

Winter 2001

# Numerical simulation of acoustic waves in a rectangular chamber

Normah Mohd. Ghazali  
*University of New Hampshire, Durham*

Follow this and additional works at: <https://scholars.unh.edu/dissertation>

---

## Recommended Citation

Mohd. Ghazali, Normah, "Numerical simulation of acoustic waves in a rectangular chamber" (2001). *Doctoral Dissertations*. 53.  
<https://scholars.unh.edu/dissertation/53>

This Dissertation is brought to you for free and open access by the Student Scholarship at University of New Hampshire Scholars' Repository. It has been accepted for inclusion in Doctoral Dissertations by an authorized administrator of University of New Hampshire Scholars' Repository. For more information, please contact [nicole.hentz@unh.edu](mailto:nicole.hentz@unh.edu).

## **NOTE TO USERS**

**This reproduction is the best copy available.**

UMI<sup>®</sup>



**NUMERICAL SIMULATION OF ACOUSTIC WAVES IN  
A RECTANGULAR CHAMBER**

BY

**Normah Mohd. Ghazali**

**B.Sc. Nuclear Engineering, University of Wisconsin-Madison(1984)  
M.Sc. Mechanical Engineering, University Malaya, Malaysia(1992)**

**Submitted to the University of New Hampshire  
in partial fulfillment of  
the requirements for the degree of**

**Doctor of Philosophy  
in  
Mechanical Engineering**

**December 2001**

UMI Number: 3030604

Copyright 2001 by  
Mohd. Ghazali, Normah

All rights reserved.

UMI<sup>®</sup>

---

UMI Microform 3030604

Copyright 2002 by Bell & Howell Information and Learning Company.

All rights reserved. This microform edition is protected against  
unauthorized copying under Title 17, United States Code.

---

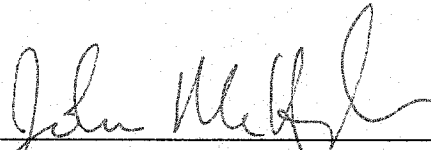
Bell & Howell Information and Learning Company  
300 North Zeeb Road  
P.O. Box 1346  
Ann Arbor, MI 48106-1346

**ALL RIGHTS RESERVED**

**©2001**

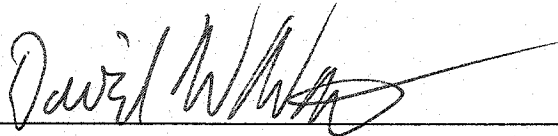
**Normah Mohd.Ghazali**

This dissertation has been examined and approved.



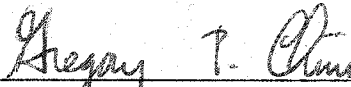
---

Director, John P. McHugh  
Associate Professor of Mechanical Engineering



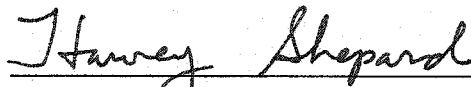
---

David W. Watt  
Associate Professor of Mechanical Engineering



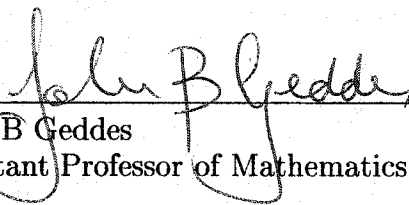
---

Gregory P. Chini  
Assistant Professor of Mechanical Engineering



---

Harvey K. Shepard  
Professor of Physics



---

John B. Geddes  
Assistant Professor of Mathematics

12/10 /2001

---

Date

# Dedication

To my husband Ismail Harun, my children  
Muhammad Hazim, Iffah, Amnah and Nuha.



## Acknowledgments

I would like to very much thank my primary advisor, Dr. John P. McHugh for guiding me through my research. His insistence on quality has helped me to persevere through the difficulties particularly during the last stages of the research. Thank you to my secondary advisor, Dr. David W. Watt for the initial introduction to my research topic, his continued support and encouragement throughout my research. A thank you too, to all the PhD committee who has been patient and tolerant of the inconveniences associated with my PhD defense.

I would like to thank Universiti Teknologi Malaysia for the financial support during my study leave here, and the UNH Graduate School for the graduate teaching assistantship.

My very special thanks to my very best friend Emilee Khalil, giving moral, spiritual and material support at all times. Special thanks to Tracy Harvey for being there through the years, always ready to help even amidst her busy schedule at the ME department. Carole McCarthy for also being my friend and sounding board. Lastly but not least, to Jason Farias for being my technical advisor and a friendly neighbor in the Kingsbury Annex Building.

Most important of all, my endless gratitude to my husband and children who has been patient and supportive through the years.

# TABLE OF CONTENTS

Dedication . . . . .	iv
Acknowledgments . . . . .	v
Abstract . . . . .	xii
<b>1 INTRODUCTION</b>	<b>1</b>
<b>2 GOVERNING EQUATIONS</b>	<b>3</b>
<b>3 COMPUTATIONAL FORMULATION</b>	<b>6</b>
3.1 Approach A . . . . .	7
3.2 Approach B . . . . .	9
3.3 Numerical techniques . . . . .	11
<b>4 VERIFICATION</b>	<b>13</b>
<b>5 RESULTS WITHOUT PLATES</b>	<b>21</b>
5.1 Beating phenomena . . . . .	24
5.2 Crosswaves . . . . .	27
5.3 Oscillatory Boundary layers . . . . .	28
5.4 Vortex motion in corners . . . . .	29
5.5 Acoustic streaming . . . . .	30
<b>6 RESULTS WITH PLATES</b>	<b>52</b>
6.1 Heat Exchanger Plates . . . . .	52

6.2 Thick plate . . . . .	52
6.3 Thin plates . . . . .	55
6.4 Multiple thin plates . . . . .	56
<b>7 Conclusions</b>	<b>95</b>
<b>Bibliography</b>	<b>96</b>
<b>Appendices</b>	<b>97</b>

## List of Tables

4.1	Parameters used in a test case. . . . .	14
4.2	Inviscid: Computed and exact wave speed . . . . .	14
4.3	Viscous: Computed and exact wave speed . . . . .	17
4.4	Viscous with conduction: Computed and exact wave speed . . . . .	19
5.1	Parameters for a test case. . . . .	21
5.2	Resulting frequencies at various Re number . . . . .	26
5.3	Resulting frequencies at various start-up period . . . . .	26

## List of Figures

4-1	Linear inviscid case: horizontal velocity . . . . .	15
4-2	Linear viscous case: horizontal velocity . . . . .	16
4-3	Linear viscous with conduction: horizontal velocity . . . . .	20
4-4	Comparison between linear viscous with and without conduction . . . . .	20
5-1	Elevations of axial velocity (u) for a sequence of times. . . . .	32
5-2	Elevations of transverse velocity (v) for a sequence of times. . . . .	33
5-3	Axial velocity at t=0.601. . . . .	34
5-4	Axial velocity at t=3.601. . . . .	35
5-5	Transverse velocity at t=0.601. . . . .	36
5-6	Transverse velocity at t=3.601. . . . .	37
5-7	Elevations of axial velocity (u) for a sequence of times. . . . .	38
5-8	Elevations of transverse velocity (v) for a sequence of times. . . . .	39
5-9	Mean temperature(diaphragm) in chamber for six cycles. . . . .	40
5-10	Mean kinetic energy in system through 10 cycles. . . . .	40
5-11	Energy flux for ten cycles. . . . .	41
5-12	Kinetic energy without non-linear terms. . . . .	41
5-13	Vorticity at t=1.801. . . . .	42
5-14	Vorticity at t=2.401. . . . .	43
5-15	Vorticity at t=3.001. . . . .	44
5-16	Resolution difficulties at high Reynolds number. . . . .	45

5-17	Vector plot of vortex flow near membrane at $t=2.701$ .	46
5-18	Vector plot of vortex flow near membrane at $t=3.001$ .	47
5-19	Vector plot of vortex flow near membrane at $t=3.301$ .	48
5-20	Vector plot of vortex flow near membrane at $t=3.601$ .	49
5-21	Vector plot of vortex flow near membrane at $t=6.001$ .	50
5-22	Acoustic streaming flow pattern.	51
5-23	Average transverse velocity at $y=0.75$ .	51
6-1	Axial velocity at $t=0.601$ .	59
6-2	Axial velocity at $t=3.601$ .	60
6-3	Transverse velocity at $t=0.601$ .	61
6-4	transverse velocity at $t=3.601$ .	62
6-5	Vorticity contour for lower half of chamber at $t=2.701$ .	63
6-6	Vorticity contour for lower half of chamber at $t=3.001$ .	64
6-7	Vorticity contour for lower half of chamber at $t=3.301$ .	65
6-8	Vector plot near front of plate at $t=2.701$ .	66
6-9	Vector plot near front of plate at $t=3.001$ .	67
6-10	Vector plot near front of plate at $t=3.301$ .	68
6-11	Vector plot near front of plate at $t=3.601$ .	69
6-12	Vector plot near front of plate at $t=6.001$ .	70
6-13	Vector plot behind plate at $t=2.701$ .	71
6-14	Vector plot behind plate at $t=3.001$ .	72
6-15	Surface heat flux.	73

6-16 Axial velocity at $t=0.601$ . . . . .	74
6-17 Axial velocity at $t=3.601$ . . . . .	75
6-18 Transverse velocity at $t=0.601$ . . . . .	76
6-19 Transverse velocity at $t=3.601$ . . . . .	77
6-20 Mean temperature in chamber. . . . .	78
6-21 Kinetic energy in chamber. . . . .	79
6-22 Heat flux at $x=0.15$ . . . . .	79
6-23 Vorticity contour for lower half of chamber at $t=2.701$ . . . . .	80
6-24 Vorticity contour for lower half of chamber at $t=3.001$ . . . . .	81
6-25 Vorticity contour for lower half of chamber at $t=3.301$ . . . . .	82
6-26 Vector plot near front of plate at $t=2.701$ . . . . .	83
6-27 Vector plot near front of plate at $t=3.001$ . . . . .	84
6-28 Vector plot near front of plate at $t=3.301$ . . . . .	85
6-29 Vector plot near front of plate at $t=3.601$ . . . . .	86
6-30 Vector plot near front of plate at $t=6.001$ . . . . .	87
6-31 Vector plot behind plate at $t=2.701$ . . . . .	88
6-32 Vector plot behind plate at $t=3.001$ . . . . .	89
6-33 Vorticity contour in chamber with 5 plates. . . . .	90
6-34 Temperature difference between plate ends, plate length=0.2. . . . .	91
6-35 Temperature difference between plate ends versus plate position. . . . .	91
6-36 Temperature difference vs number of plates. . . . .	92
6-37 Temperature pattern between plates with 2-plate (top) and 9-plate (bottom). . . . .	93
6-38 Flow pattern between plates with 2-plate (top) and 9-plate (bottom). . . . .	94

**ABSTRACT**

**NUMERICAL SIMULATION OF ACOUSTIC WAVES IN A  
RECTANGULAR CHAMBER**

by

Normah Mohd. Ghazali  
University of New Hampshire, December, 2001

Numerical simulation of acoustic waves in a closed two-dimensional rectangular chamber is considered. The waves are generated by a membrane or piston boundary condition on one wall. The simulations are performed through many acoustic cycles. A stack of heat exchanger plates are sometimes included. The study is motivated by thermoacoustic refrigeration, a phenomena which uses sound waves in a chamber to achieve a cooling effect.

The present study treats the flow numerically. The governing equations are the viscous compressible Navier-Stokes system, assuming a perfect gas. The numerical method employs a finite difference spatial discretization and semi-implicit time-marching procedure. Verification is accomplished by propagating linear acoustic waves.

The desired result of forcing is a standing wave. However, the results show a significantly more complex flow than the expected standing wave, including beating, crosswaves, and streaming. Vortex flow also appears near the wavemaker and in the area surrounding the plate.



# Chapter 1

## INTRODUCTION

Numerical simulation of acoustic waves in a closed two-dimensional rectangular chamber is considered. The waves are generated by a membrane or piston boundary condition on one wall. The simulations are performed through several acoustic cycles. Heat exchanging plates of various length and position are sometimes included. The simulations are motivated by thermoacoustic refrigeration, a phenomena which uses sound waves in a chamber to achieve a cooling effect.

Recent interest has been directed towards the study of thermoacoustic refrigeration due to the overall simplicity of thermoacoustic devices. The thermoacoustic effect may have been used over a century ago by European glass blowers. Known as the Sondhauss effect, it was discussed qualitatively in 1877 by William Strutt [1]. An early modern thermoacoustic refrigerator was a testbed cryocooler built by Hoffer in 1986 [2]. It was a gas-filled resonator containing a stack of plates and driven by a loudspeaker. Active study into thermoacoustic applications appears to have started with the Montreal Protocol [3], an international agreement to reduce and later stop the worldwide production of harmful refrigerants, chlorofluorocarbons (CFCs). The absence of any refrigerants, moving parts, and lubricants makes thermoacoustic refrigeration an appealing replacement for current refrigeration systems [4]. Unfortunately, previous thermoacoustic systems have low coefficient of performance. Although they are generally simple, reliable, and inexpensive, further research is needed before they can be an acceptable replacement to current systems.

The numerical results given herein treat the entire resonator, and allow the acoustic wave to evolve in time, adjusting to the no-slip boundary conditions, the presence of heat exchanging plates, and other features. Previous numerical work on thermoacoustics has mainly concentrated on the plate region where the cooling effects are observed [6]-[8]. Worlikar and Knio [6] used central finite difference methodology on rectangular grids. The Navier-Stokes system is solved implicitly to first order. Their numerical study, however, covers only the region enclosing two plates and without any oscillating flow anywhere in their computational domain. They also neglect thermal diffusion. Cao et. al [7] also modeled the two plate region using finite differences, discretized the governing equations on staggered grids. Their numerical method was only first order accurate in time, and the physical model included both the diffusive and dissipative effects. However, the boundary conditions have assumed a priori the presence of standing and/or travelling waves on the left and right side of the horizontal plates.

The governing equations for the present study are the viscous compressible Navier-Stokes system, assuming a perfect gas. The numerical method employs a finite difference spatial discretization and semi-implicit time marching procedure. All algebraic equations are treated using the Gauss-Seidel iteration method. Linear terms are evaluated with the Crank-Nicholson method, and non-linear terms with the fourth-order Adams-Bashforth method.

The results show that the oscillating flow causes a variety of patterns, including beating, cross waves, streaming, and other flows.

## Chapter 2

### GOVERNING EQUATIONS

The governing equations are the equations of continuity, momentum and energy, assuming a compressible Newtonian fluid with constant thermophysical properties. These equations in Cartesian coordinates for two-dimensions are [5]

$$\frac{D\rho}{Dt} + \rho(\nabla \cdot \mathbf{u}) = 0, \quad (1)$$

$$\rho \left( \frac{\partial \mathbf{u}}{\partial t} + (\mathbf{u} \cdot \nabla) \mathbf{u} \right) = -\nabla p + \mu \nabla^2 \mathbf{u} + \frac{\mu}{3} \nabla(\nabla \cdot \mathbf{u}), \quad (2)$$

$$\rho c_p \frac{DT}{Dt} = \nabla \cdot (K \nabla T) + \frac{Dp}{Dt} + \mu \Phi, \quad (3)$$

where  $\Phi$  is the viscous dissipation given by

$$\Phi = 2 \left[ \left( \frac{\partial u}{\partial x} \right)^2 + \left( \frac{\partial v}{\partial y} \right)^2 \right] + \left( \frac{\partial u}{\partial y} + \frac{\partial v}{\partial x} \right)^2 - \frac{2}{3} \left( \frac{\partial u}{\partial x} + \frac{\partial v}{\partial y} \right)^2, \quad (4)$$

$\rho$  is the density,  $\mu$  is dynamic viscosity,  $K$  is the thermal conductivity, and  $c_p$  is the isobaric specific heat. The velocity components are  $(u, v)$ . The bulk viscosity is assumed to be zero, and body forces have been excluded.

Ideal gas behavior is assumed, where

$$p = \rho RT. \quad (5)$$

Density is now eliminated from (1) using (5), and the resulting equations are put in dimensionless form using

$$t^* = t\omega, \quad x^* = \frac{x}{H}, \quad y^* = \frac{y}{H},$$

$$u^* = \frac{u}{\omega H}, \quad v^* = \frac{v}{\omega H}, \quad \rho^* = \frac{\rho}{\rho_m},$$

$$T^* = \frac{T}{T_m}, \quad p^* = \frac{p}{\rho_m R T_m},$$

where  $H$  is the width of the resonator,  $\omega$  is the forcing frequency, and  $\rho_m, T_m$  are the mean density and temperature of domain. Note that the subscript generally refers to a mean or average quantity. The dimensionless equations, after dropping the circumflex, are

$$\frac{D}{Dt} \left( \frac{p}{T} \right) = \left( -\frac{p}{T} \right) \left( \frac{\partial u}{\partial x} + \frac{\partial v}{\partial y} \right), \quad (6)$$

$$\rho \frac{Du}{Dt} = -\frac{1}{M^2 \gamma} \frac{\partial p}{\partial x} + \frac{1}{Re} \nabla^2 u + \frac{1}{3Re} \frac{\partial}{\partial x} \left( \frac{\partial u}{\partial x} + \frac{\partial v}{\partial y} \right), \quad (7)$$

$$\rho \frac{Dv}{Dt} = -\frac{1}{M^2 \gamma} \frac{\partial p}{\partial y} + \frac{1}{Re} \nabla^2 v + \frac{1}{3Re} \frac{\partial}{\partial y} \left( \frac{\partial u}{\partial x} + \frac{\partial v}{\partial y} \right), \quad (8)$$

$$\rho \frac{DT}{Dt} = \frac{1}{Pe} \nabla^2 T + \left( \frac{\gamma - 1}{\gamma} \right) \frac{Dp}{Dt} + \frac{M^2}{Re} (\gamma - 1) \Phi'. \quad (9)$$

The Reynolds number, Mach number, and Peclet number are defined as

$$Re = \frac{H^2 \omega}{\nu}, \quad (10)$$

$$M = \frac{\omega H}{\sqrt{\gamma R T_m}}, \quad (11)$$

$$Pe = \frac{H^2 \omega}{\alpha}, \quad (12)$$

respectively.

The boundary conditions are no-slip, no-penetration, and zero heat flux,

$$v(0, y, t) = 0, \quad (13)$$

$$u\left(\frac{L}{H}, y, t\right) = v\left(\frac{L}{H}, y, t\right) = 0, \quad (14)$$

$$u(x, 0, t) = v(x, 0, t) = 0, \quad (15)$$

$$u(x, 1, t) = v(x, 1, t) = 0, \quad (16)$$

where  $L/H$  is the aspect ratio, and  $L$  is the length of the resonator. Furthermore,  $u(0, y, t)$  will be chosen to drive the acoustic waves, as discussed later.

## Chapter 3

### COMPUTATIONAL FORMULATION

The dimensional pressure, temperature, and density are separated into a mean and fluctuating part,

$$p = p_m + p', \quad (17)$$

$$T = T_m + T', \quad (18)$$

$$\rho = \rho_m + \rho', \quad (19)$$

where  $p'$ ,  $T'$ , and  $\rho'$  are the fluctuating parts. Equations (17-19) are made non-dimensional as before, inserted into (6-9), and the circumflex is dropped. After expanding the derivatives on the left-hand side, (6) becomes

$$(1 + T) \frac{Dp}{Dt} = (1 + p) \frac{DT}{Dt} - (1 + p)(1 + T) \nabla \cdot \mathbf{u}. \quad (20)$$

Note that the dimensionless mean pressure, temperature, and density are unity. Equations (7-9) become

$$\frac{\partial u}{\partial t} = -\frac{1}{M^2 \gamma} \frac{\partial p}{\partial x} + \frac{1}{Re} \nabla^2 u + \frac{1}{3Re} \frac{\partial}{\partial x} \left( \frac{\partial u}{\partial x} + \frac{\partial v}{\partial y} \right) - Q_x, \quad (21)$$

$$\frac{\partial v}{\partial t} = -\frac{1}{M^2 \gamma} \frac{\partial p}{\partial y} + \frac{1}{Re} \nabla^2 v + \frac{1}{3Re} \frac{\partial}{\partial y} \left( \frac{\partial u}{\partial x} + \frac{\partial v}{\partial y} \right) - Q_y, \quad (22)$$

$$\frac{\partial T}{\partial t} = \frac{1}{Pe} \nabla^2 T + \left( \frac{\gamma - 1}{\gamma} \right) \frac{\partial p}{\partial t} - Q_T, \quad (23)$$

where the nonlinear terms are combined in the subscripted Q:

$$Q_x = \rho \frac{Du}{Dt} + u \frac{\partial u}{\partial x} + v \frac{\partial u}{\partial y}, \quad (24)$$

$$Q_y = \rho \frac{Dv}{Dt} + u \frac{\partial v}{\partial x} + v \frac{\partial v}{\partial y}, \quad (25)$$

$$Q_T = \rho \frac{DT}{Dt} + u \frac{\partial T}{\partial x} + v \frac{\partial T}{\partial y} - \left( \frac{\gamma - 1}{\gamma} \right) \left( u \frac{\partial p}{\partial x} + v \frac{\partial p}{\partial y} \right). \quad (26)$$

Note that viscous dissipation has been dropped, which is generally important only for very low Re flow. Furthermore, the terms in (24-26) containing  $\rho$  are now neglected. This approximation has the convenient consequence of eliminating  $\rho$  from the system, and can be justified with a Boussinesq type scale argument.

Two approaches, A and B, are considered. The difference between the methods concerns the treatment of several terms in (20).

### 3.1 Approach A

The linear and nonlinear terms in (20) are separated, as before, resulting in

$$\frac{\partial p}{\partial t} = \frac{\partial T}{\partial t} - (\nabla \cdot \mathbf{u}) - Q_p, \quad (27)$$

where  $Q_p$  is given by

$$Q_p = T \left( \frac{\partial p}{\partial t} + u \frac{\partial p}{\partial x} + v \frac{\partial p}{\partial y} \right) - p \left( \frac{\partial T}{\partial t} + u \frac{\partial T}{\partial x} + v \frac{\partial T}{\partial y} \right)$$

$$+ \left( u \frac{\partial p}{\partial x} + v \frac{\partial p}{\partial y} \right) + (p + T + pT) \nabla \cdot \mathbf{u}, \quad (28)$$

Eliminate  $p$  in (21-23) using (27) to obtain

$$\begin{aligned} \frac{\partial^2 u}{\partial t^2} &= \frac{1}{M^2 \gamma} \left( \frac{\partial^2 u}{\partial x^2} + \frac{\partial^2 v}{\partial x \partial y} - \frac{\partial^2 T}{\partial x \partial t} \right) \\ &+ \frac{1}{Re} \frac{\partial}{\partial t} (\nabla^2 u) + \frac{1}{3Re} \frac{\partial}{\partial t} \left( \frac{\partial^2 u}{\partial x^2} + \frac{\partial^2 v}{\partial x \partial y} \right) \\ &+ \frac{1}{M^2 \gamma} \frac{\partial}{\partial x} (Q_p) - \frac{\partial}{\partial t} (Q_x), \end{aligned} \quad (29)$$

$$\begin{aligned} \frac{\partial^2 v}{\partial t^2} &= \frac{1}{M^2 \gamma} \left( \frac{\partial^2 u}{\partial x \partial y} + \frac{\partial^2 v}{\partial y^2} - \frac{\partial^2 T}{\partial y \partial t} \right) \\ &+ \frac{1}{Re} \frac{\partial}{\partial t} (\nabla^2 v) + \frac{1}{3Re} \frac{\partial}{\partial t} \left( \frac{\partial^2 u}{\partial x \partial y} + \frac{\partial^2 v}{\partial y^2} \right) \\ &+ \frac{1}{M^2 \gamma} \frac{\partial}{\partial y} (Q_p) - \frac{\partial}{\partial t} (Q_y), \end{aligned} \quad (30)$$

$$\frac{\partial T}{\partial t} = \frac{\gamma}{Pe} \nabla^2 T + (1 - \gamma) (\nabla \cdot \mathbf{u}) + (1 - \gamma) Q_p - \gamma Q_T, \quad (31)$$

The above equations are solved simultaneously for  $u$ ,  $v$  and  $T$ , and pressure is obtained from

$$\frac{\partial p}{\partial t} = \frac{\gamma}{\gamma - 1} \left( \frac{\partial T}{\partial t} - \frac{1}{Pe} \nabla^2 T + Q_T \right) \quad (32)$$

A further assumption, often made by previous researchers, but not included here, is large Peclet number. If  $Pe$  number is assumed to be large, then the diffusion term in (31) is dropped. Equation (31) is then used to eliminate temperature in (29) and (30) to obtain

$$\frac{\partial^2 u}{\partial t^2} = \frac{1}{M^2} \left( \frac{\partial^2 u}{\partial x^2} + \frac{\partial^2 v}{\partial x \partial y} \right)$$



$$\begin{aligned}
& + \frac{1}{Re} \frac{\partial}{\partial t} (\nabla^2 u) + \frac{1}{3Re} \frac{\partial}{\partial t} \left( \frac{\partial^2 u}{\partial x^2} + \frac{\partial^2 v}{\partial x \partial y} \right) \\
& + \frac{1}{M^2} \frac{\partial}{\partial x} (Q_p + Q_T) - \frac{\partial}{\partial t} (Q_x), \tag{33}
\end{aligned}$$

$$\begin{aligned}
\frac{\partial^2 v}{\partial t^2} &= \frac{1}{M^2} \left( \frac{\partial^2 u}{\partial x \partial y} + \frac{\partial^2 v}{\partial y^2} \right) \\
& + \frac{1}{Re} \frac{\partial}{\partial t} (\nabla^2 v) + \frac{1}{3Re} \frac{\partial}{\partial t} \left( \frac{\partial^2 u}{\partial x \partial y} + \frac{\partial^2 v}{\partial y^2} \right) \\
& + \frac{1}{M^2} \frac{\partial}{\partial y} (Q_p + Q_T) - \frac{\partial}{\partial t} (Q_y). \tag{34}
\end{aligned}$$

The temperature and pressure would then be determined using

$$\frac{\partial T}{\partial t} = (1 - \gamma) (\nabla \cdot \mathbf{u}) + (1 - \gamma) Q_p - \gamma Q_T, \tag{35}$$

$$\frac{\partial p}{\partial t} = \frac{\gamma - 1}{\gamma} \left( \frac{\partial T}{\partial t} + Q_T \right). \tag{36}$$

Equations (33-36) are only given for comparison with previous work. The diffusion term in (31) was not neglected for the results given below.

### 3.2 Approach B

The second approach is to transfer a linear term,  $\frac{\partial T}{\partial t}$ , to the sum of nonlinear terms to obtain

$$\frac{\partial p}{\partial t} = -(\nabla \cdot \mathbf{u}) - Q_p, \tag{37}$$

where  $Q_p$  is now defined as

$$Q_p = u \frac{\partial p}{\partial x} + v \frac{\partial p}{\partial y} - \left( \frac{1+p}{1+T} \right) \frac{DT}{Dt} + p \nabla \cdot \mathbf{u}. \quad (38)$$

Using (38) to eliminate pressure in (21-23) gives

$$\begin{aligned} \frac{\partial^2 u}{\partial t^2} &= \frac{1}{M^2 \gamma} \left( \frac{\partial^2 u}{\partial x^2} + \frac{\partial^2 v}{\partial x \partial y} \right) \\ &+ \frac{1}{Re} \frac{\partial}{\partial t} (\nabla^2 u) + \frac{1}{3Re} \frac{\partial}{\partial t} \left( \frac{\partial^2 u}{\partial x^2} + \frac{\partial^2 v}{\partial x \partial y} \right) \\ &- \frac{\partial}{\partial t} (Q_x) + \frac{1}{M^2 \gamma} \frac{\partial}{\partial x} (Q_p), \end{aligned} \quad (39)$$

$$\begin{aligned} \frac{\partial^2 v}{\partial t^2} &= \frac{1}{M^2 \gamma} \left( \frac{\partial^2 u}{\partial x \partial y} + \frac{\partial^2 v}{\partial y^2} \right) \\ &+ \frac{1}{Re} \frac{\partial}{\partial t} (\nabla^2 v) + \frac{1}{3Re} \frac{\partial}{\partial t} \left( \frac{\partial^2 u}{\partial x \partial y} + \frac{\partial^2 v}{\partial y^2} \right) \\ &- \frac{\partial}{\partial t} (Q_y) + \frac{1}{M^2 \gamma} \frac{\partial}{\partial y} (Q_p), \end{aligned} \quad (40)$$

$$\frac{\partial T}{\partial t} = \frac{1}{Pe} \nabla^2 T + \left( \frac{1-\gamma}{\gamma} \right) (\nabla \cdot \mathbf{u}) - Q_T + \left( \frac{1-\gamma}{\gamma} \right) Q_p. \quad (41)$$

The advantage of this approach is that (39) and (40) are now independent of temperature.

Pressure is obtained from equation (23):

$$\frac{\partial p}{\partial t} = \frac{\gamma}{\gamma-1} \left( \frac{\partial T}{\partial t} - \frac{1}{Pe} \nabla^2 T + Q_T \right). \quad (42)$$

### 3.3 Numerical techniques

Spatial derivatives are approximated with finite differences, accurate to second order. Interior grid points use central differences, for example,

$$\frac{\partial u}{\partial x} \approx \frac{u_{i+1,j} - u_{i-1,j}}{2\Delta x}, \quad (43)$$

$$\frac{\partial^2 u}{\partial x^2} \approx \frac{u_{i+1,j} - 2u_{i,j} + u_{i-1,j}}{\Delta x^2}. \quad (44)$$

One-sided derivatives are used on the boundaries, for example,

$$\frac{\partial u}{\partial x} \approx \frac{-3u_{i,j} + 4u_{i+1,j} - u_{i+2,j}}{2\Delta x}, \quad (45)$$

$$\frac{\partial^2 u}{\partial x^2} \approx \frac{2u_{i,j} - 5u_{i+1,j} + 4u_{i+2,j} - u_{i+3,j}}{\Delta x^2}. \quad (46)$$

The temporal integration is achieved with a semi-implicit method, where linear terms are treated implicitly, and non linear terms explicitly. The linear terms in the equations containing first order temporal derivatives, such as (29) and (30), are treated with the Crank-Nicholson method in the usual manner. Note that the Crank-Nicholson method is second order accurate. The nonlinear terms in (29) and (30) are treated with the Adams-Bashforth method.

The linear terms in the equations with second order temporal derivatives must be carefully treated to avoid severe artificial damping of acoustic waves. Consider for example

$$\frac{\partial^2 u}{\partial t^2} = f(u).$$

The equation is approximated with

$$\frac{u^{n+1} - 2u^n + u^{n-1}}{\Delta t^2} \simeq \frac{f^{n+1} + f^{n-1}}{2}, \quad (47)$$

which can be shown to be second-order accurate in time. The non-linear terms in (29) and (30) are approximated with

$$\frac{\partial Q_x}{\partial t} \simeq \frac{Q_x^n - Q_x^{n-1}}{\Delta t}, \quad (48)$$

which is first-order accurate in time. The complete set of discrete equations is given in Appendix A.

Waves are forced by imposing the normal component of velocity along one side. The  $x = 0$  boundary used for this purpose, and the imposed velocity has the form

$$u(0, y) = U_o h(y) \sin t,$$

where  $U_o$  is the forcing amplitude of the velocity and  $h(y)$  is a shape function. Two shape functions have been employed;  $h = 1$ , which corresponds to a piston wavemaker, and  $h = \sin y$ , which corresponds to a membrane. A piston boundary condition has the left wall forcing amplitude constant in  $y$ , and the membrane boundary condition has a sinusoidal increase in the amplitude with a maximum and a minimum occurring at the chamber centerline.

## Chapter 4

### VERIFICATION

Verification of computational formulation, numerical methods, and software is accomplished by propagating linear acoustic waves computationally and comparing the results to the exact solution. Both inviscid and viscous cases are considered using approach A.

An exact solution is found by discarding the viscous, conduction, and nonlinear terms, and assuming the wave motion is one dimensional, reducing (33) to

$$\frac{\partial^2 u}{\partial t^2} = \frac{1}{M^2} \left( \frac{\partial^2 u}{\partial x^2} \right). \quad (49)$$

The solution is

$$u = U_0 e^{i(kx - \omega t)}, \quad (50)$$

where  $U_0$ ,  $k$ , and  $\omega$  are constants, and

$$\omega^2 = \frac{k^2}{M^2}. \quad (51)$$

The boundary at  $x = 0$  is the wavemaker, oscillating at a dimensionless frequency of unity.

A forced wave will therefore have  $\omega = 1$ , and  $k^2 = M^2$ .

The numerical solution to the linear inviscid equations is obtained using the methods in the previous section. The viscous terms are removed and the no-slip condition is discarded.

Otherwise the simulations are unchanged. The parameter values for a test case are given

in table 4.1.

M	0.905
Pr	0.67
L/H	4.00
$\Delta t$	0.01
$U_o$	0.1

Table 4.1 Parameters used in a test case.

Waves are allowed to propagate in the simulations until the domain is nearly filled, but without reaching the opposite boundary to avoid reflections. Figure 4-1 shows the velocity profile for a resolution of 400 x 100 (axial x transverse) at  $t = 5.656$ . Note in figure 4-1 that the wave is not attenuated, as expected when diffusion is excluded, and the wave amplitude matches the forcing amplitude of the wavemaker. Table 4.2 shows that the numerical results produce wave parameters which converge to the exact solution as resolution increases. The wavespeed matches the exact solution to approximately 3% at a resolution of 400, while the wavenumber matches to within 0.11%.

spatial resolution	wave speed	wave number, k
100 x 30	1.0755	0.9232
200 x 30	1.0682	0.9022
400 x 30	1.0719	0.9060
exact	1.105	0.905

Table 4.2 Inviscid: Computed and exact wave speed

Viscosity is now included. An exact solution is available again, assuming  $u = u(x, t)$ .

Neglecting nonlinear terms and heat diffusion, equation (33) is

$$\frac{\partial^2 u}{\partial t^2} = \frac{1}{M^2} \frac{\partial^2 u}{\partial x^2} + \frac{4}{3Re} \frac{\partial}{\partial t} \left( \frac{\partial^2 u}{\partial x^2} \right), \quad (52)$$

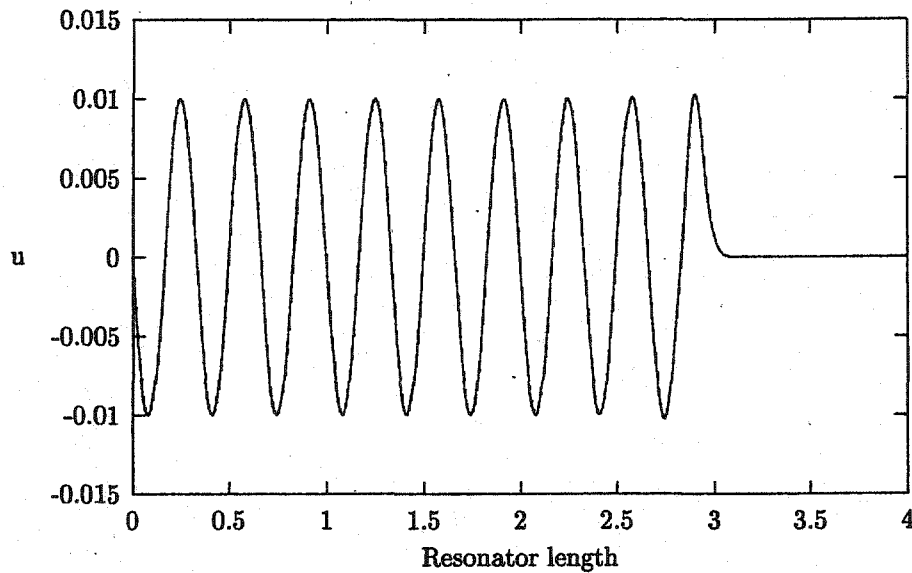


Figure 4-1 Linear inviscid case: horizontal velocity

which has the solution

$$u(x, t) = U_0 e^{-i\omega t} e^{ikx} \quad (53)$$

The solution for an evanescent wave is obtained by choosing  $\omega$  to be real and solving for  $k$ , resulting in

$$k = \frac{\omega \sqrt{\frac{1}{M^2} - \frac{4i\omega}{3Re}}}{\frac{1}{M^2} - \frac{4i\omega}{3Re}} \quad (54)$$

Note that  $k$  is complex. The corresponding wave speed is

$$c = \sqrt{\frac{1}{M^2} - \frac{4i\omega}{3Re}} \quad (55)$$

The value of the wave number for  $Re = 40$ , and  $M = 0.905$  is

$$k = 0.905 + 0.012i$$

The value of the wavespeed is

$$c = 1.105 - 0.015i$$

Note that the real part of the wavespeed and the wave number are not significantly different from the inviscid case, since the second term on the right of (55) is small compared to the first term.

The above exact solution is compared to the numerical results again by forcing waves that propagate parallel to the x-axis, and examining the results before the leading wave has reached the opposite wall. The simulation is performed in two spatial dimensions, imposing the no-slip condition on all boundaries. Figure 4-2 shows the resulting velocity along the centerline of the chamber at a time of 5.656. Note that a similar velocity profile near the top or bottom boundary ( $y=0$  or  $1$ ) would be greatly altered due to the boundary layer flow. This boundary layer, and other phenomena, are discussed in the next section.

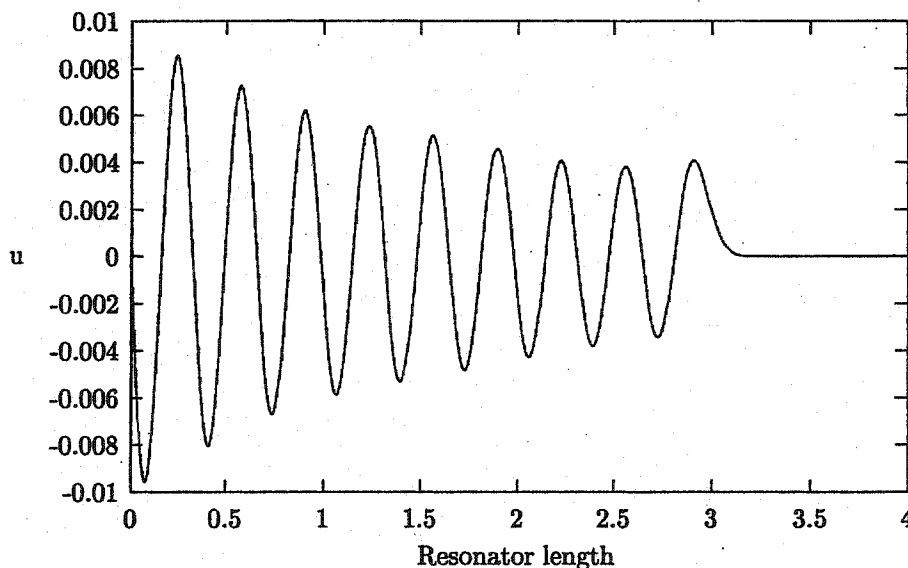


Figure 4-2 Linear viscous case: horizontal velocity

The velocity profile in figure 4-2 clearly shows the spatial decay of an evanescent wave.



However, the exponential envelope is not fully developed, as can be seen in the leading few waves of the profile. The simulation should continue to allow the profile to develop, however, the leading wave quickly reaches the opposite boundary, and reflections pollute the solution.

Table 4.3 compares wave parameters between the exact and numerical solutions for a variety of resolutions. The decay factor is obtained using the logarithmic decrement. Note that the leading wave is avoided when determining the decay factor. Increasing the resolution for the y direction results in the wave speed that matches the exact solution to within 2.7%, while the wave number matches to within 1%. Note that higher resolution in y had no effect on the inviscid results, since there was no variation in y for the inviscid case.

spatial resolution	wave speed	wave number, k	decay factor
100 x 30	1.0755	0.9425	0.5542
200 x 30	1.0829	0.9003	0.5646
400 x 30	1.0829	0.8936	0.5848
800 x 30	1.0755	0.8969	0.5902
400 x 100	1.0755	0.9139	0.3490
exact	1.105	0.905	0.346

Table 4.3 Viscous: Computed and exact wave speed

Clearly, the accurate match of wave speed, wave number, and decay factor between exact and numerical solutions demonstrates the validity of the computational formulation, the numerical techniques, and the computer codes.

Now include conduction in the linear viscous model. The linear equations, assuming wave propagation in only one space dimension, are

$$\frac{\partial^2 u}{\partial t^2} = \frac{1}{M^2 \gamma} \left( \frac{\partial^2 u}{\partial x^2} - \frac{\partial^2 T}{\partial x \partial t} \right) + \frac{4}{3Re} \frac{\partial}{\partial t} \left( \frac{\partial^2 u}{\partial x^2} \right), \quad (56)$$

$$\frac{\partial T}{\partial t} = \frac{\gamma}{Pe} \frac{\partial^2 T}{\partial x^2} + (1 - \gamma) \frac{\partial u}{\partial x}, \quad (57)$$

$$\frac{\partial p}{\partial t} = \frac{\gamma}{\gamma - 1} \left( \frac{\partial T}{\partial t} - \frac{1}{Pe} \frac{\partial^2 T}{\partial x^2} \right). \quad (58)$$

The analytic solution is

$$u(x, t) = U_o e^{-i\omega t} e^{ikx}, \quad (59)$$

$$T(x, t) = T_o e^{-i\omega t} e^{ikx}, \quad (60)$$

$$p(x, t) = p_o e^{-i\omega t} e^{ikx}. \quad (61)$$

Substituting (59-61) into (56-58), one gets

$$\begin{pmatrix} \omega^2 - \frac{k^2}{M^2 \gamma} + \frac{4i\omega k^2}{3Re} & \frac{-k\omega}{M^2 \gamma} & 0 \\ (1 - \gamma) ik & \left( i\omega - \frac{\gamma k^2}{Pe} \right) & 0 \\ 0 & \left( \frac{k^2}{Pe} - \frac{i\gamma\omega}{(\gamma-1)} \right) & i\omega \end{pmatrix} \begin{pmatrix} U_o \\ T_o \\ p_o \end{pmatrix} = 0. \quad (62)$$

Since the coefficients  $U_o$ ,  $T_o$ , and  $p_o$  cannot be zero for a non-trivial solution, the determinant of the matrix A must be zero. Let  $\omega = 1$  to match the forcing frequency, then k is found to be

$$k = \frac{-A + \sqrt{A^2 - 4B}}{2}, \quad (63)$$

where

$$A = -\frac{Pe}{\gamma} \frac{\frac{4i}{3Re} - \frac{1}{M^2} + \frac{i\gamma}{Pe}}{\frac{4}{3Re} + \frac{i}{M^2 \gamma}},$$

$$B = -\frac{Pe}{\gamma} \frac{\omega^3}{\frac{4\omega}{3Re} + \frac{i}{M^2\gamma}}$$

Choosing the parameters in table 5.1, the wave number is computed to be

$$k = 0.818 + 0.022i.$$

The corresponding wavespeed is

$$c = 1.221 - 0.033i$$

The simulations are performed as before, using the piston wavemaker and allowing waves to propagate nearly to the end wall. Figure 4-3 shows the computed axial velocity along the centerline of the chamber at this time. Table 4.4 shows the results at different resolutions. Note that conduction (+) has decreased the wave speed in comparison to the solution of the linear viscous case without conduction (-), as can be seen in figure 4-4.

spatial resolution	wave speed	wave number, k	decay factor
100 x 30	0.9724	1.0556	0.2600
200 x 30	0.9577	1.0349	0.2875
400 x 30	0.9724	1.0006	0.3541
800 x 30	0.9724	1.0029	0.3502
400 x 100	0.9724	1.0006	0.3541
exact	1.221	0.8190	0.3509

Table 4.4 Viscous with conduction: Computed and exact wave speed

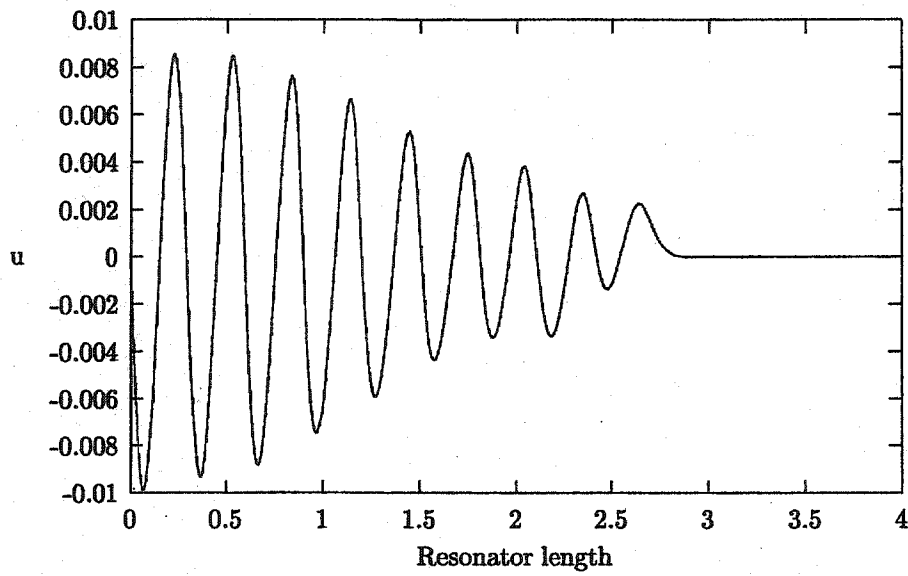


Figure 4-3 Linear viscous with conduction: horizontal velocity

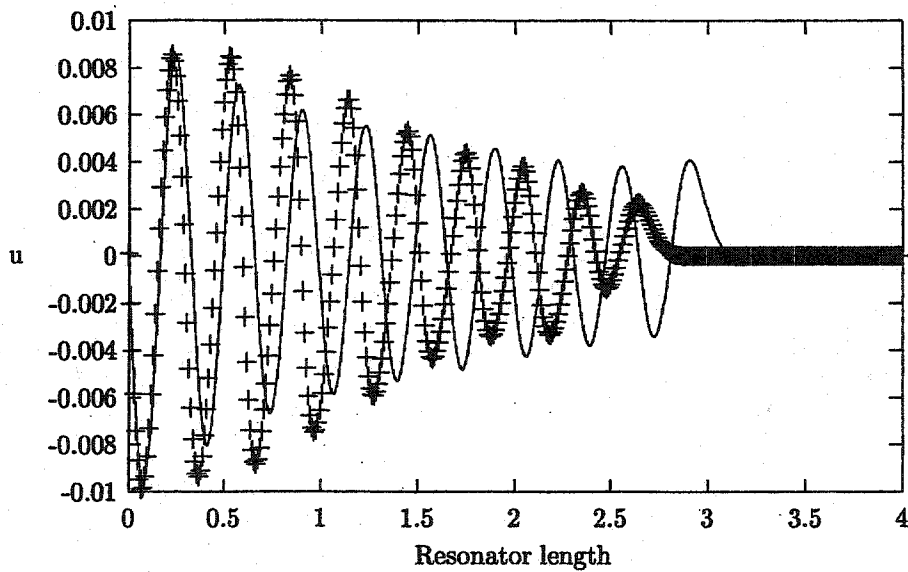


Figure 4-4 Comparison between linear viscous with and without conduction

## Chapter 5

### RESULTS WITHOUT PLATES

Consider the numerical solution to the full non-linear Navier-Stokes system with conduction. The heat exchanger plates normally installed in a practical thermoacoustic device are not included here. A set of parameters (shown in table 5.1) is chosen based on a typical operating condition for a thermoacoustic resonator.

$P_m$	101 kPa
$T_m$	293K
M	0.7854
Pr	0.67
Re	800000
Pe	600000
L/H	4.00
$\Delta t$	0.001
$\Delta x$	0.01
$U_o$	0.001

Table 5.1 Parameters for a test case.

The Mach number is chosen so that the forcing will produce waves with a half wavelength ( $n=0.5$ ) that matches the domain length, Using linear inviscid theory, (51) gives

$$M = k = \frac{2\pi}{\lambda}, \quad (64)$$

where  $\lambda$  is the dimensionless wavelength. The wavelength is chosen to be twice the length of the chamber:

$$\lambda = 2L, \quad (65)$$

$$M = \frac{\pi}{L}. \quad (66)$$

A membrane wavemaker is employed, which models a loudspeaker, as used in most thermoacoustic refrigerators. The wavemaker is on the left wall of the rectangular chamber. The forcing is maintained for the duration of the simulation. Results for a typical case using a membrane wavemaker are shown in figures 5-1 and 5-2 with a resolution of 100x30. Figure 5-1 shows a sequence of surface plots of axial velocity,  $u$ , while figure 5-2 shows the transverse velocity,  $v$ . Note that the period of the wavemaker in the rescaled system is  $2\pi$ . Hence the results in figures 5-1 and 5-2 correspond to an interval of ten periods of forcing.

Higher resolution simulations (400x100) are shown in figures 5-3 through 5-6 for the same case. Higher resolution required a smaller time step, and made a ten cycle simulation difficult to achieve. Note that figures 5-3 through 5-6 correspond to an interval of only one cycle of forcing.

Surface plots of  $u$  and  $v$  with a piston wavemaker (instead of the membrane) are shown in figures 5-7 and 5-8. Note that the axial velocity imposed by the piston wavemaker (constant in  $y$ ) in figures 5-7 and 5-8 is equal to the maximum axial velocity imposed by the membrane wavemaker, which occurs in the wavemaker center. This results in the acoustic wave driven by a piston having a higher amplitude than the wave driven by a membrane, as can be seen by comparing 5-1 and 5-7.

Several diagnostic quantities are evaluated at each time step during the simulations. The quantities are the average temperature in the domain,

$$\bar{T} = \frac{1}{V} \int \int T dV, \quad (67)$$

the energy flux across a line of constant  $x$ ,

$$\overline{uT} = \frac{1}{H} \int (uT) dy, \quad (68)$$

the average kinetic energy of the system ,

$$\overline{KE} = \frac{1}{2V} \int \int (u^2 + v^2) dV, \quad (69)$$

and

$$\bar{v} = \frac{1}{L} \int v^2 dx, \quad (70)$$

which is a useful measure of streaming, the expression  $V$  being the volume of the domain.

Figures 5-9, 5-10, and 5-11 show the diagnostic quantities corresponding to the results in figures 5-1 and 5-2. Note that the mean temperature shown in figure 5-9 is oscillatory. A careful observation of figure 5-9 reveals that the temperature does not return to zero after a few cycles, and the maximum temperature has slightly increased. This is attributed to viscous dissipation.

The desired result of the forcing is a standing acoustic wave. However, the velocity field is significantly more complex than the expected standing wave, as is evident in figures 5-1 and 5-2. The added features can be categorized as follows:

- Beating phenomena
- Crosswaves
- Streaming

- Oscillatory boundary layers and Stokes' solution
- Vortex motion in the corners near the wavemaker

### 5.1 Beating phenomena

The 'beating' phenomena occurs when the amplitude of an oscillation also oscillates. The beating effect in the present simulations can be seen by studying the mean kinetic energy,  $\overline{KE}$ , shown in figure 5-10 for the present example. (Note that since kinetic energy is always positive, a cycle corresponds to two peaks of kinetic energy). The amplitude is clearly seen to have an oscillation at a frequency much lower than the forcing frequency. Subsequent cases, performed for more cycles, demonstrate that the beating effect continues, repeating the pattern shown in figure 5-10 very closely, indicating an oscillation phenomena rather than a transient effect. The energy flux in figure 5-11 also shows the beating phenomena.

The simplest explanation of beating is that of an oscillation with two incommensurate frequencies which are close in value. Using sinusoidal functions, the beating behavior can be modeled simply with the product of two cosine functions:

$$\cos \omega_f t \cos \omega_n t, \quad (71)$$

where  $\omega_f$  and  $\omega_n$  are the high and low frequencies measured in the results. Equation (71) can be arranged into the sum of two independent oscillations at two other frequencies with the following identity:

$$A \cos \omega_1 t + A \cos \omega_2 t = 2A \cos \left[ \frac{\omega_1 + \omega_2}{2} t \right] \cos \left[ \frac{\omega_1 - \omega_2}{2} t \right], \quad (72)$$



where  $\omega_1$  and  $\omega_2$  are the frequencies of the individual oscillations. The frequency pairs are then related by

$$\omega_n = \frac{\omega_1 - \omega_2}{2}, \quad (73)$$

$$\omega_f = \frac{\omega_1 + \omega_2}{2}. \quad (74)$$

Two frequencies can be extracted from figure 5-10; a high frequency,  $\omega_f$ , and a low frequency,  $\omega_n$ . The frequency relations, (73) and (74), may then be used to determine  $\omega_1$  and  $\omega_2$ .

Simulations are performed to determine the values of  $\omega_f$  and  $\omega_n$  for a variety of parameter values. The simulations are performed using the parameters in table 5.1 for an interval of Reynolds numbers. The value of  $\omega_f$  and  $\omega_n$  is determined directly from the average kinetic energy for each case, and the trigometric relation is used to determine  $\omega_1$  and  $\omega_2$  from these values.

Table 5.2 shows the results. Note that  $\omega_f$  is consistently near 0.95, which is approximately the forcing frequency of unity. The value of  $\omega_n$ , which will be called the envelope frequency, is seen to vary only slightly with Reynolds number, until the Reynolds number reaches a very low value, and the beating is no longer present. This trend with Reynolds number appears to be the result of excessive damping on the envelope oscillation and occurs with both types of wavemaker, the membrane and the piston.

One explanation for the beating is that the envelope oscillation is the result of the transient behavior at the beginning of the simulation. The initial wave propagates across the chamber, reflects off of the end of the chamber, and then the incident wave and the reflected wave interact to form the standing wave. This transition from a motionless fluid to a standing wave must result in the low frequency behavior. Perhaps the forcing could

Re number	$w_n$	$w_f$
40	nil	0.9520
100	0.2327	0.9520
1000	0.1348	0.9520
800000	0.1051	0.9520
10000000	0.1051	0.9520

Table 5.2 Resulting frequencies at various Re number

be initiated such that there is no beating, both in the simulations studied here, and in a practical device. The link between the forcing and the beating is studied here by ramping up the forcing amplitude, a scheme which has been used at length in many types of numerical simulations. The amplitude is assumed to increase linearly, until a chosen time, beyond which it remains constant. The simulation continues for a total of ten cycles of the forcing, and then  $\omega_f$  and  $\omega_n$  are determined from the average kinetic energy, equation (69). The resulting values of  $\omega_f$  and  $\omega_n$  are shown in table 5.3.

Period of linear increase(cycle)	$w_n$	$w_f$
1	0.0952	0.9520
2	0.0868	0.9520
3	0.0799	0.9520
4	0.0739	0.9520
5	0.0689	0.9520
6	0.0645	0.9666
7	0.0605	0.9666
8	0.0571	0.9666
9	0.0512	0.9666
10	0.0512	0.9666

Table 5.3 Resulting frequencies at various start-up period

Note in table 5.3 that  $\omega_f$  is only slightly affected by the ramping effect. However,  $\omega_n$  is greatly affected. The value of  $\omega_n$  is reduced by an order of magnitude between the

case without any ramping and the case with ramping over one forcing period. The value continues to decrease as length of the ramping time increases. The results demonstrate that the beating phenomena is at least strongly influenced by the initialization procedures, and that perhaps there is a manner of starting the simulations to avoid the beating.

Other changes in the simulations had little or no effect on the beating phenomena. For example, varying the aspect ratio of the rectangular chamber or the forcing amplitude did not significantly affect the pattern of beating. Attempts at changing the wavenumber to a lower or higher value than the half wavelength, 0.4 and 0.6, did not significantly affect the beating.

The above simulation was fully nonlinear, but the beating phenomena is also present in a linear simulation. Figure 5-12 shows the average kinetic energy for a case matching the results in figure 5-10, except that the nonlinear terms are removed. Note that the beating effect is still present, but the amplitude of the envelope oscillation is dramatically reduced. The difference between linear and nonlinear results indicates that a complicated nonlinear interaction between the incident wave and the reflected wave plays a major role in the beating behavior.

## 5.2 Crosswaves

Crosswaves are unintended secondary waves which develop on the incident acoustic wave that have spatial oscillation 'across' the chamber. Crosswaves in acoustics and other non-linear systems have been studied previously, and are reviewed by Garrett [9].

Crosswaves can be clearly seen in the present results in contours of transverse velocity. The sequence of contours in figure 5-2 shows the advance of the crosswaves along the

chamber. Note that the dominant crosswave mode does not fill the entire chamber until nearly the sixth cycle of the standing acoustic wave. Note also that the wavemaker for figure 5-2 is a membrane.

The same sequence of surface plots of  $v$  for the piston wavemaker, shown in figure 5-8, does not show strong crosswaves. This implies that the crosswaves in figure 5-2 are wave modes which are directly forced by the membrane wavemaker.

Previous theoretical results on crosswaves imply that crosswaves will develop as a nonlinear instability, even when the wavemaker does not force them directly, such as the piston wavemaker case. The piston wavemaker does show very small amplitude crosswaves, and perhaps these waves will grow in time as a result of nonlinear interaction with the incident wave. The simulations with a piston wavemaker do not show this event. However, sufficiently long simulations could not be achieved with current computer resources.

### 5.3 Oscillatory Boundary layers

The axial oscillation of the fluid results in a boundary layer phenomena at the top and bottom boundary. These boundary layers can best be seen in contours of vorticity, as shown in figures 5-13, 5-14, and 5-15. The temporal oscillation results in spatial oscillations in the transverse direction. These oscillations are waves, and are analagous to the viscous waves in Stokes' second solution, which is the parallel flow of a viscous incompressible fluid with an oscillating bottom [10]. The wavelength of the spatial oscillations correlates approximately with Stokes' second solution.

At times the numerical methods have difficulty resolving the boundary layers, which are remarkably thin. The difficulty appears at the boundary where the axial velocity is

maximum. An example is shown in figure 5-16. Note in figure 5-16 that the point nearest the boundary shows an unrealistic value, although the remainder of the points show 'good' results. Doubling the resolution (also shown in figure 5-16) improves the results, but does not cure the problem. In general, this problem only appears sporadically, when the amplitude is large and the Reynolds number is high, and does not appear to affect the validity of the numerical solution.

#### 5.4 Vortex motion in corners

The results show that a vortex motion is present in the corners of the chamber adjacent to the wavemaker. This motion is only evident with the membrane wavemaker, and does not appear in the two corners at the opposite end of the chamber.

Consider the bottom corner, adjacent to the wavemaker. An example of the flow in this corner is shown with a sequence of vector plots in figures 5-17 through 5-20. These figures correspond to the lower left corner of the domain ( $0 < x < 0.05, 0 < y < 0.2$ ), and show the development and movement of a clockwise vortex. Note that the velocity vectors in the rest of the chamber at this time show positive axial flow, and are essentially uniform.

The clockwise vortex appears at the time when the wavemaker is imposing an axial velocity near zero, changing from positive to negative values. This would correspond to the membrane being in its rightmost position. Note in figures 5-17 through 5-20 that the vortex moves away from both the wavemaker and the adjacent wall.

Figure 5-21, which is also a vector plot of the lower left corner of the domain, shows a counterclockwise vortex. Figure 5-21 was recorded after approximately one full period of forcing. The counterclockwise vortex also appears when the wavemaker is forcing an

axial velocity near zero, the difference being that the velocity is changing from negative to positive. This would correspond to the membrane being in its leftmost position. Both the clockwise and counterclockwise vortex appear once (at different times) for every period of forcing.

The motion is symmetric about the axial centerline of the chamber. Hence the top corner adjacent to the wavemaker has the same vortex motion, except the sense of rotation is reversed.

The motion in the corners becomes increasingly complicated with each additional period of motion during a single simulation, often causing the simulation to fail due to a lack of resolution in the corners. Simulations with a resolution as high as 1200x400 failed to resolve completely this motion for long times. Long simulations can apparently only be achieved by reducing the Reynolds numbers to add sufficient damping to eliminate such complicated motion. In an experiment, the corners are likely to be a source of turbulence.

## 5.5 Acoustic streaming

Acoustic streaming is a secondary flow forced by the acoustic waves. The streaming is a steady flow along the centerline of the resonator, away from the wavemaker, and return flow along the side boundaries. A schematic diagram of the flow is shown in figure 5-22. The phenomena appears to have been first reported by Lord Rayleigh [11], and is discussed briefly in Rayleigh's volumes, *The Theory of Sound* [11]. Streaming can occur in incompressible systems also, as reviewed by Riley [12].

Streaming in the rectangular container being studied here is evaluated with

$$\bar{v} = \frac{1}{L} \int_0^1 v^2 dx, \quad (75)$$

which is determined at three evenly spaced transverse positions: the center of the domain, one quarter of the height from the top, and one quarter of the height from the bottom. Note that if the streaming is zero, then there is no significant vertical velocity at these elevations, and  $\bar{v}$  is zero. Actually,  $\bar{v}$  measures the strength of all combined secondary flows, including crosswaves. But the crosswaves are oscillatory, as will be seen in the profile. The nonoscillatory part is attributed to streaming.

A time history of  $\bar{v}$  for the upper position for an example simulation is shown in figure 5-23, again using the parameters in table 5.1. Note that  $\bar{v}$  for the centerline position remains approximately zero for the duration of the simulation, and the upper and lower positions remain equal in value. This indicates symmetric secondary flows about the axial centerline. Several features are evident in figure 5-23. The mean value of  $\bar{v}$  is increasing with time. The value of  $\bar{v}$  is oscillating, and the oscillation includes several frequencies. Finally, the magnitude of  $\bar{v}$  remains quite small.

The oscillation part of  $\bar{v}$  is certainly due to the standing acoustic wave, along with the crosswaves. The increasing trend in  $\bar{v}$  is indication of a streaming flow growing steadily in strength. Apparently, many acoustic cycles are needed to attain steady streaming, for the value of  $\bar{v}$  did not cease to increase with more cycles.

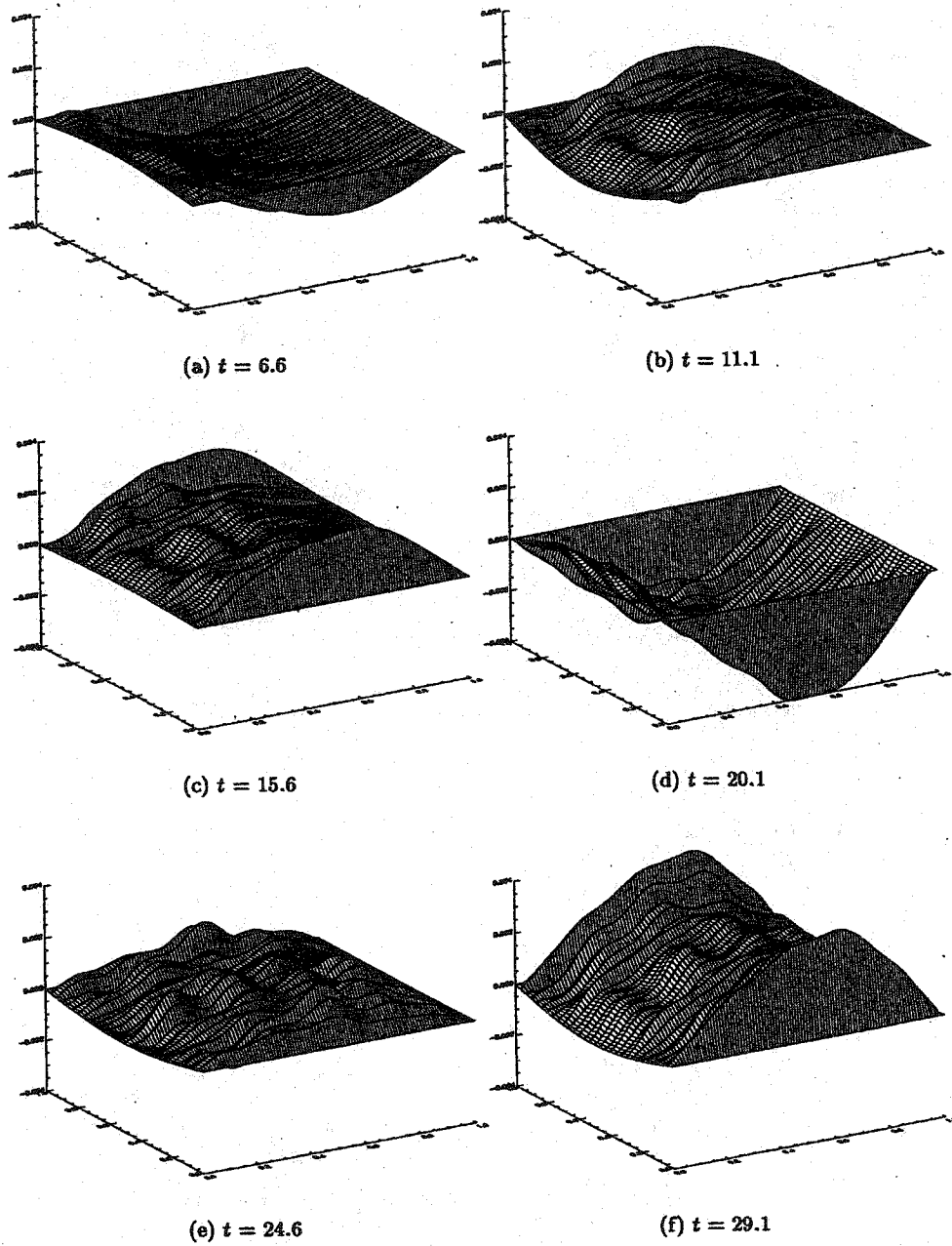


Figure 5-1 Elevations of axial velocity ( $u$ ) for a sequence of times.



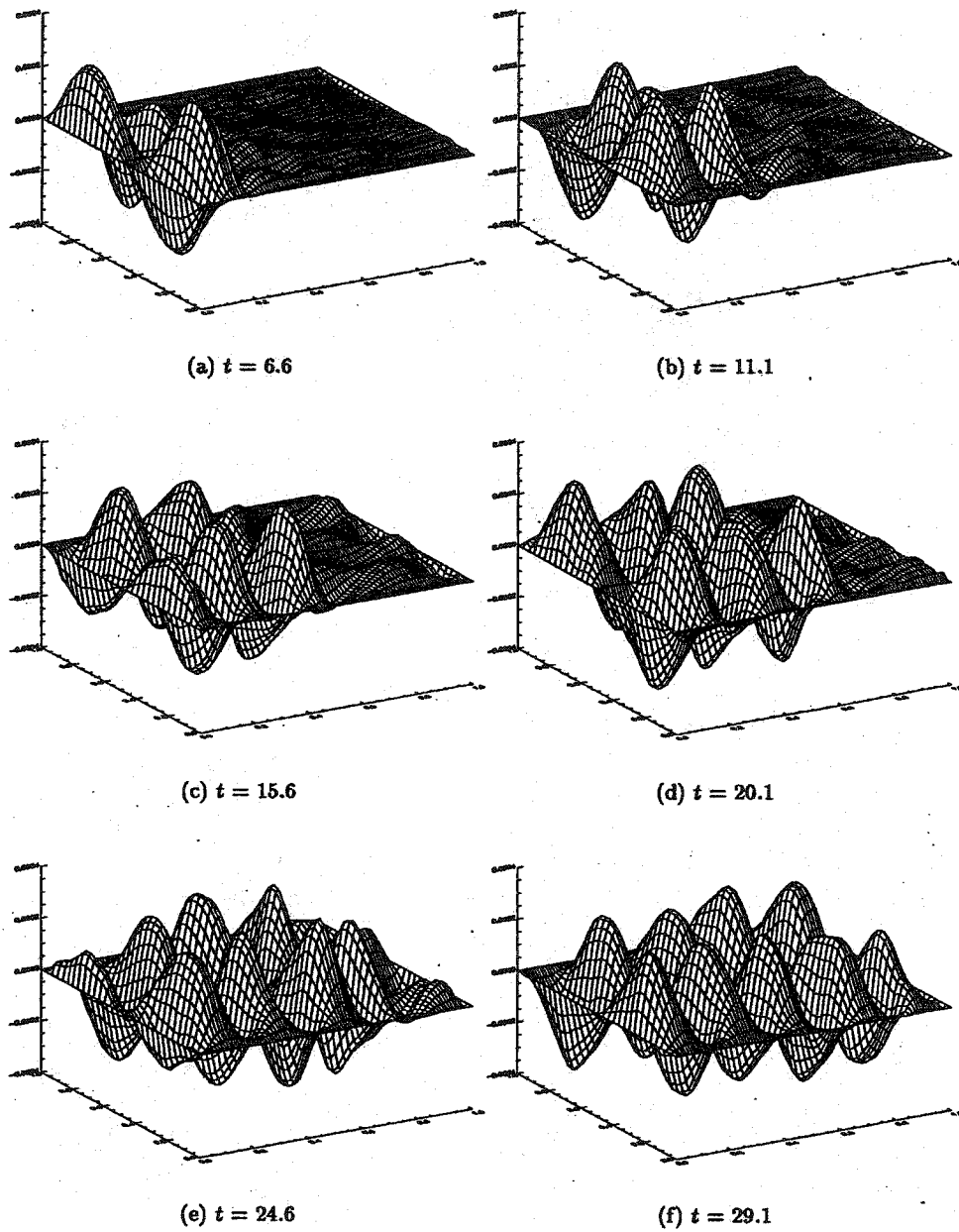


Figure 5-2 Elevations of transverse velocity ( $v$ ) for a sequence of times.

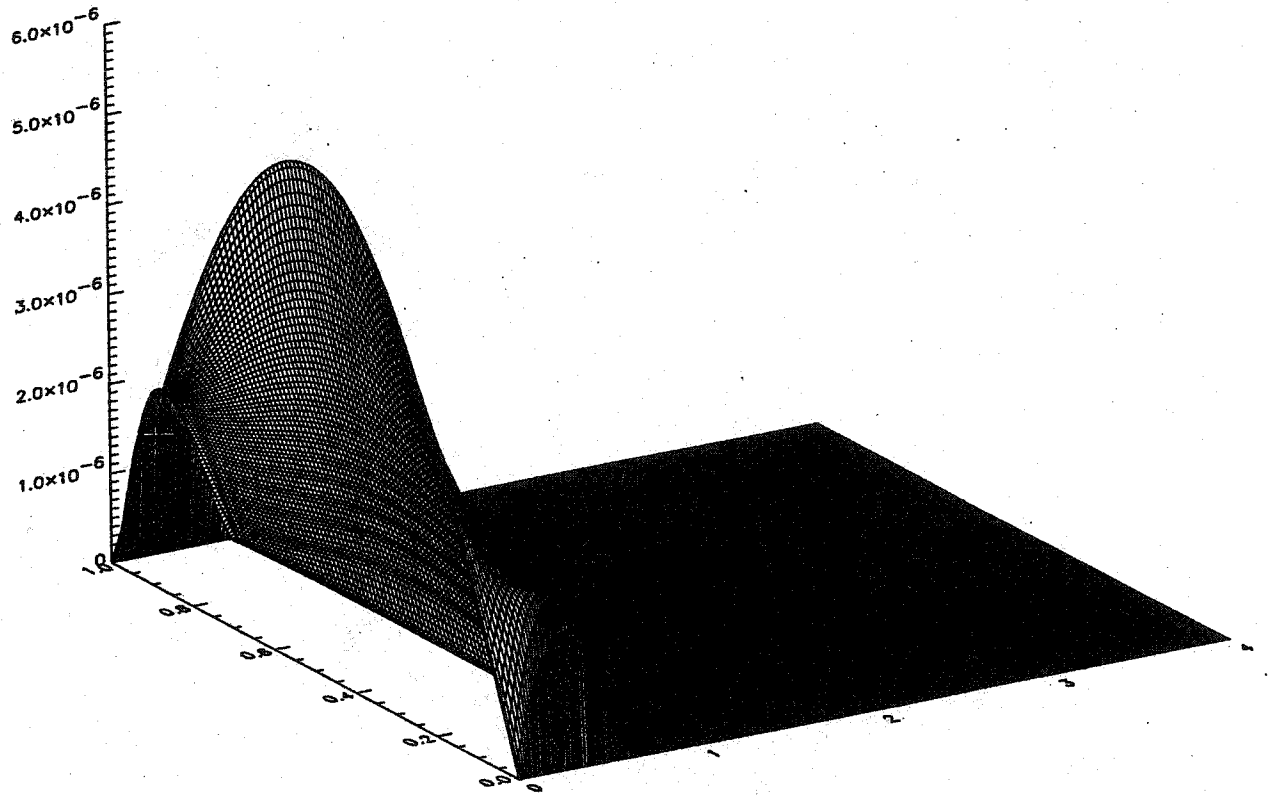


Figure 5-3 Axial velocity at  $t=0.601$ .

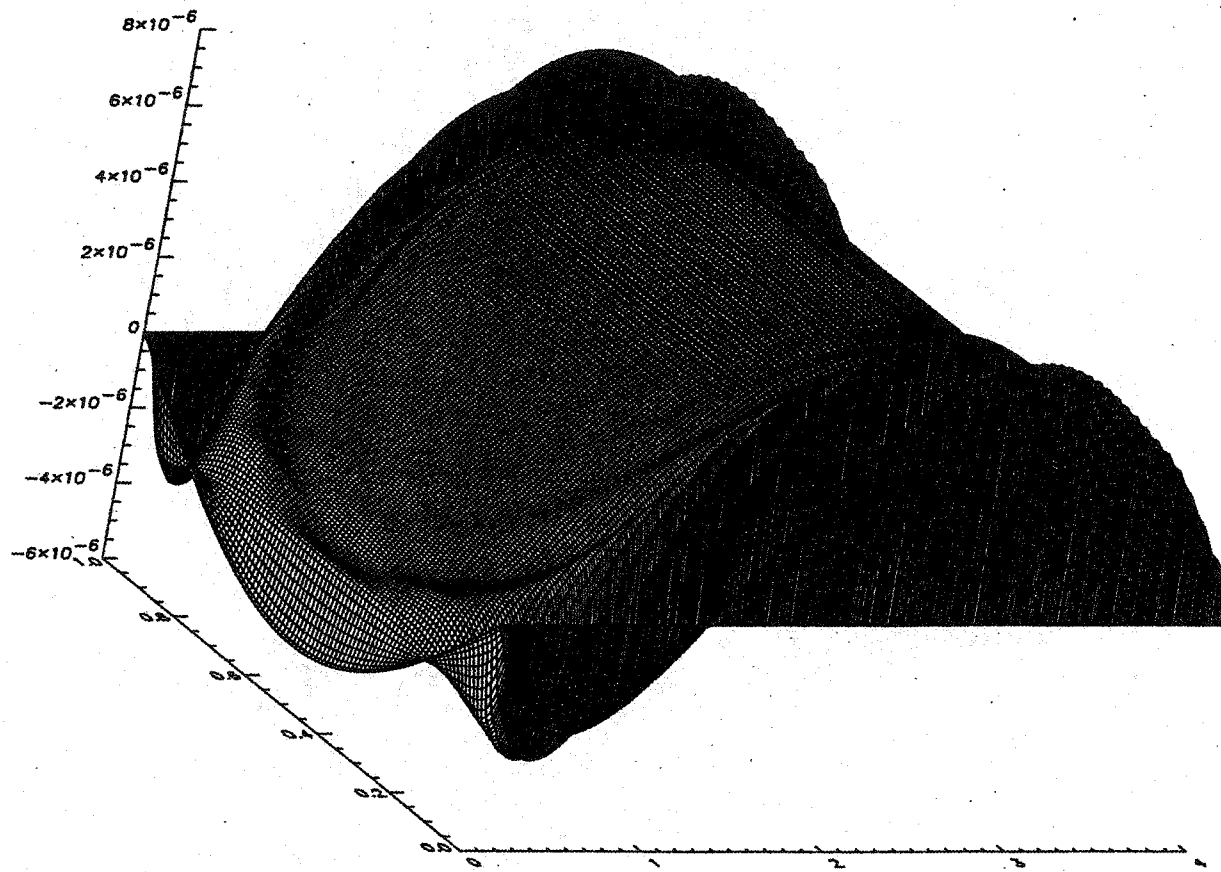


Figure 5-4 Axial velocity at  $t=3.601$ .

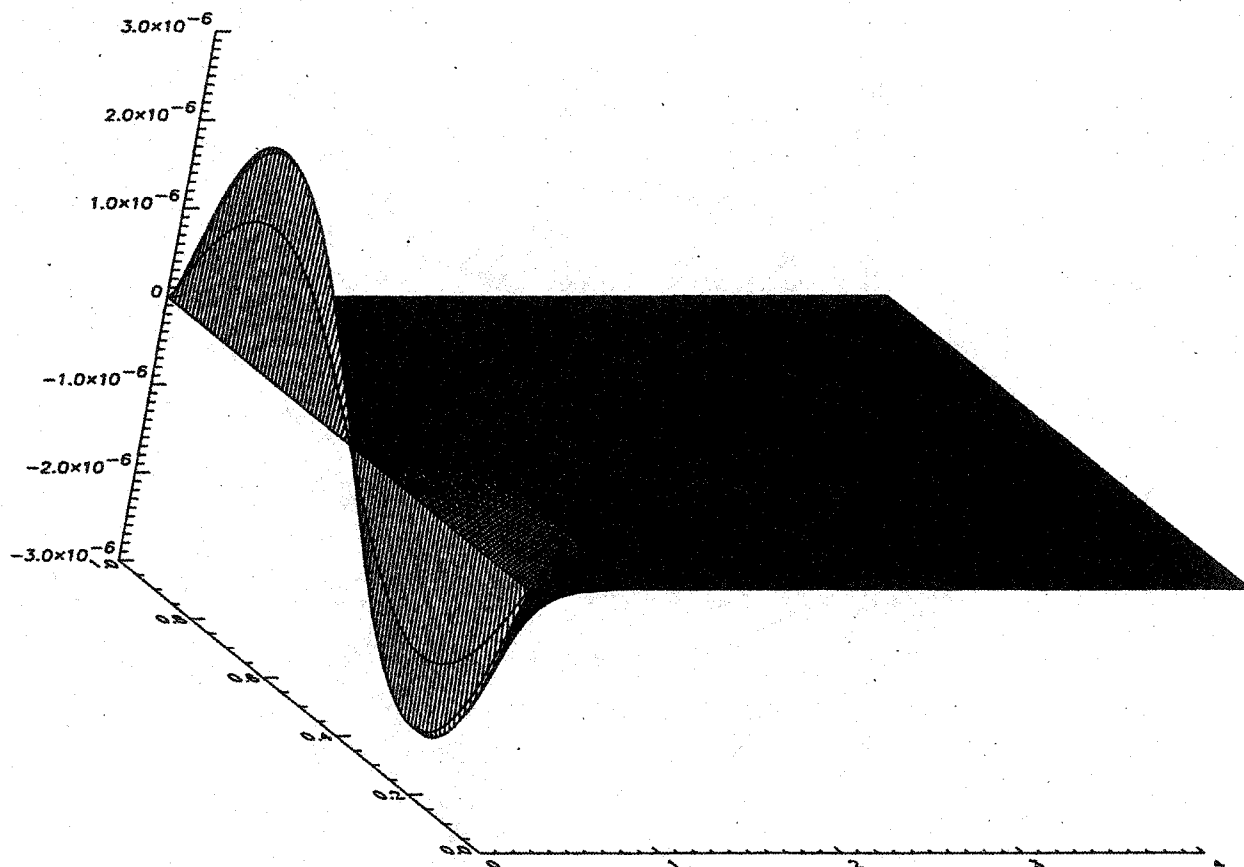


Figure 5-5 Transverse velocity at  $t=0.601$ .

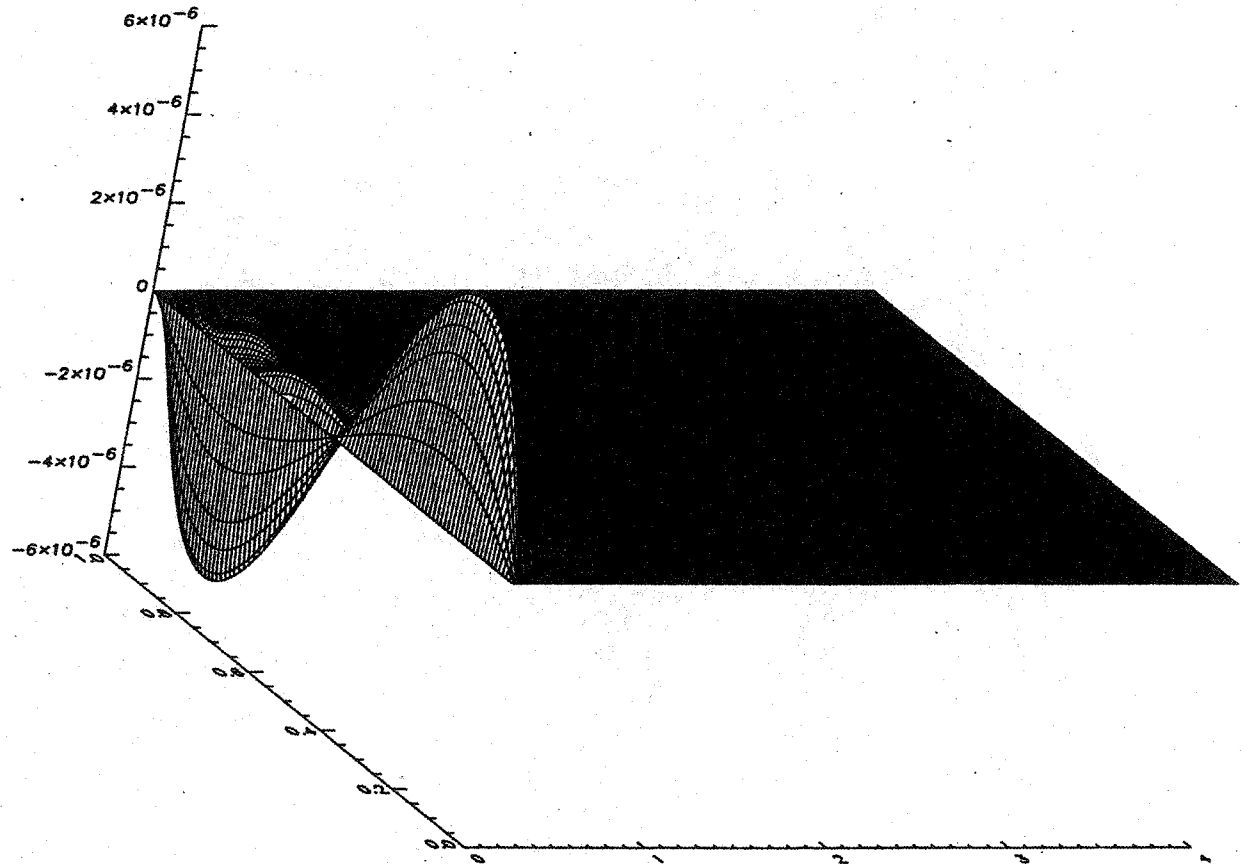


Figure 5-6 Transverse velocity at  $t=3.601$ .

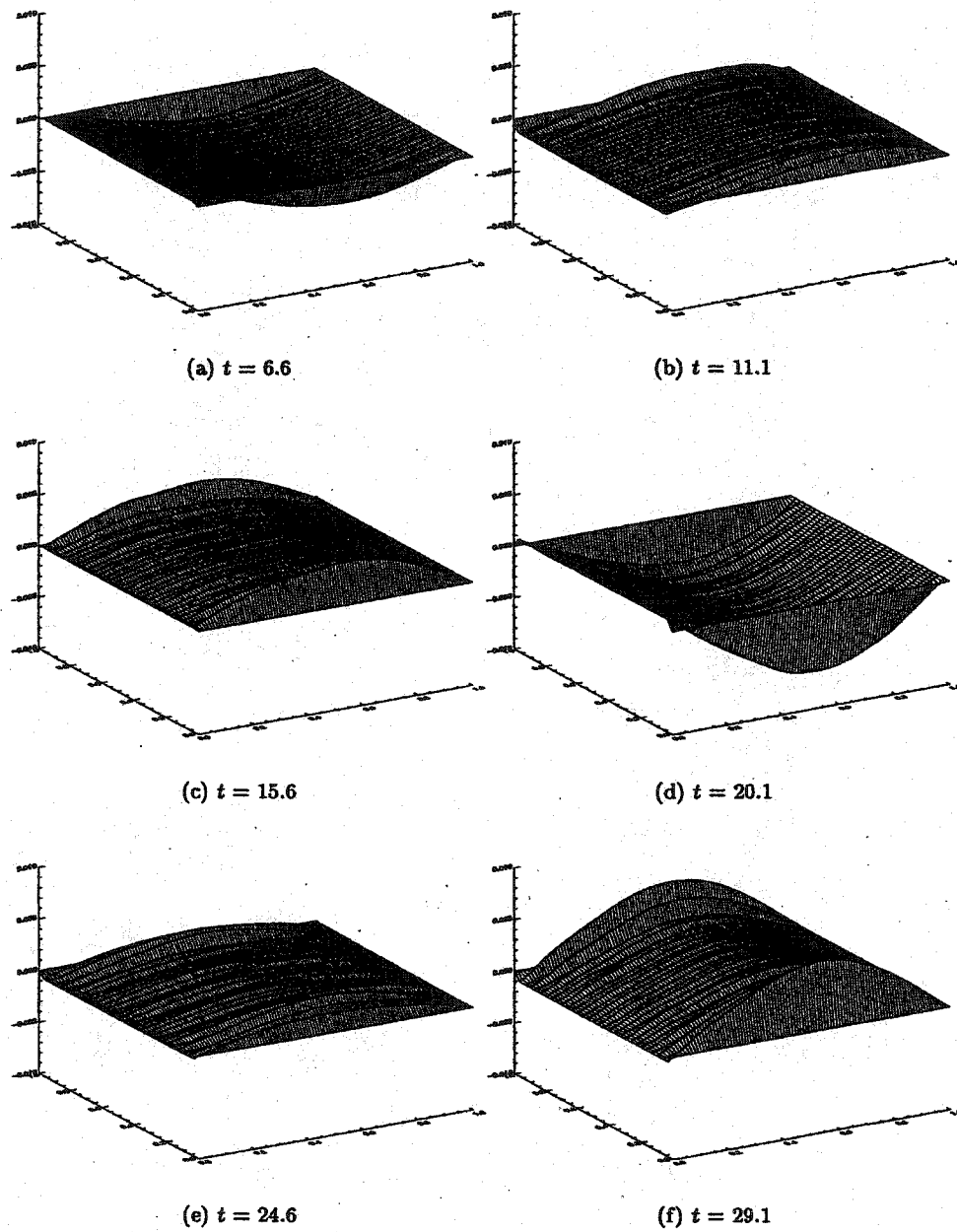


Figure 5-7 Elevations of axial velocity ( $u$ ) for a sequence of times.

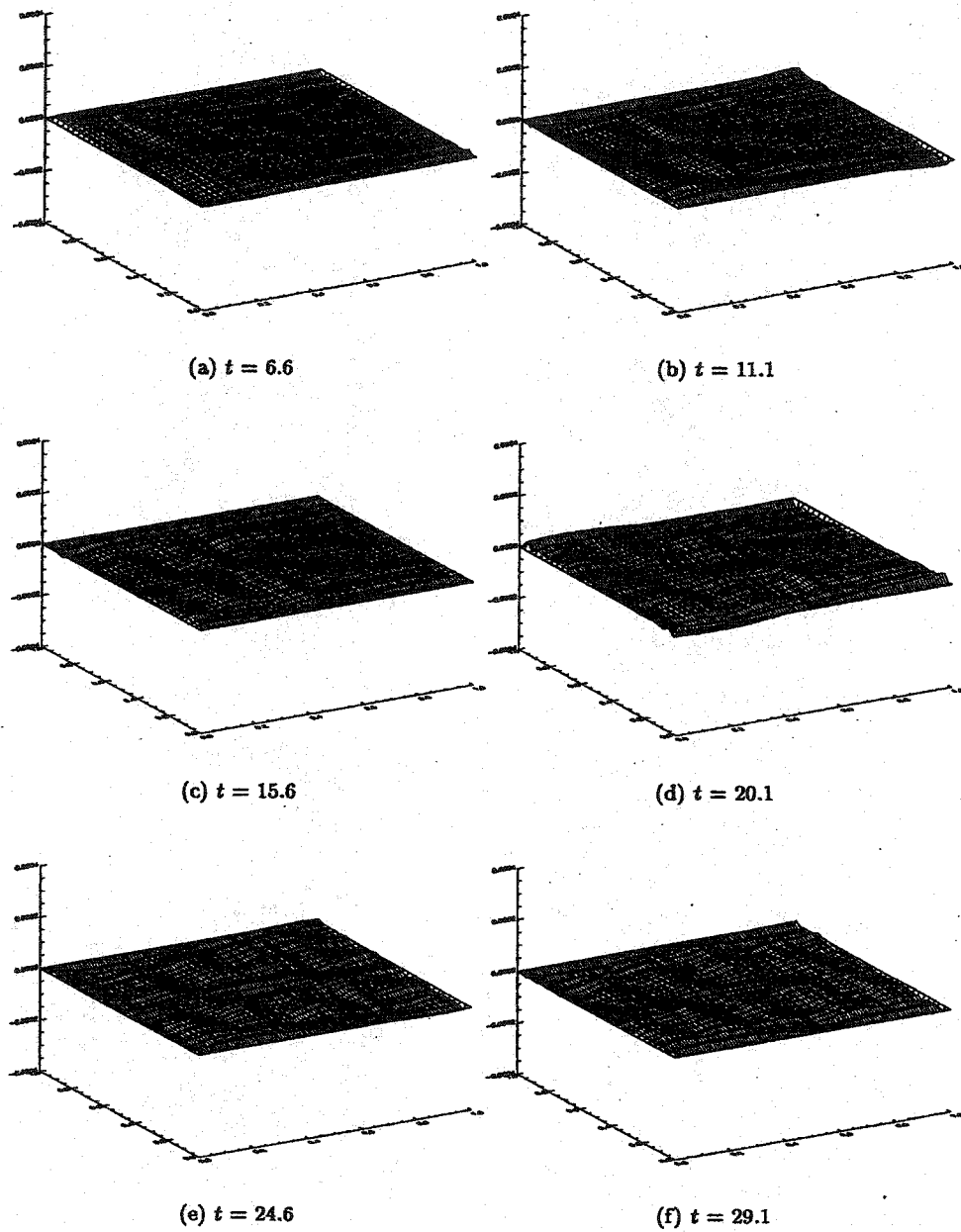


Figure 5-8 Elevations of transverse velocity ( $v$ ) for a sequence of times.

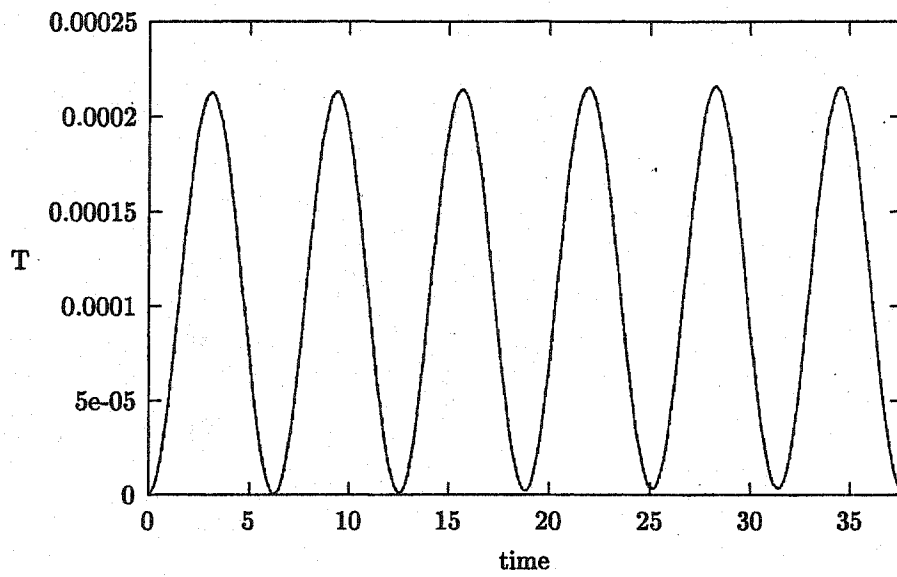


Figure 5-9 Mean temperature(diaphragm) in chamber for six cycles.

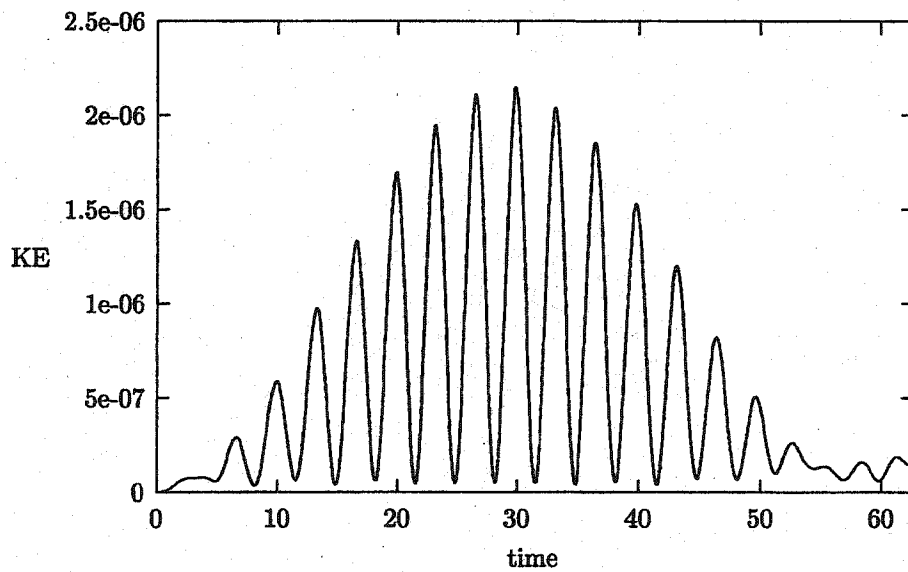


Figure 5-10 Mean kinetic energy in system through 10 cycles.



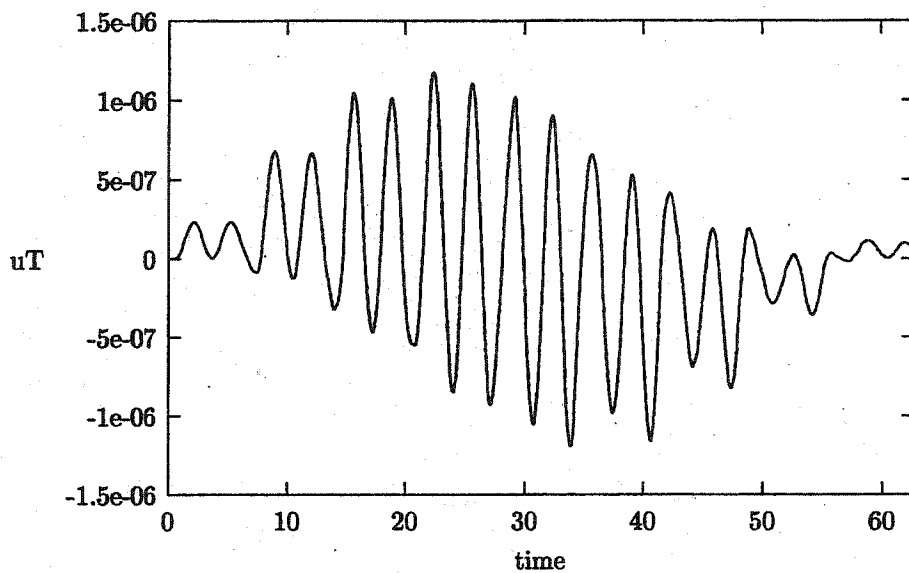


Figure 5-11 Energy flux for ten cycles.

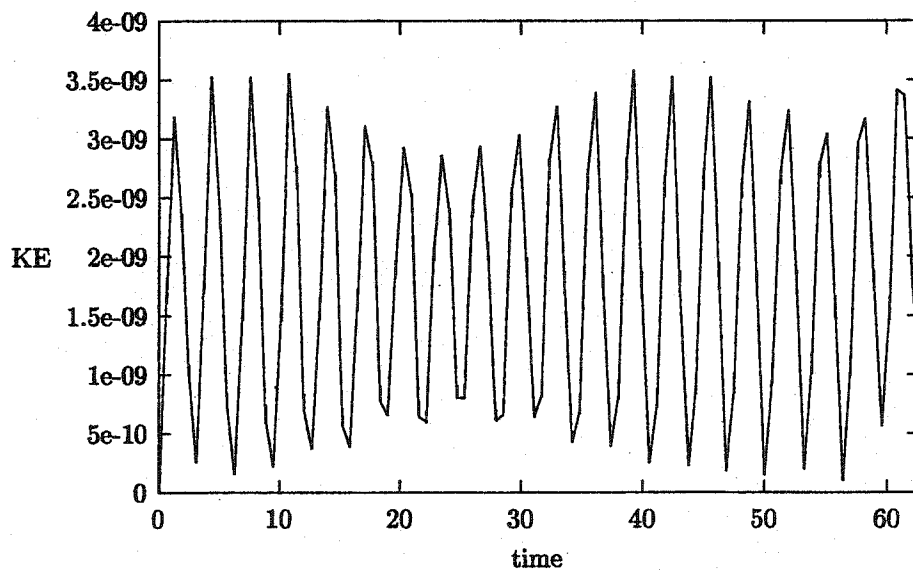
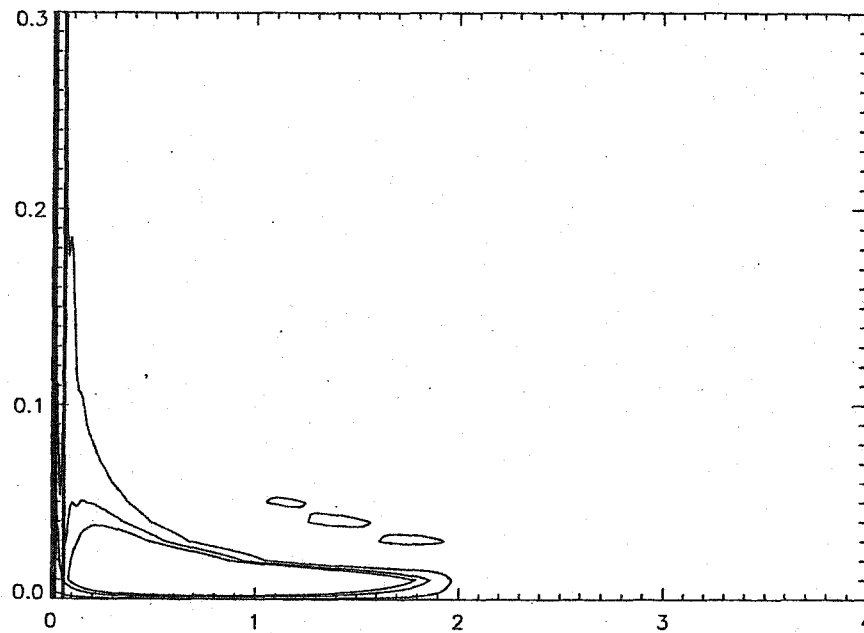
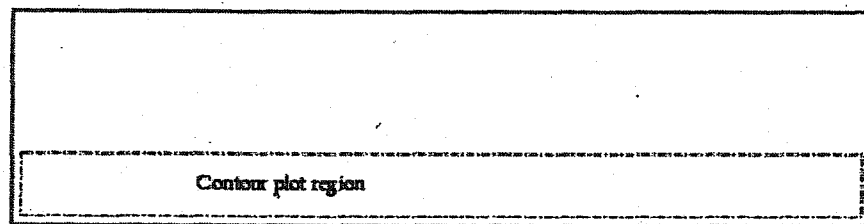


Figure 5-12 Kinetic energy without non-linear terms.

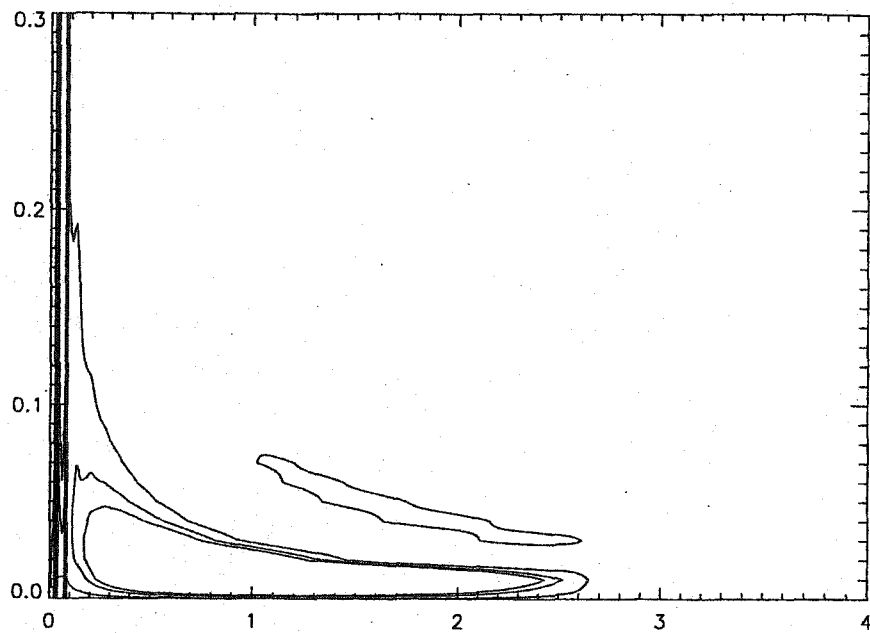


(a) Contour plot at  $t=1.801$

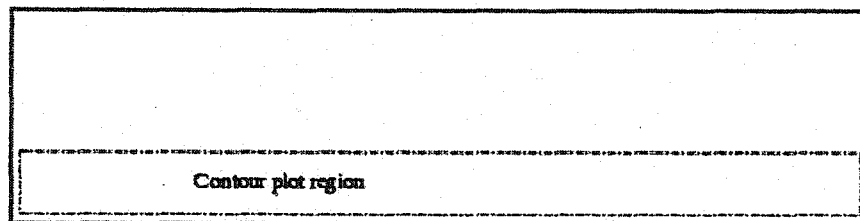


(b) Schematic of entire chamber showing contour plot region

Figure 5-13 Vorticity at  $t=1.801$ .

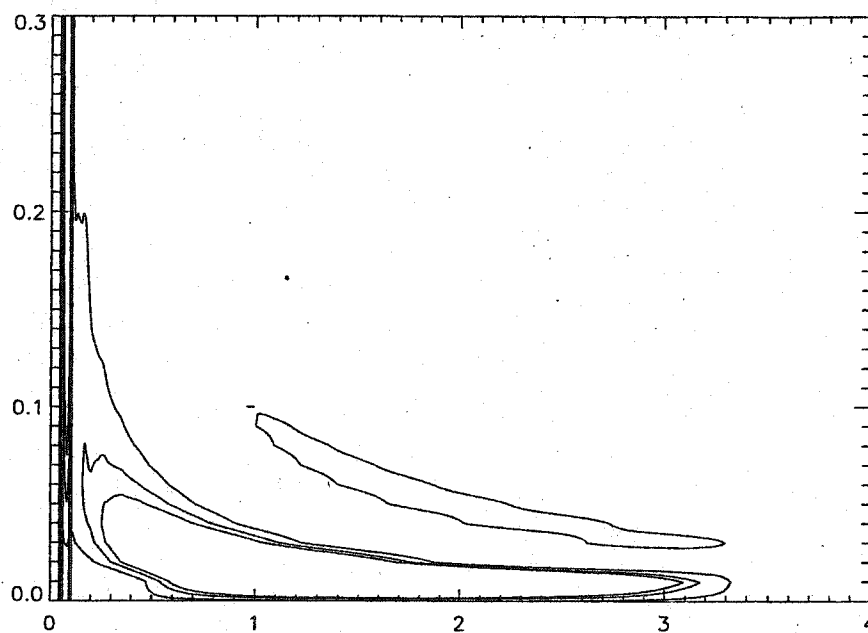


(a) Contour plot at  $t=2.401$

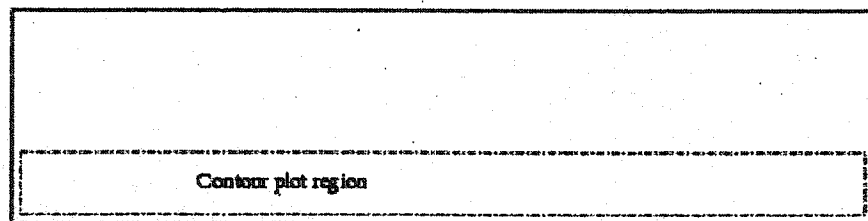


(b) Schematic of entire chamber showing contour plot region

Figure 5-14 Vorticity at  $t=2.401$ .



(a) Contour plot at  $t=3.001$



(b) Schematic of entire chamber showing contour plot region

Figure 5-15 Vorticity at  $t=3.001$ .

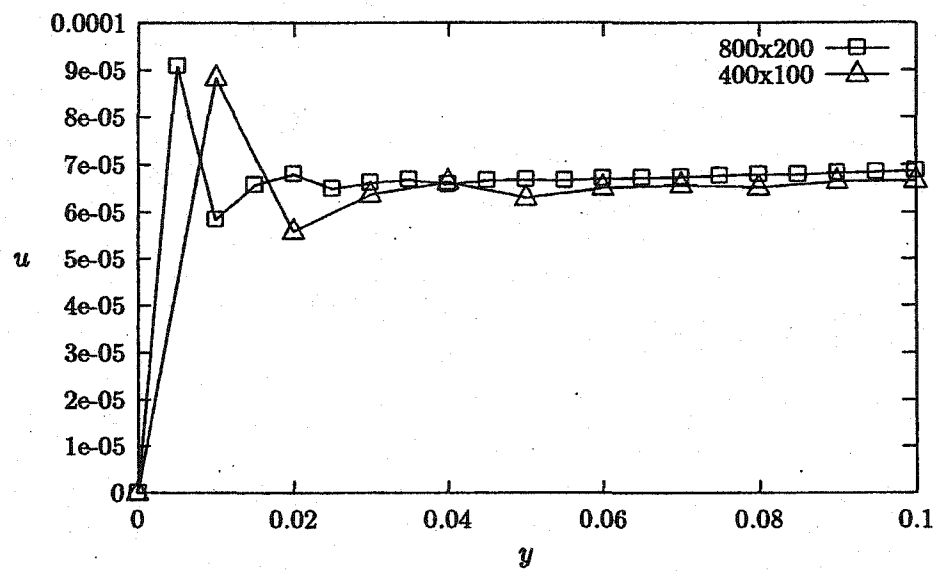
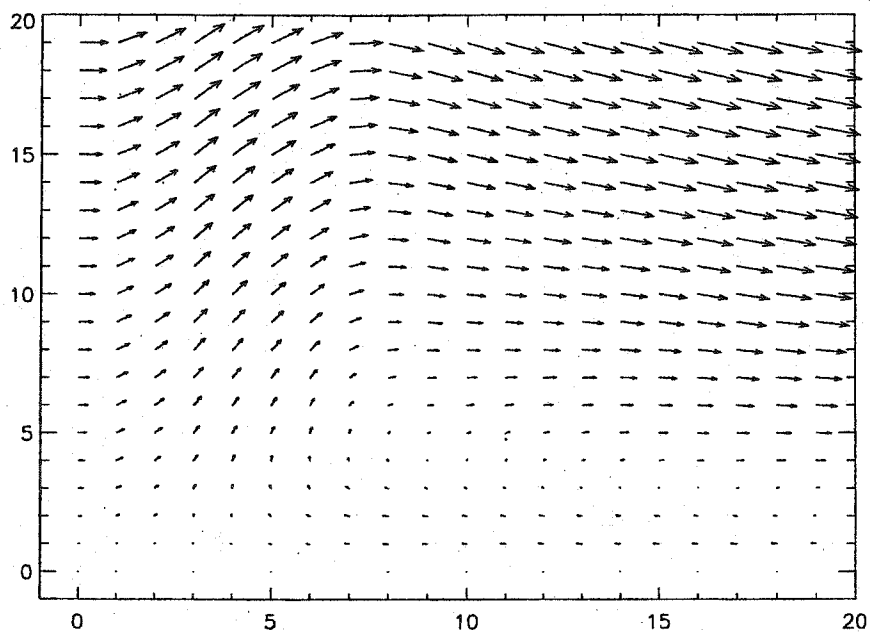
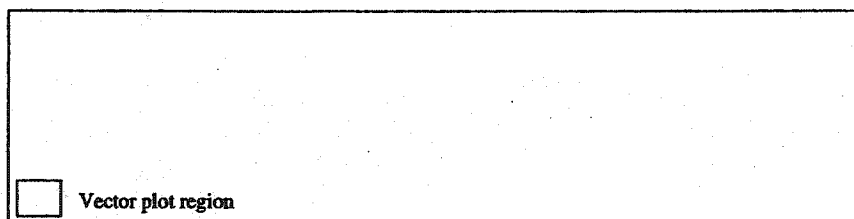


Figure 5-16 Resolution difficulties at high Reynolds number.

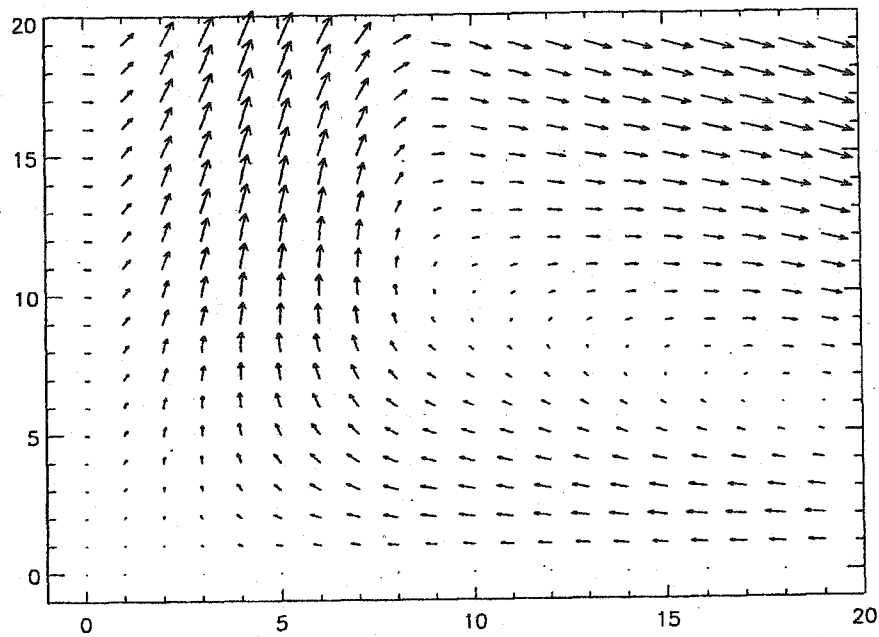


(a) Vector plot at  $t=2.701$

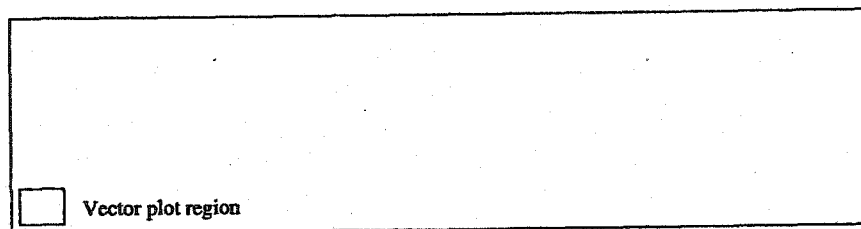


(b) Schematic of entire chamber showing vector plot region

Figure 5-17 Vector plot of vortex flow near membrane at  $t=2.701$ .

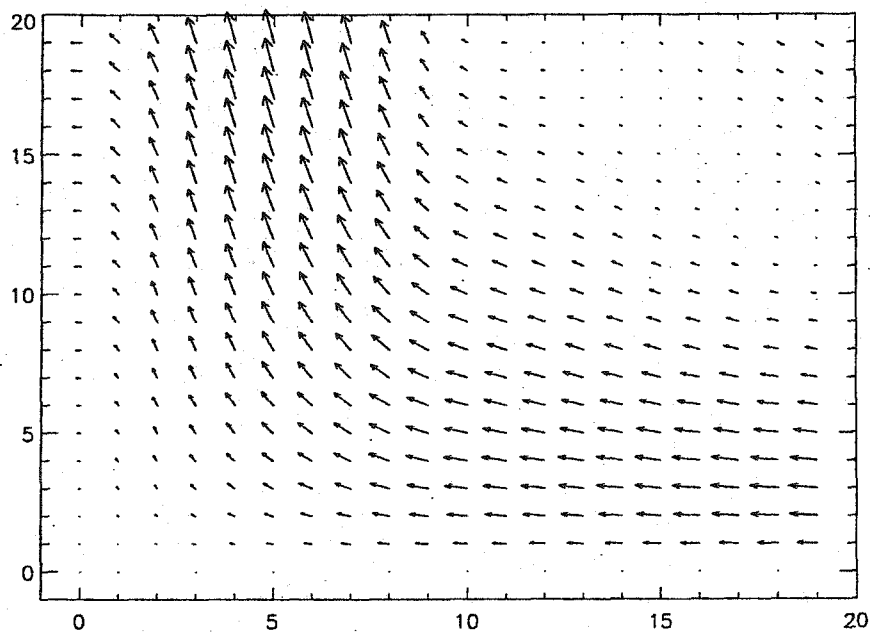


(a) Vector plot at  $t=3.001$

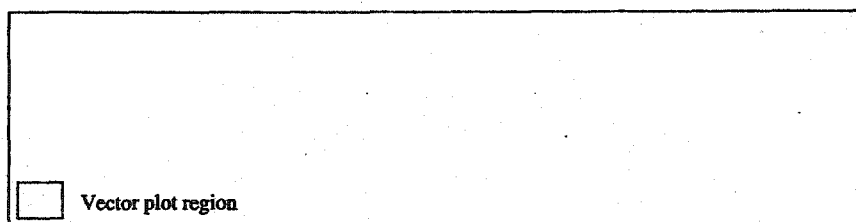


(b) Schematic of entire chamber showing  
vector plot region

Figure 5-18 Vector plot of vortex flow near membrane at  $t=3.001$ .



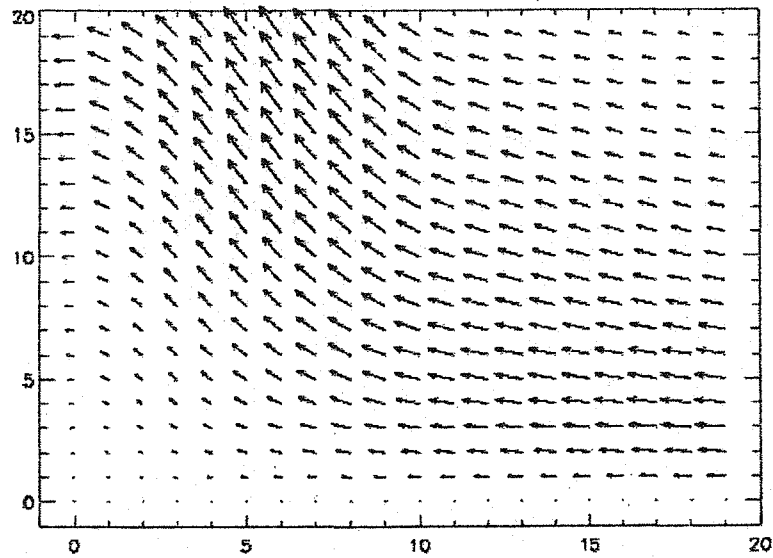
(a) Vector plot at  $t=3.301$



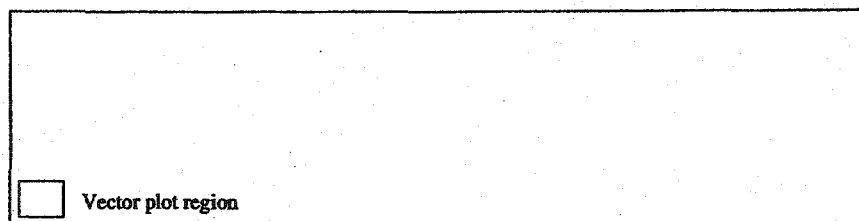
(b) Schematic of entire chamber showing vector plot region

Figure 5-19 Vector plot of vortex flow near membrane at  $t=3.301$ .



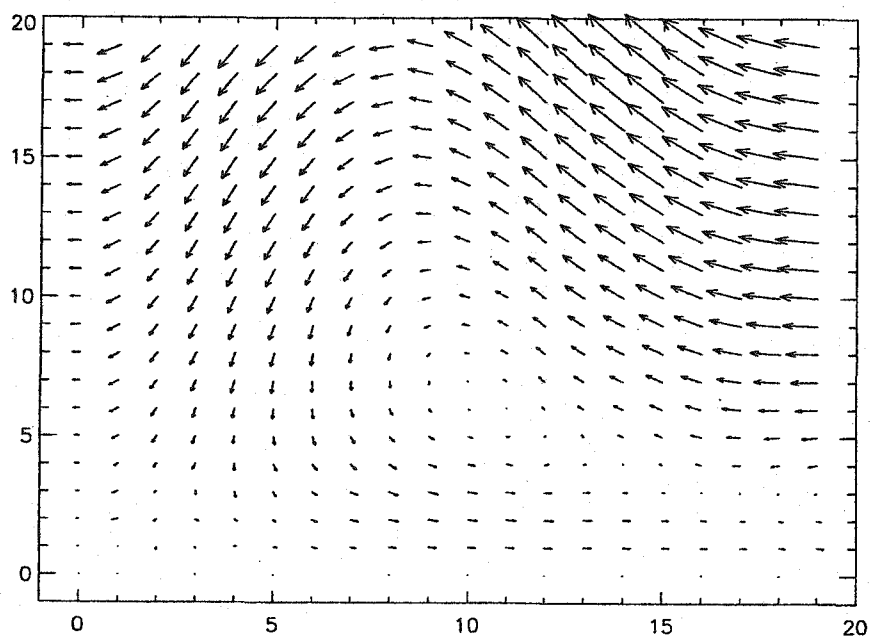


(a) Vector plot at  $t=3.601$

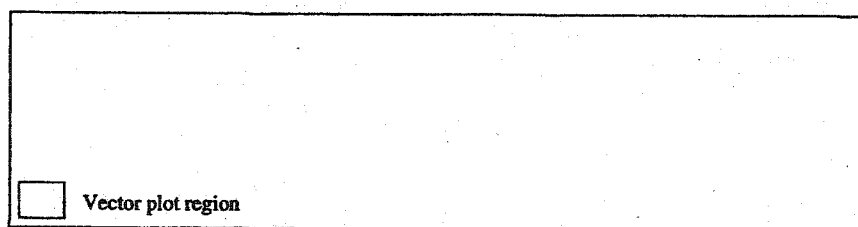


(b) Schematic of entire chamber showing vector plot region

Figure 5-20 Vector plot of vortex flow near membrane at  $t=3.601$ .



(a) Vector plot at  $t=6.001$



(b) Schematic of entire chamber showing  
vector plot region

Figure 5-21 Vector plot of vortex flow near membrane at  $t=6.001$ .

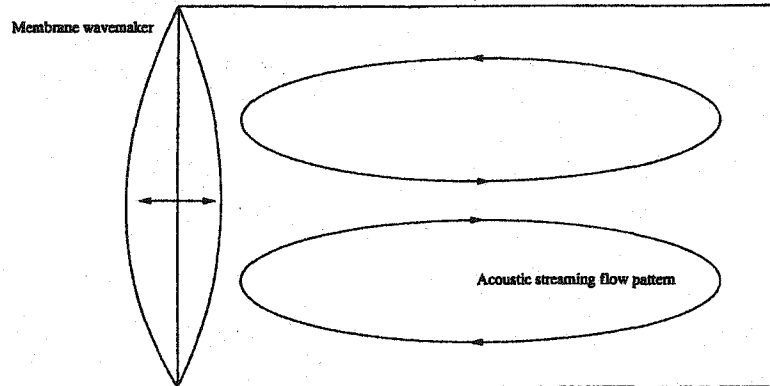


Figure 5-22 Acoustic streaming flow pattern.

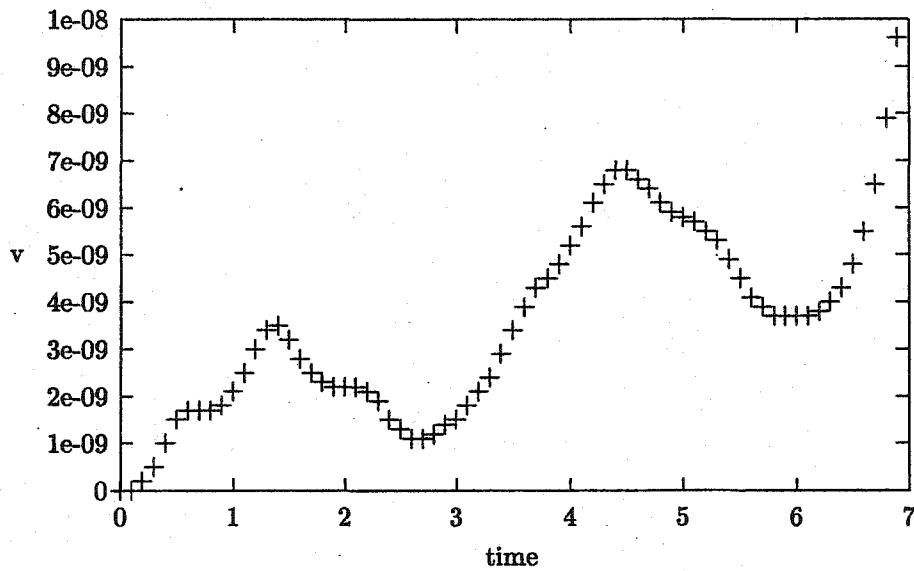


Figure 5-23 Average transverse velocity at  $y=0.75$ .

## Chapter 6

### RESULTS WITH PLATES

#### 6.1 Heat Exchanger Plates

A practical thermoacoustic device includes heat exchanging 'plates' installed in the chamber. Existing theories of thermoacoustic effects, usually based on linear inviscid theory, assumes that the heat exchanger plates do not alter the acoustic field. The effect of the plates on the acoustic waves is considered below. The plates are modeled two ways; thick plates and thin plates. Thick plates are solid material that is motionless but allows conduction, and the temperature of the solid evolves with the motion of the fluid. The boundary conditions are the continuity of temperature, heat flux, and velocity. The thin plates are merely a single row of discrete points, interior to the flow, where zero velocity is imposed. All plates are positioned parallel to the direction of wave propagation.

#### 6.2 Thick plate

The governing equations for the temperature of the plate material is

$$\frac{\partial T_s}{\partial t} = \frac{1}{P_s} \nabla^2 T_s, \quad (76)$$

where  $T_s$  is the temperature of the solid plate material, and

$$P_s = \frac{\omega L^2}{\alpha_s}, \quad (77)$$

$\alpha_s$  being the thermal diffusivity of the plate material. The thermal properties of the plate material are assumed to remain constant, and are chosen to model stainless steel (type 304). The resulting value of  $P_s$  is  $2.247 \times 10^7$ , which is used for all thick plate cases.

Equation (76) is discretized as before. The fluid is initially at rest, the temperature is initially uniform, and waves are forced with a membrane. The parameter values for the simulations are again given in Table 5.1.

The plate employs the same computational grid as the fluid, which is uniform in both directions. Hence the plate boundaries correspond exactly to grid points in the fluid. This method places a limit on the minimum dimension of a plate. The one-sided second order difference schemes for the boundary conditions require three grid points. Therefore, a plate cannot be less than three grid points in size. In practice, good results were obtained only with a minimum of five grid points across a plate.

For example, a typical simulation uses 101 grid points evenly spaced across the chamber. A plate has a minimum thickness of five grid points, or four grid spacings, meaning that the plate thickness is 4% of the chamber height. Actual heat exchanger plates in existing devices have a thickness which is generally less than 1%, which cannot be achieved with the chosen grid. The resolution would have to be increased to 401 points to allow a plate thickness of 1% of the chamber height.

The simulation of the previous section are repeated with a single thick plate installed at the transverse centerline of the chamber. The leading edge of the plate is located at the twentieth gridpoint from the wavemaker (the resolution is  $400 \times 100$ ), and the plate is fifty gridpoints in length and five gridpoints in height.

Example surface plots of axial and transverse velocity are shown in figures 6-1 through

6-4. The results show that the standing wave forms as before, and the secondary flows are still present; beating, crosswaves, corner vortices, and oscillating boundary layers.

In addition, a variety of phenomena appear near the plate that were not present previously. This flow can be seen in the contour plots of vorticity shown in figures 6-5-6-7. Note that the contour plot is only for the lower part of the chamber, as shown in the schematic (bottom of 6-5 through 6-7). The plate has an oscillating boundary layer which forms a cellular flow pattern on both sides of the plate. A close-up view of the flow in this cell near the wavemaker is shown in figures 6-8 through 6-12 with vector plots. The vector plots clearly show a vortical flow. Note that the time of figures 6-8 and 6-9 is  $t=2.701$ ,  $3.001$ , which is early in the simulation, corresponding to the initial wave shortly before it impacts the opposite wall. Hence the axial velocity of the incident wave is positive, and the wavemaker velocity is positive but approaching zero.

Note in figure 6-8 that the region near the plate, which is located at the top of this figure, shows a negative axial velocity (flow to the left in the figure). This is despite the positive axial velocity of the incident wave. Note in these figures the evolution of the vortex. It appears to move away from the plate and the wavemaker. Figure 6-12, which corresponds to  $t=6.001$ , is opposite in direction to that of figure 6-9 which is computed approximately half an acoustic cycle earlier.

Vortex motion at the bottom left corner of the chamber near the membrane can be seen in figure 6-7, as in the case without a plate. The cellular flow pattern progresses as discussed earlier.

The 'wake' region directly downstream of the plate is a region of intensely complicated flow, as shown with vector plots in figures 6-13 and 6-14. Figure 6-13 show that this flow

can be simple laminar flow at times. However, vortex shedding from each side of the plate can complicate the flow dramatically, as shown in figure 6-14. Note that figures 6-13 and 6-14 differ only in time by a fraction of a wave period.

The surface heat flux,

$$q = -\frac{\partial T}{\partial y},$$

is an important quantity in thermoacoustics. It measures the efficiency of heat transfer between fluid and solid. Figure 6-15 shows the heat flux along the plate surface for the above case. Note that  $q$  has a sharp 'kink' near the end of the plate, which has been explained analytically by Swift[4] and reported by Cao et al. [7]. Cao et al. observed no smoothing of the peak even with a highly resolved computational grid. This trend in heat flux near the plate edge may be related to the fact that the fluid near the plate ends is advected beyond the end of the plate for part of the acoustic cycle.

Note that the single thick plate located at the transverse center is found to have equal heat flux on both the top and bottom surfaces. Repositioning the plate at the same axial coordinate but different transverse location results in the heat flux no longer being equal on the top and bottom surface. However, it is interesting to note that the sum of the heat flux through the top and bottom surfaces is independent of the position.

### 6.3 Thin plates

Consider a single thin plate, located in the same position as the single thick plate of the previous section. Surface plots of the horizontal velocity are shown in figures 6-16 through 6-19. The dynamics of the acoustic wave with the thin plate closely match the results with

the thick plate, as can be seen by comparing the surface plots in figures 6-1 to 6-4 and 6-16 to 6-19. This indicates that the thin plate approximation, which does not alter the temperature profile directly, is a useful plate model for overall dynamics of the acoustic wave. The similarity in the results between thick and thin plates models can also be seen in the diagnostic quantities, shown for both thick and thin plate cases in figures 6-20 to 6-22. Note that the two curves in each of these figures are indistinguishable.

The boundary layer flow on either side of the thin plate develops in a manner similar to the thick plate. This can be seen by comparing the contour and vector plots for the thin plate, figures 6-23 to 6-30, with the equivalent plot for the thick plate, figures 6-5 to 6-12.

Significant differences do appear directly behind the plates. Figures 6-31 and 6-32 show a vector plot of the region directly behind the thin plate, corresponding to figures 6-13 and 6-14, which show the same region at the same times behind the thick plate. The flow appears to be strikingly different. Both cases show flow reversal (negative axial velocity), although one must look closely at figure 6-32 to see leftward pointing vectors, and both cases are symmetric about the chamber axial centerline. But clearly the flow behind the thick plate shows much more complicated flow, and stronger flow reversal. The flow reversal may be understood by noting in figure 6-14 that two symmetric counterrotating shed vortices are present, with centers approximately eleven gridpoints 'downstream' of the plate. These counterrotating vortices appear to induce the strong flow leftward behind the plate.

#### 6.4 Multiple thin plates

One advantage of the thin plate model is the ease with which multiple plates may be included. No additional computational resources are required, and high quality results may



be obtained with modest resolution.

Figure 6-33 shows a contour plot of the vorticity for the entire chamber with five thin plates, equally spaced across the chamber. Figure 6-33 clearly shows the developing boundary layer on each side of each plate, and the boundary layer along the top and bottom wall. Note that contours for the center plate are longer than the contours for the other plates. This is due to the membrane wavemaker, which forces a larger axial velocity at the center.

An important measure of the performance of a heat exchanger plate is the temperature difference between the ends of the plate. Figure 6-34 shows the temperature difference for the first ( $\diamond$ ), second (+), and third (\*) plate in the 5-plate stack for plate length of 0.2. The next 2 are symmetrical with respect to the chamber centerline. Several plate lengths are tried. The plate length of 0.3 generates the highest temperature difference. However, further analysis reveals that a length of 0.2 gives the maximum temperature difference when the results for the five plates are averaged.

The position of the plates is considered by repeating the simulations with the plates in different horizontal positions along the chamber. The results are shown in figure 6-35. Note that the temperature difference increases monotonically as the plates are moved closer to the wavemaking membrane. However, this effect is only important very close to the membrane, and position is not important elsewhere. Note that the plate length was 0.2 for the results in figure 6-35.

Consider a fixed plate length and axial position, but vary the number of plates. Figure 6-36 show temperature difference as a function of number of plates. Only the temperature difference for the center plate is shown. The plate position is 0.2.

The axial velocity between plates is shown in figure 6-37 for two cases: 9 plates and

2 plates. Note the difference in the profiles. The nine plate case resembles the laminar parallel Poiseuille flow profile for steady flow between parallel plates, while the two plate case has a bulk flow with distinct boundary layer on each side.

Corresponding temperature profiles are shown in figure 6.4. Again, the two plate case shows distinct boundary layers, and more importantly, a much steeper temperature gradient normal to the plate surface. Hence, a narrower plate gap not only restricts the flow between plates, but also reduces the heat flux between plate and fluid.

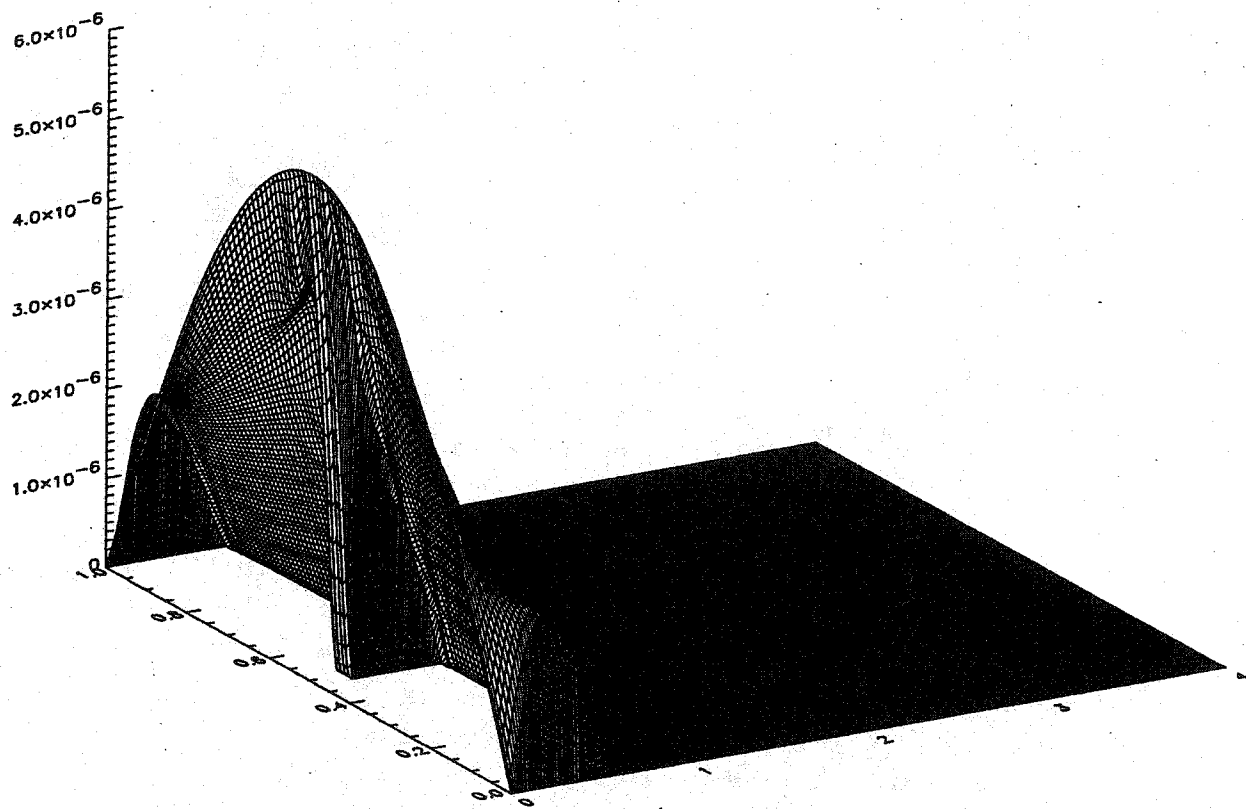


Figure 6-1 Axial velocity at  $t=0.601$ .

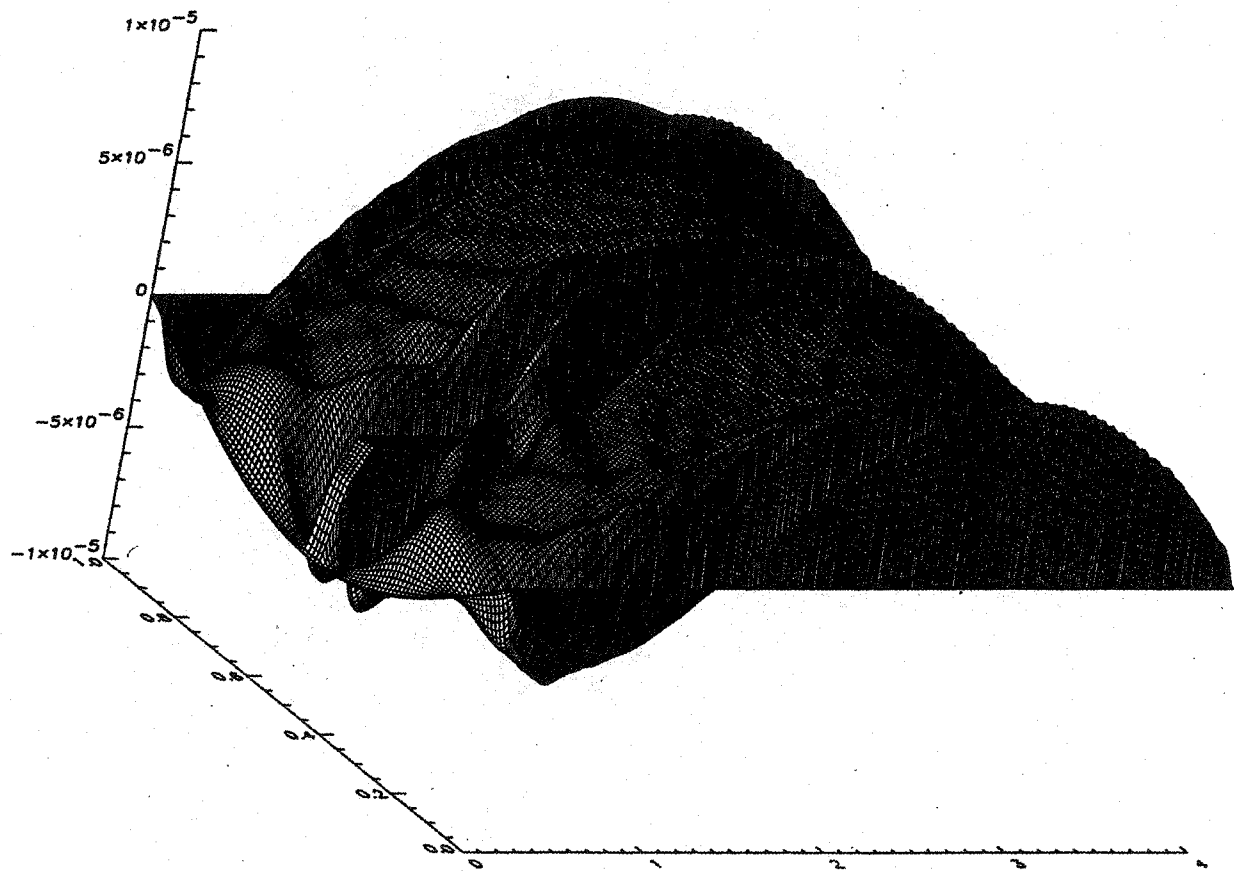


Figure 6-2 Axial velocity at  $t=3.601$ .

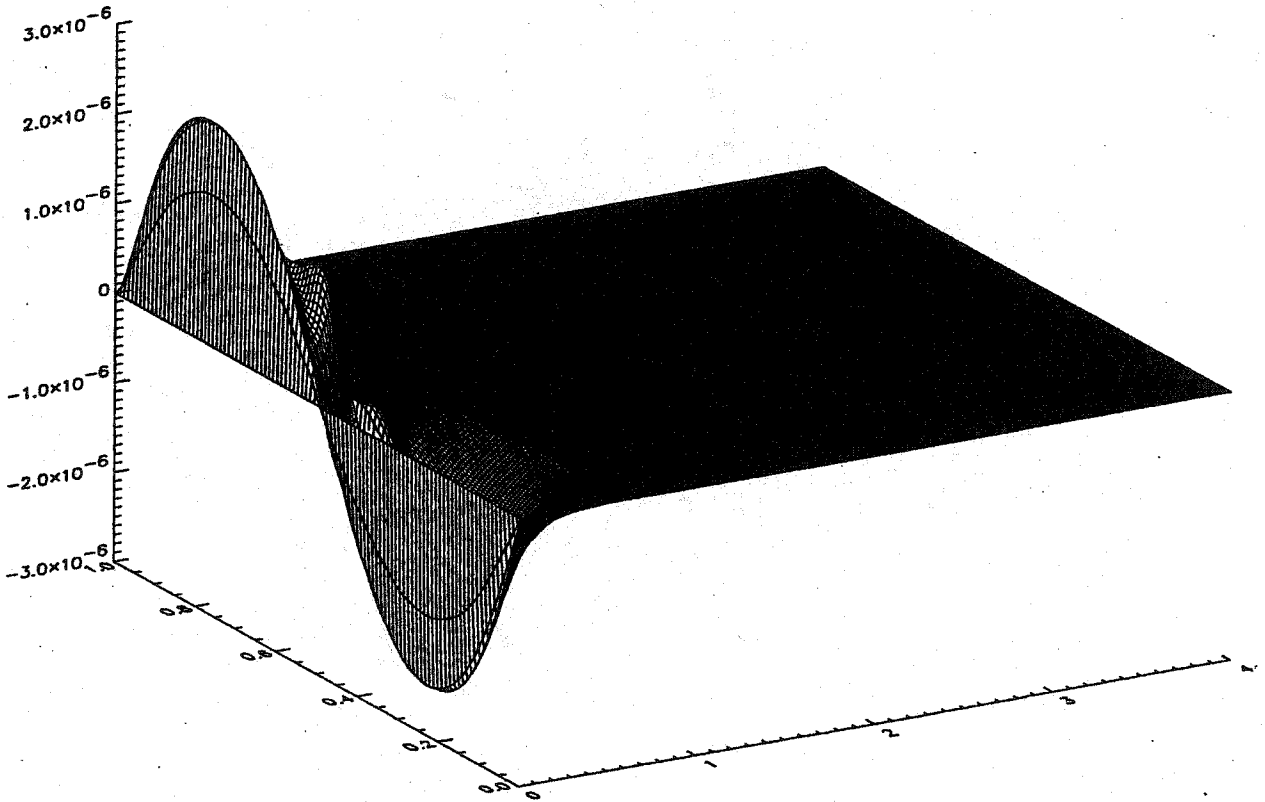


Figure 6-3 Transverse velocity at  $t=0.601$ .

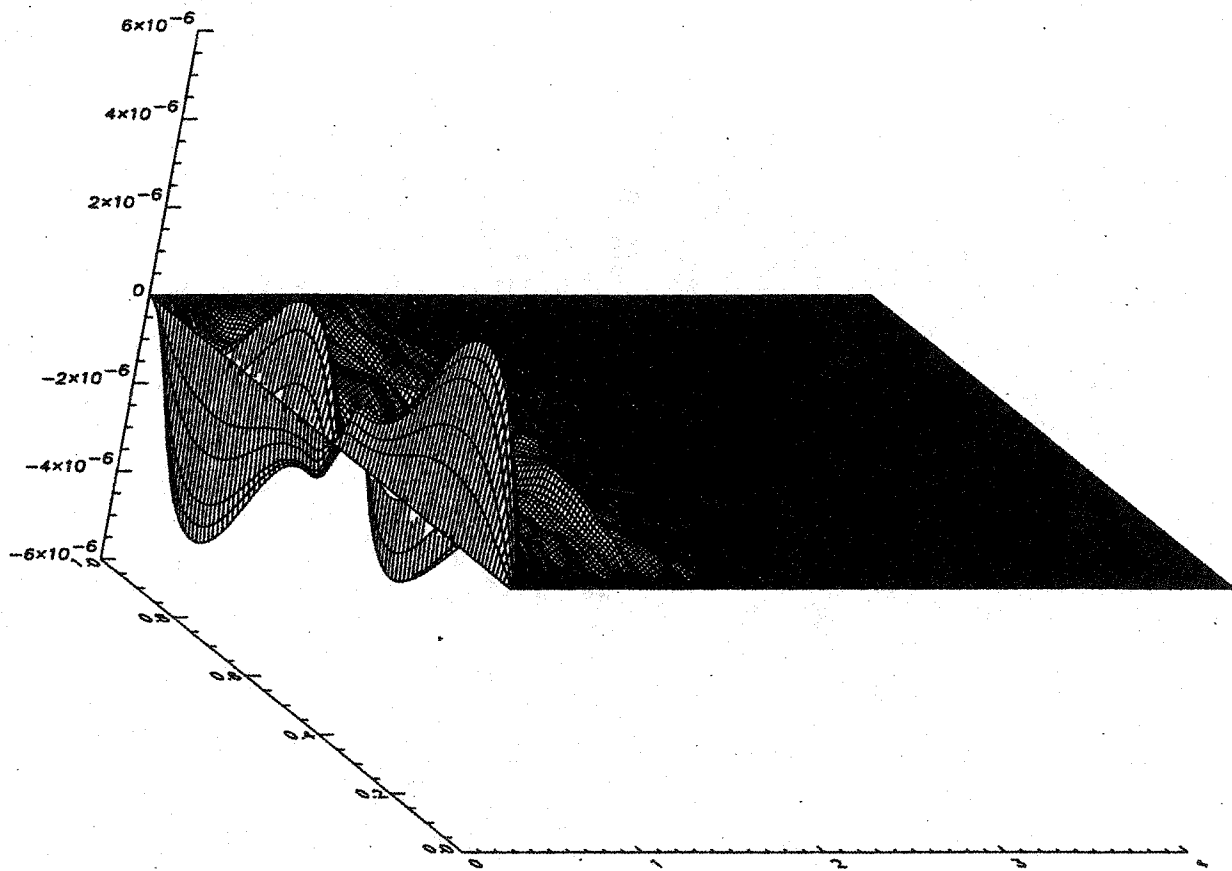
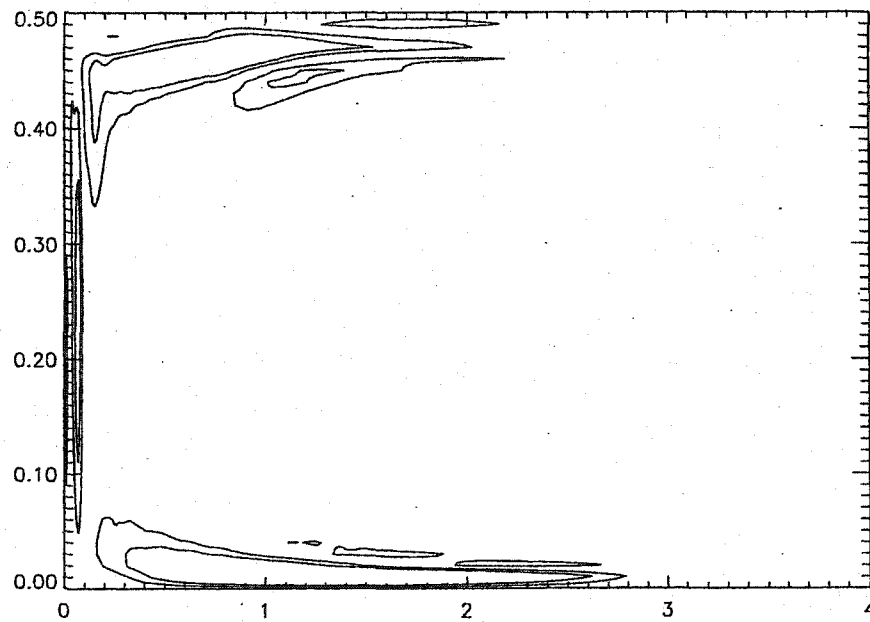
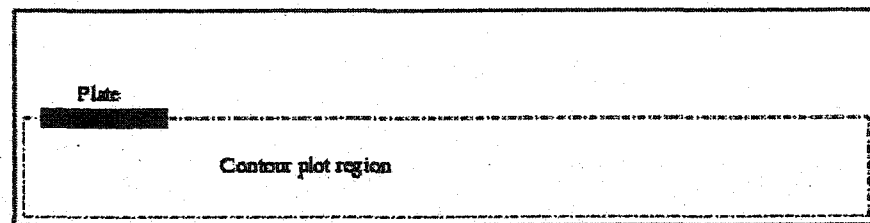


Figure 6-4 transverse velocity at  $t=3.601$ .

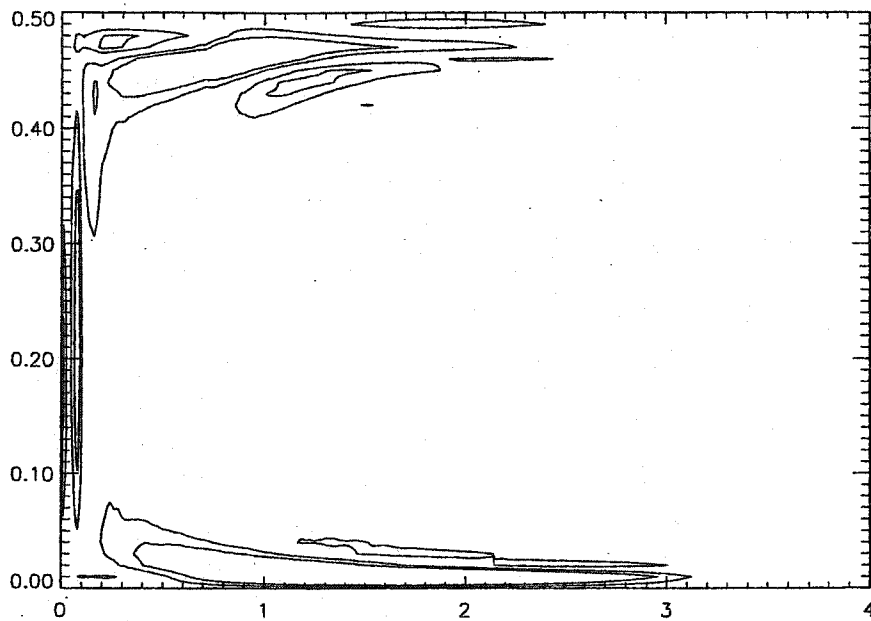


(a) Contour plot at  $t=2.701$

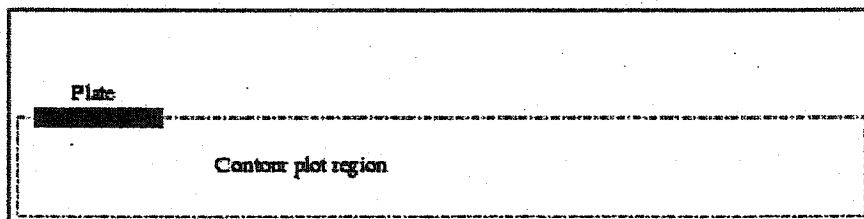


(b) Schematic of entire chamber showing contour plot region

Figure 6-5 Vorticity contour for lower half of chamber at  $t=2.701$ .



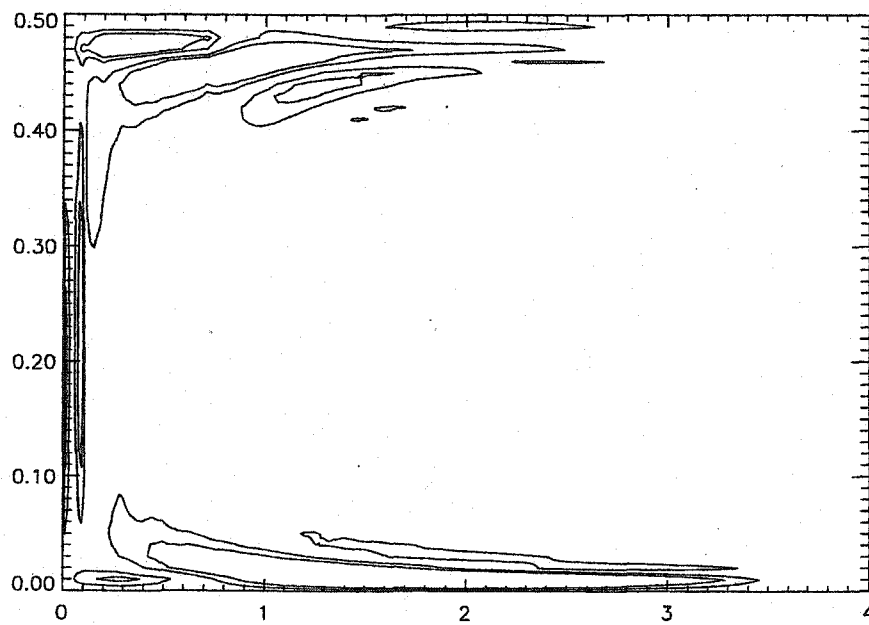
(a) Contour plot at  $t=3.001$



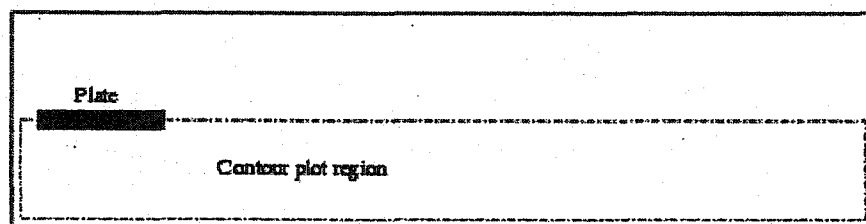
(b) Schematic of entire chamber showing contour plot region

Figure 6-6 Vorticity contour for lower half of chamber at  $t=3.001$ .



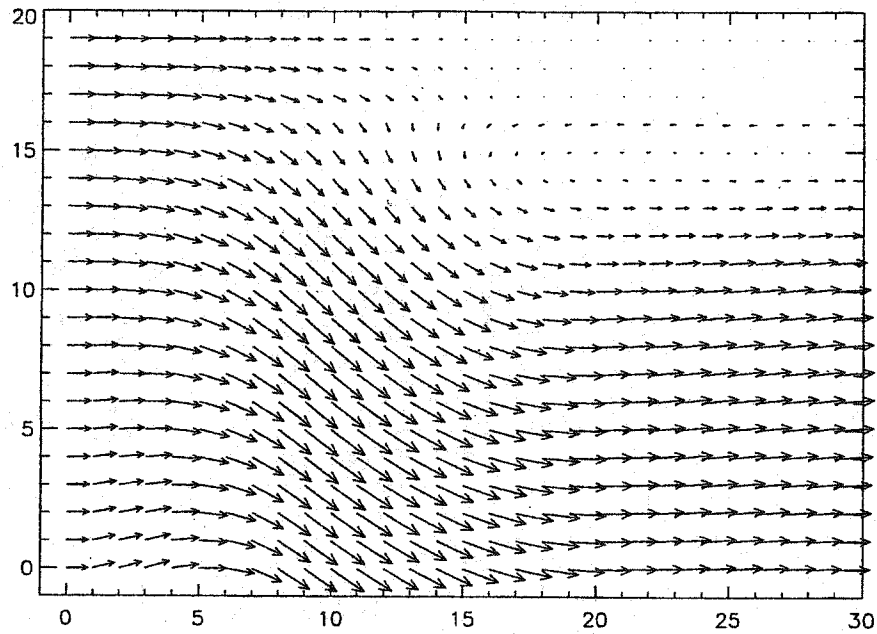


(a) Contour plot at  $t=3.301$

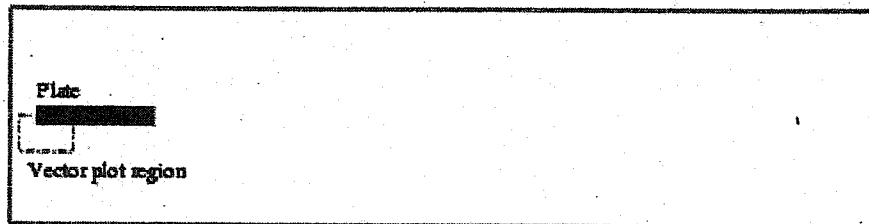


(b) Schematic of entire chamber showing contour plot region

Figure 6-7 Vorticity contour for lower half of chamber at  $t=3.301$ .

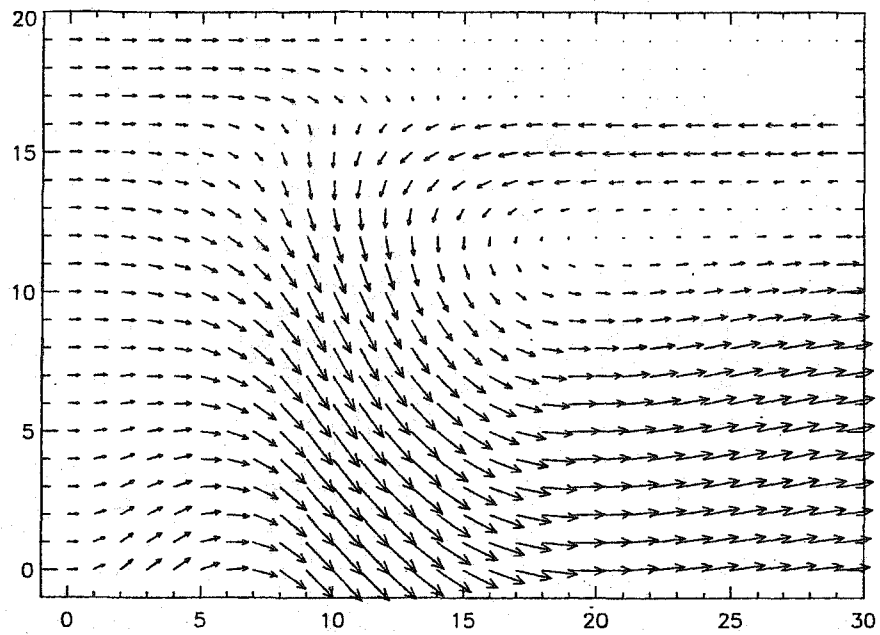


(a) Vector plot at  $t=2.701$

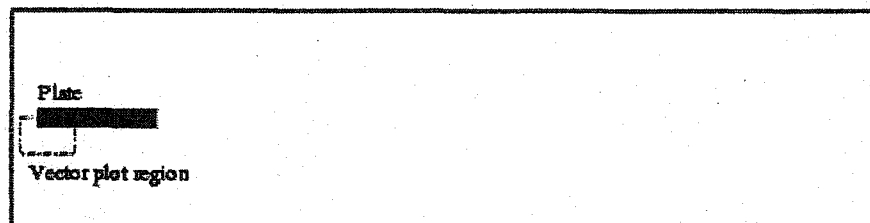


(b) Schematic of entire chamber showing vector plot region

Figure 6-8 Vector plot near front of plate at  $t=2.701$ .

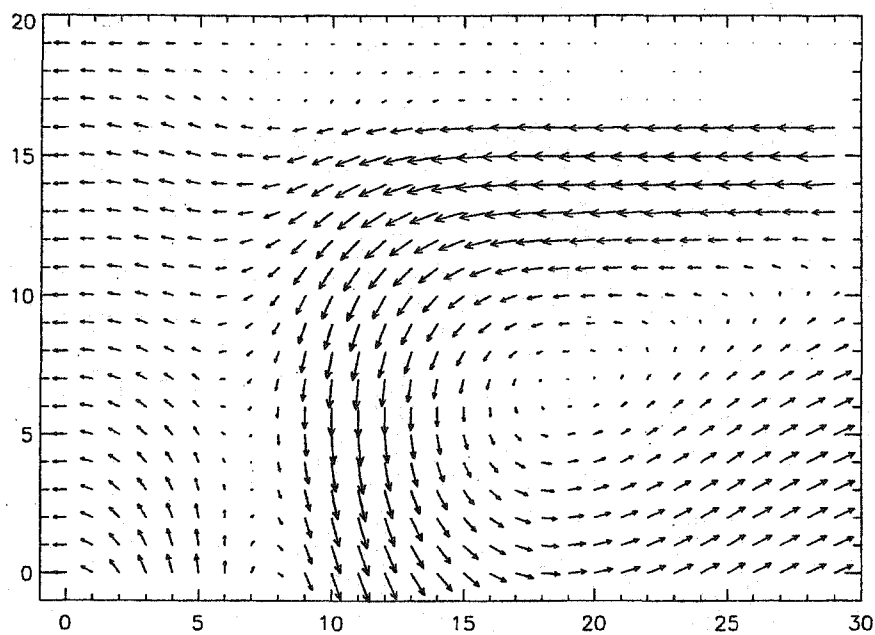


(a) Vector plot at  $t=3.001$

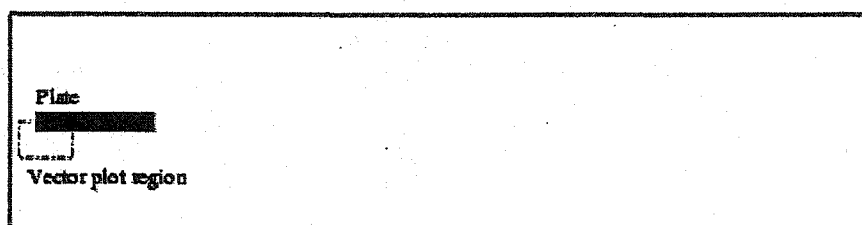


(b) Schematic of entire chamber showing vector plot region

Figure 6-9 Vector plot near front of plate at  $t=3.001$ .

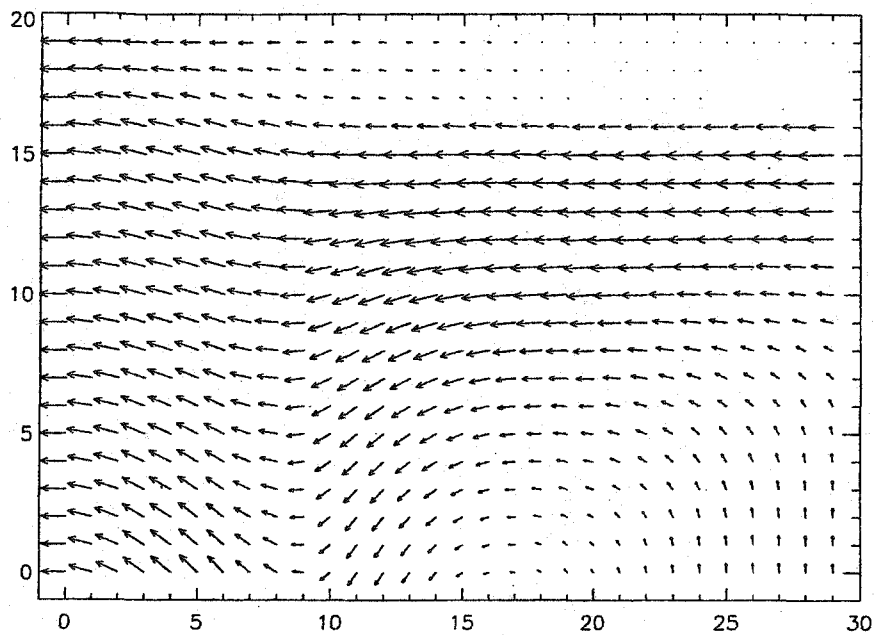


(a) Vector plot at  $t=3.301$

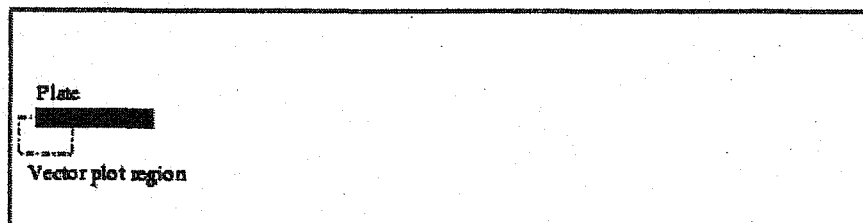


(b) Schematic of entire chamber showing vector plot region

Figure 6-10 Vector plot near front of plate at  $t=3.301$ .

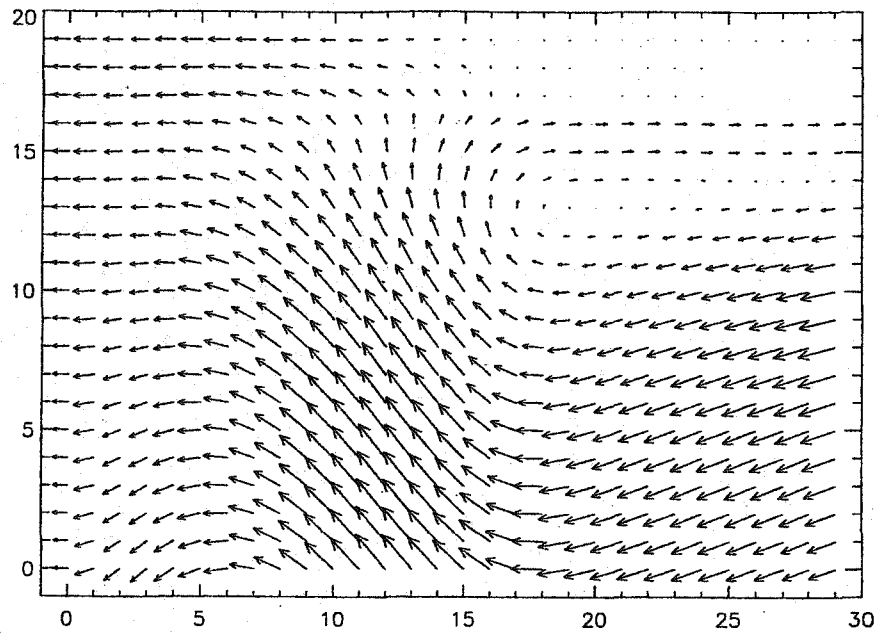


(a) Vector plot at  $t=3.601$

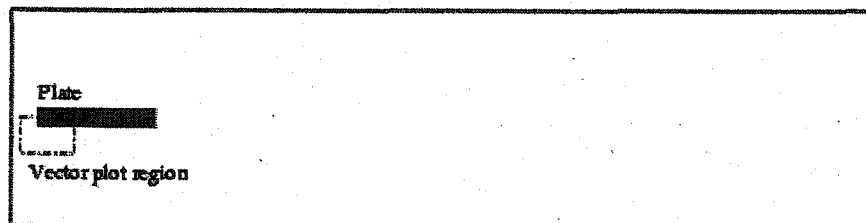


(b) Schematic of entire chamber showing vector plot region

Figure 6-11 Vector plot near front of plate at  $t=3.601$ .

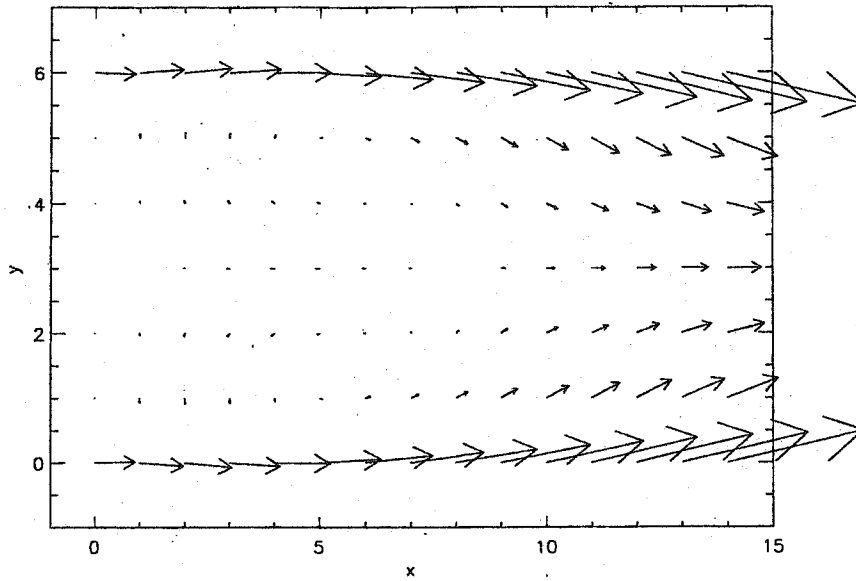


(a) Vector plot at  $t=6.001$

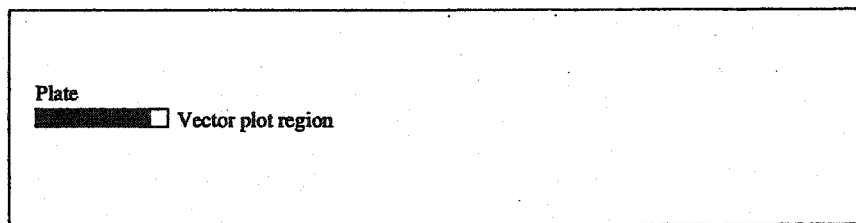


(b) Schematic of entire chamber showing vector plot region

Figure 6-12 Vector plot near front of plate at  $t=6.001$ .

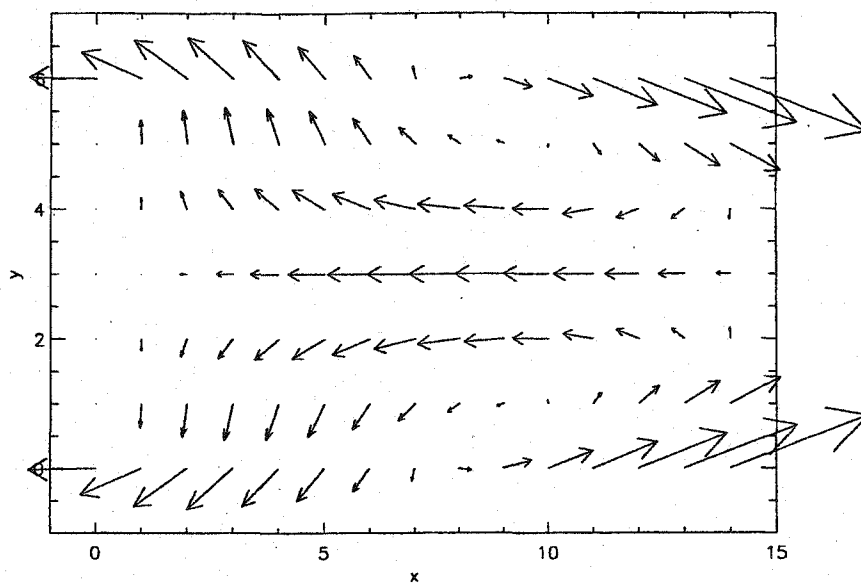


(a) Vector plot at  $t=2.701$

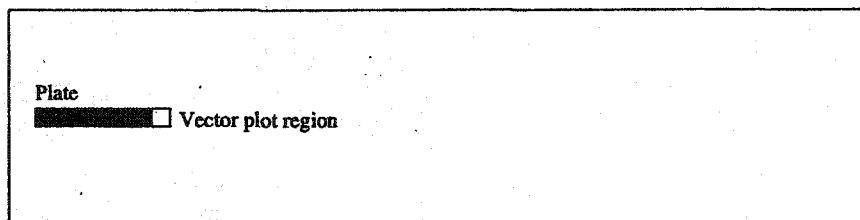


(b) Schematic of entire chamber showing vector plot region

Figure 6-13 Vector plot behind plate at  $t=2.701$ .



(a) Vector plot at  $t=3.001$



(b) Schematic of entire chamber showing vector plot region

Figure 6-14 Vector plot behind plate at  $t=3.001$ .



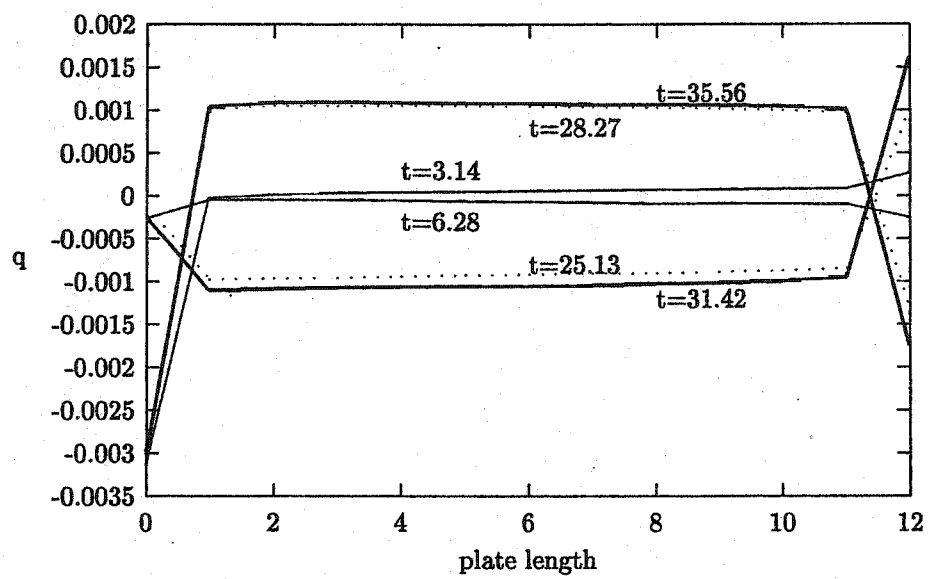


Figure 6-15 Surface heat flux.

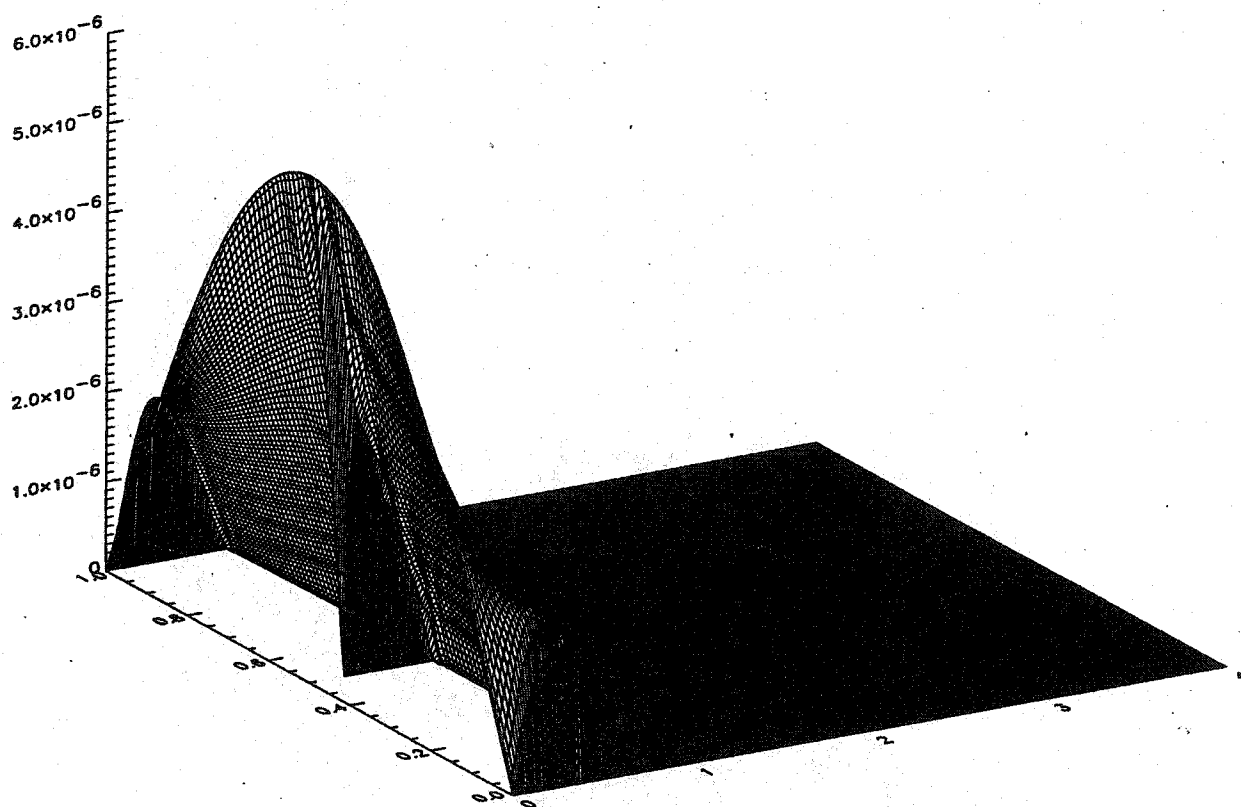


Figure 6-16 Axial velocity at  $t=0.601$ .

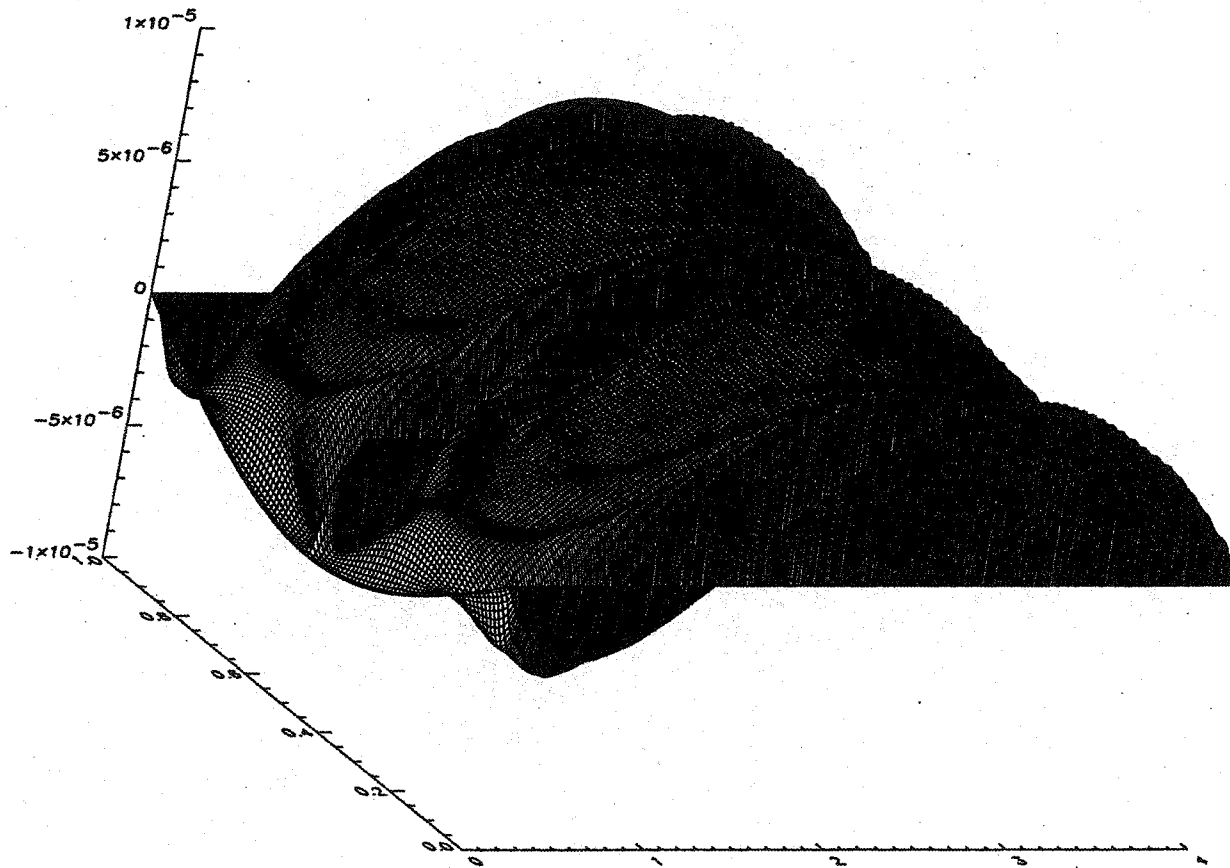


Figure 6-17 Axial velocity at  $t=3.601$ .

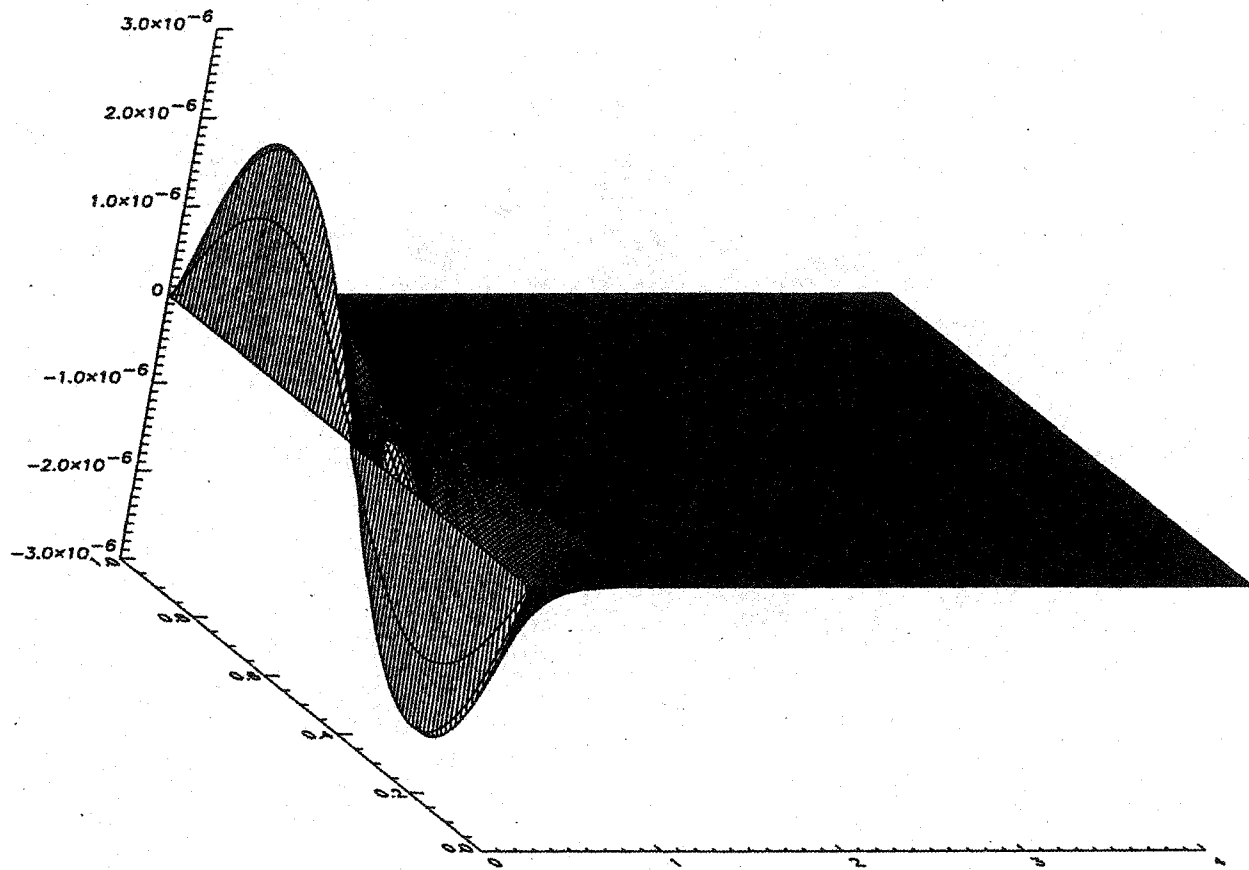


Figure 6-18 Transverse velocity at  $t=0.601$ .

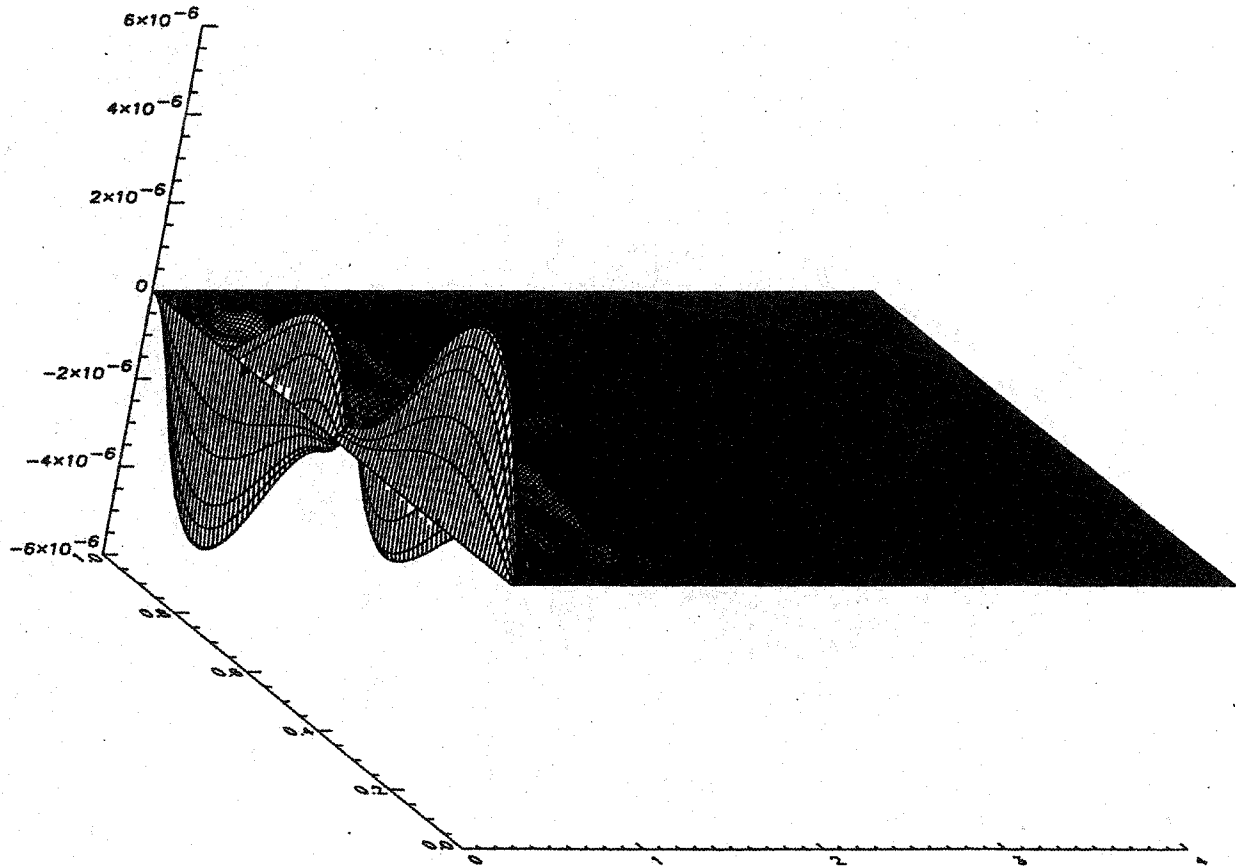


Figure 6-19 Transverse velocity at  $t=3.601$ .

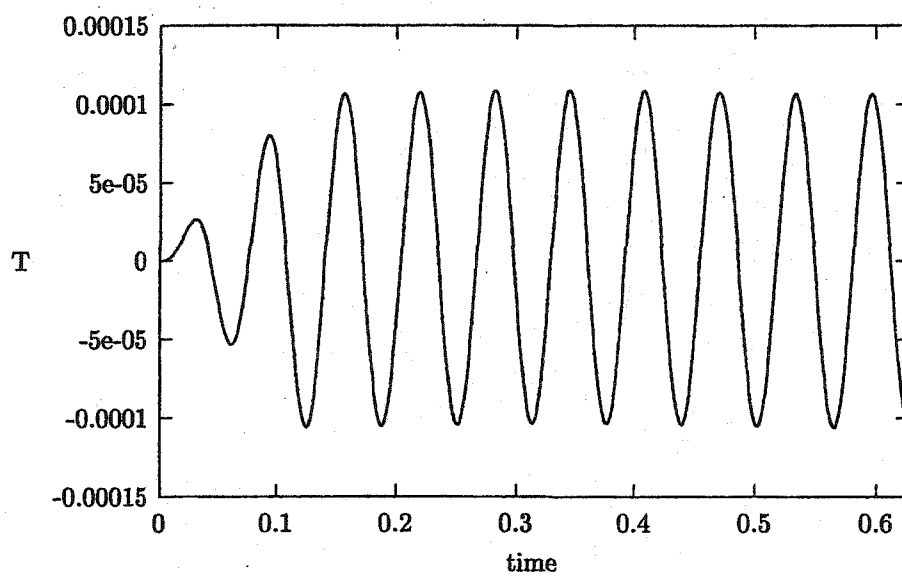


Figure 6-20 Mean temperature in chamber.

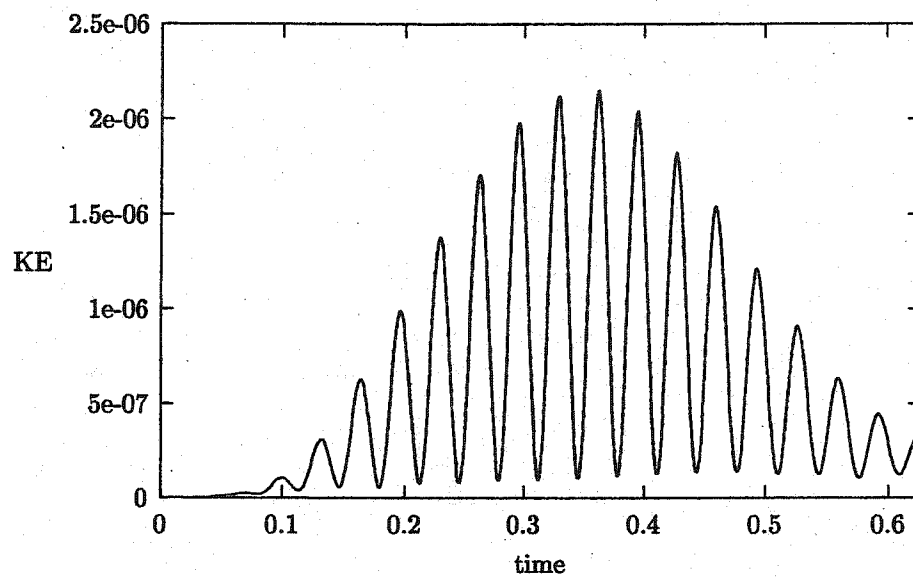


Figure 6-21 Kinetic energy in chamber.

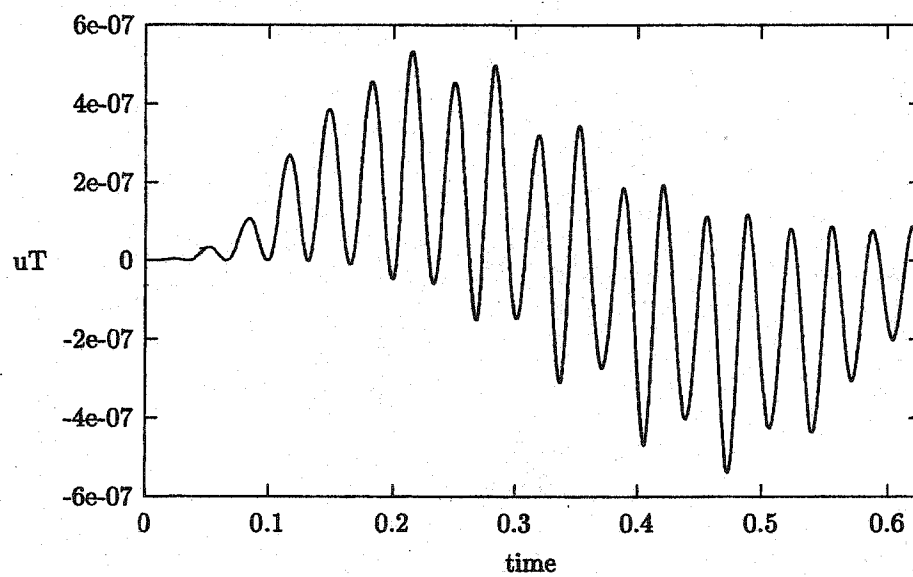
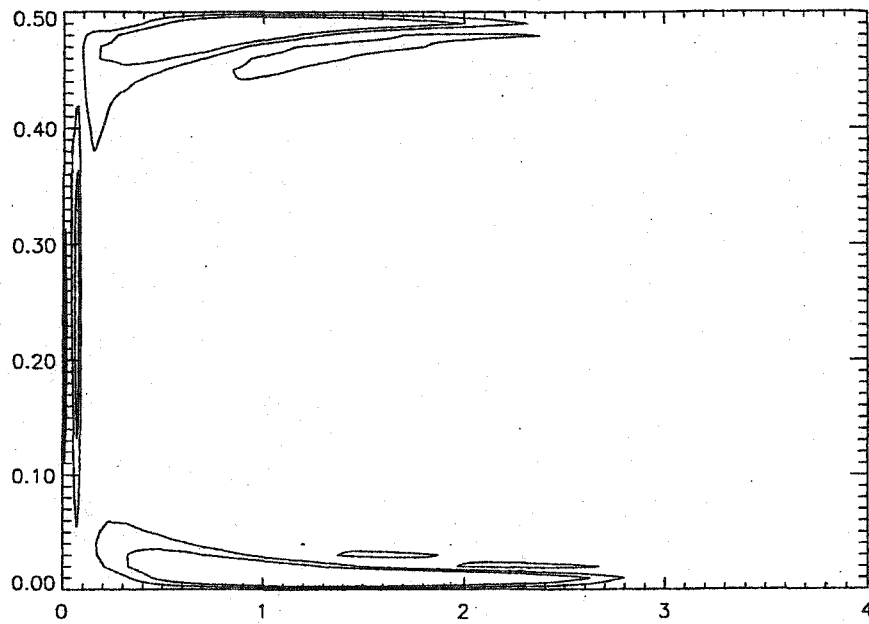
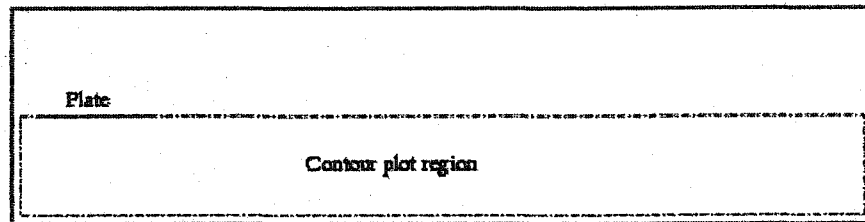


Figure 6-22 Heat flux at  $x=0.15$ .



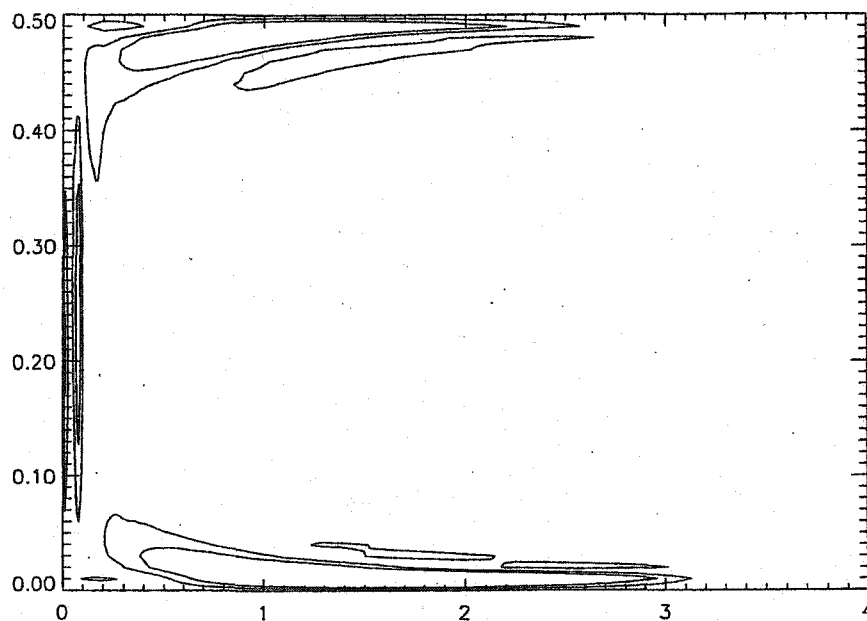
(a) Contour plot at  $t=2.701$



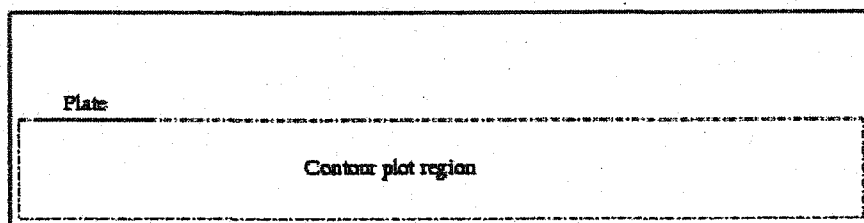
(b) Schematic of entire chamber showing contour plot region

Figure 6-23 Vorticity contour for lower half of chamber at  $t=2.701$ .



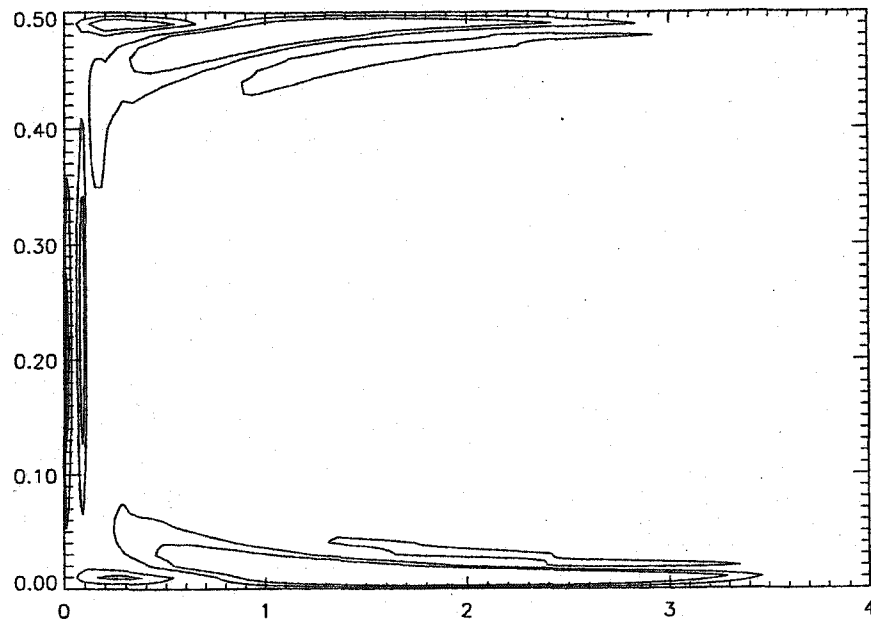


(a) Contour plot at  $t=3.001$

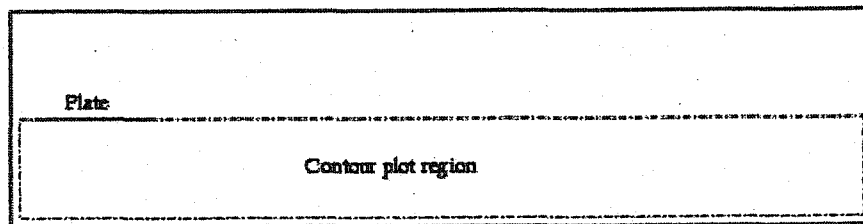


(b) Schematic of entire chamber showing contour plot region

Figure 6-24 Vorticity contour for lower half of chamber at  $t=3.001$ .

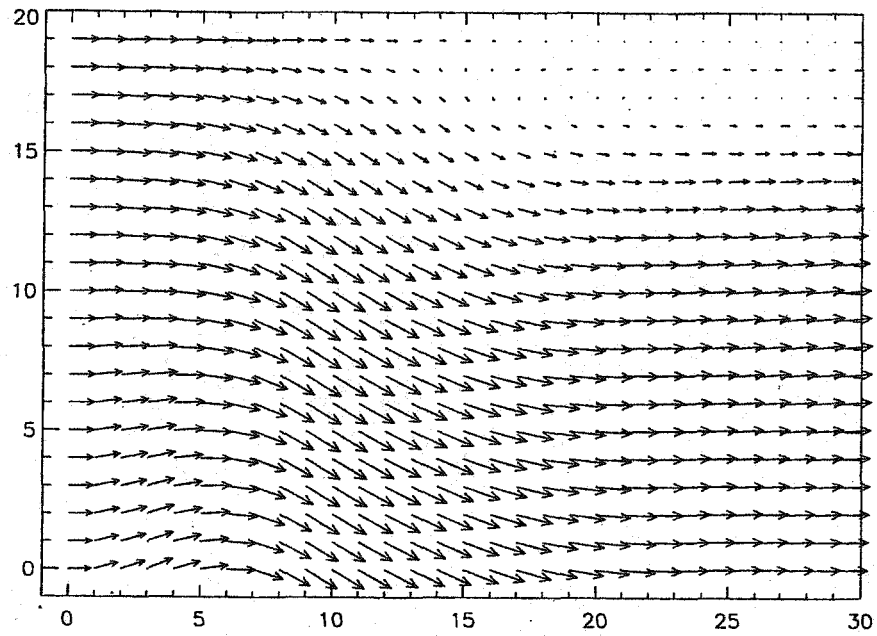


(a) Contour plot at  $t=3.301$

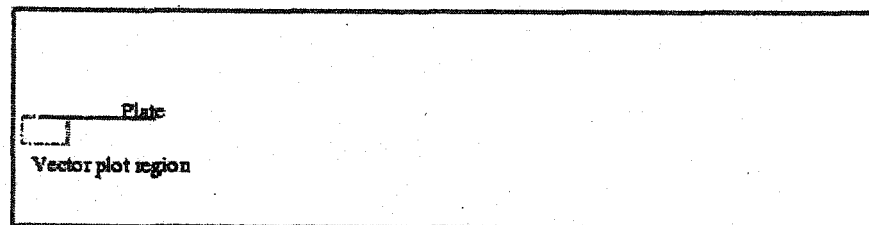


(b) Schematic of entire chamber showing contour plot region

Figure 6-25 Vorticity contour for lower half of chamber at  $t=3.301$ .

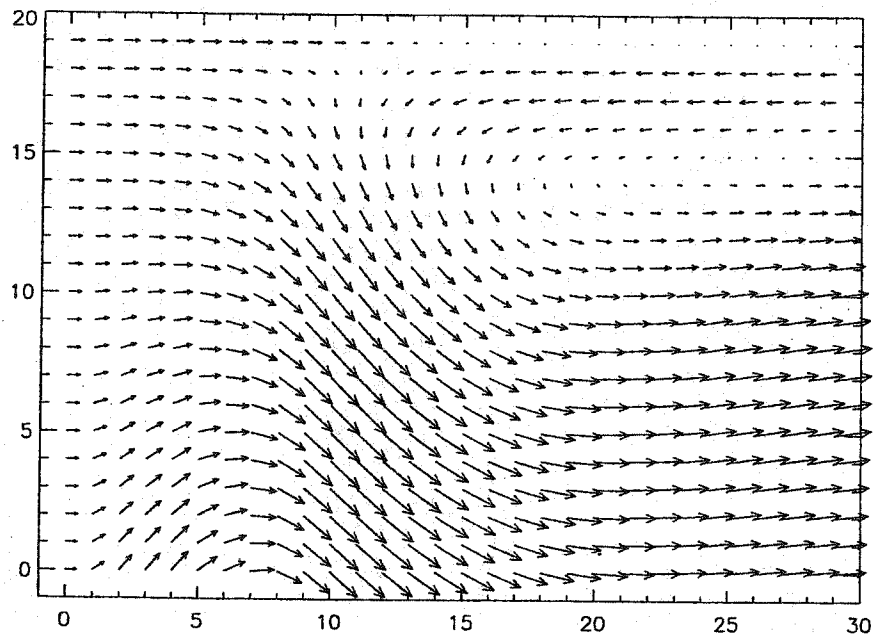


(a) Vector plot at  $t=2.701$

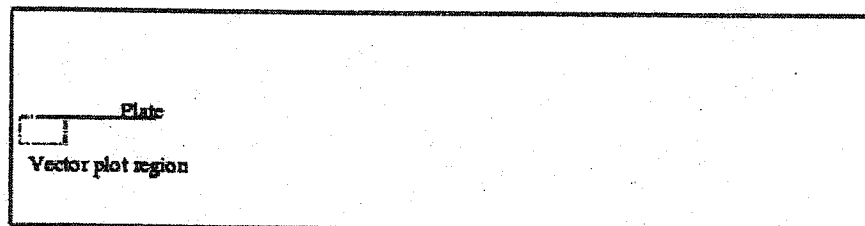


(b) Schematic of entire chamber showing vector plot region

Figure 6-26 Vector plot near front of plate at  $t=2.701$ .

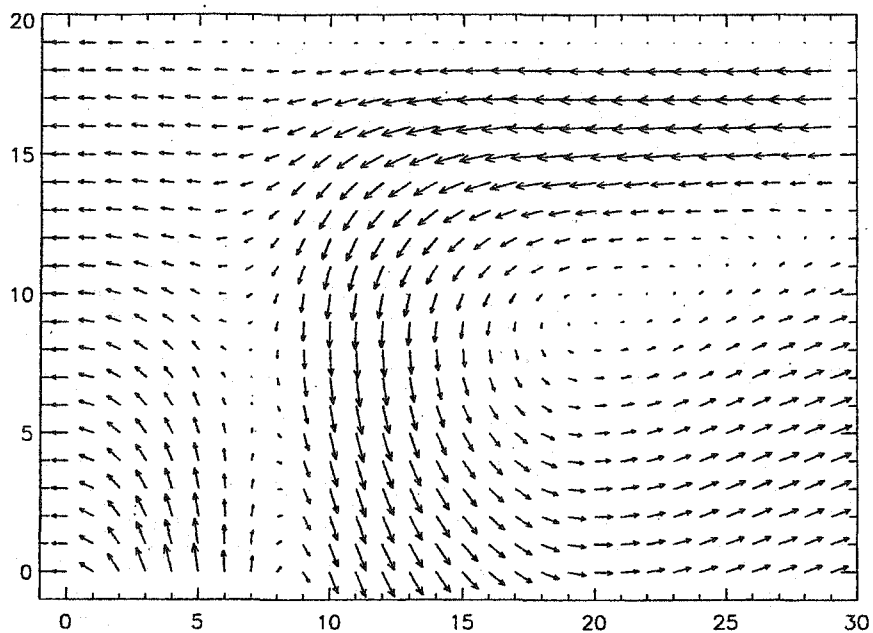


(a) Vector plot at  $t=3.001$

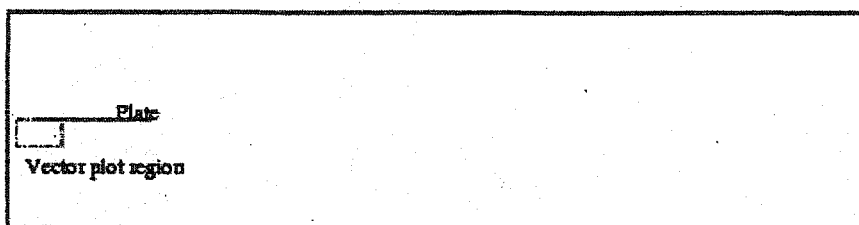


(b) Schematic of entire chamber showing vector plot region

Figure 6-27 Vector plot near front of plate at  $t=3.001$ .

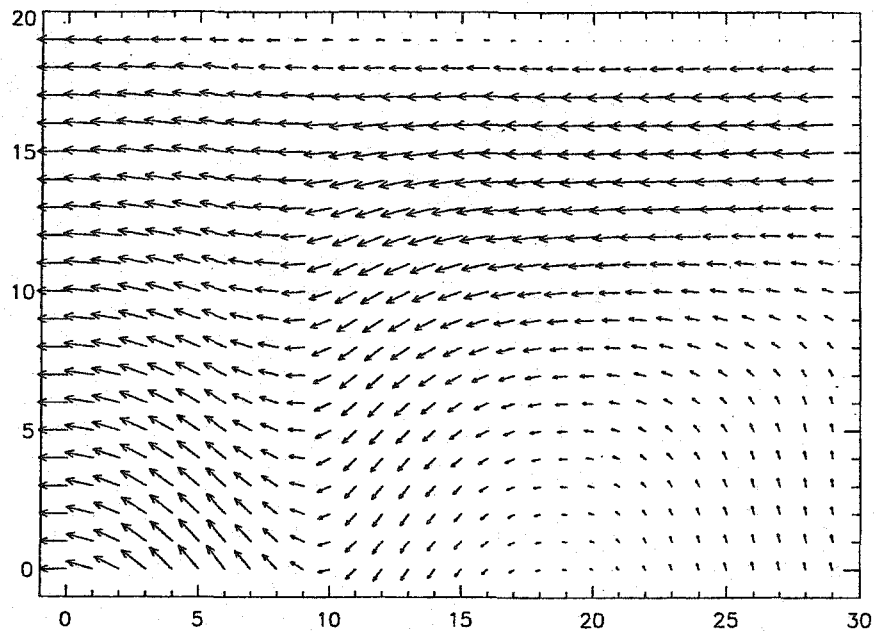


(a) Vector plot at  $t=3.301$

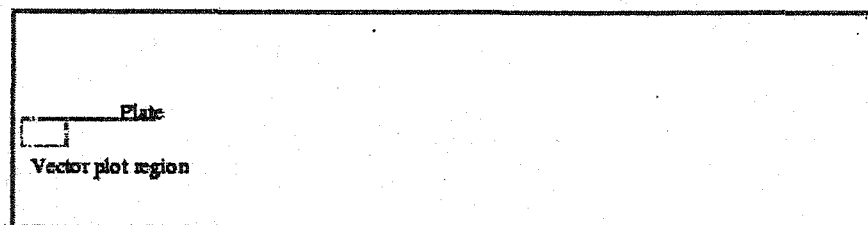


(b) Schematic of entire chamber showing vector plot region

Figure 6-28 Vector plot near front of plate at  $t=3.301$ .

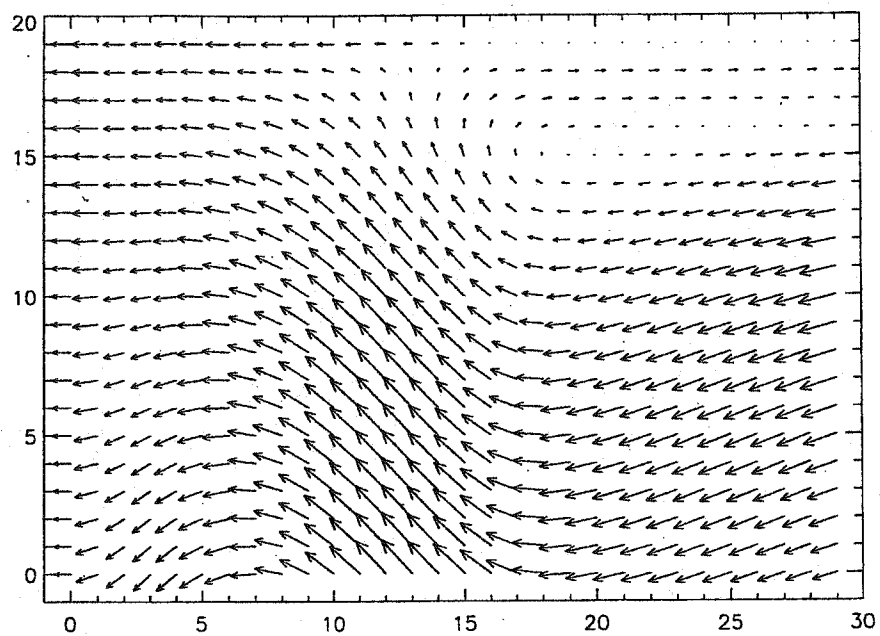


(a) Vector plot at  $t=3.601$

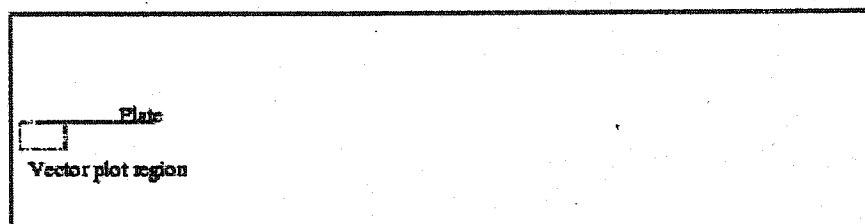


(b) Schematic of entire chamber showing vector plot region

Figure 6-29 Vector plot near front of plate at  $t=3.601$ .

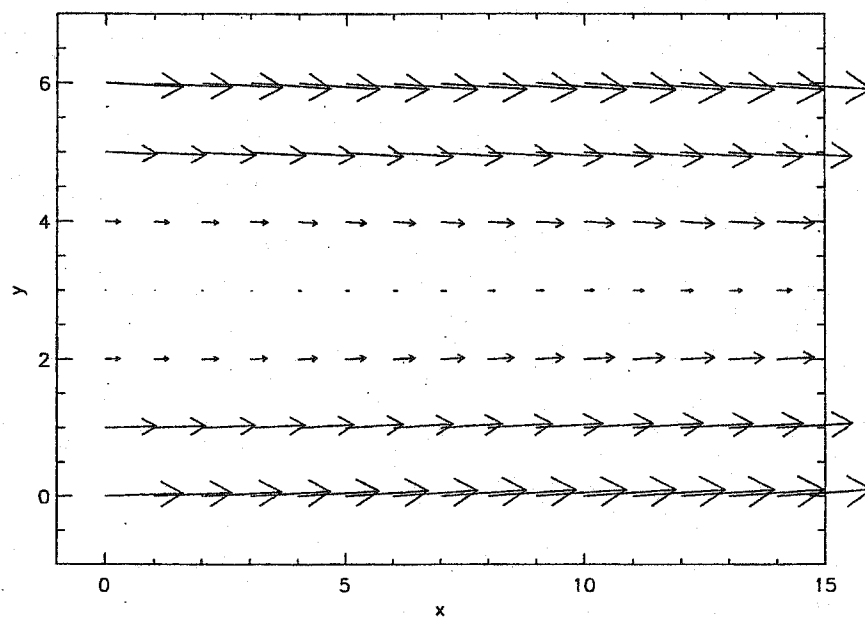
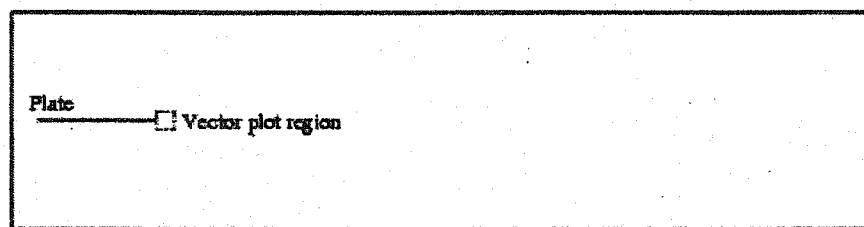


(a) Vector plot at  $t=6.001$



(b) Schematic of entire chamber showing vector plot region

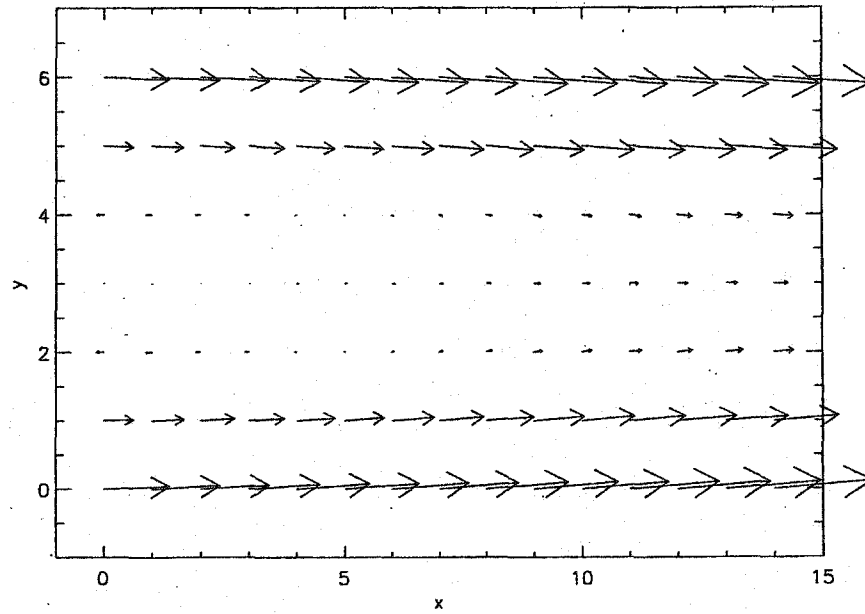
Figure 6-30 Vector plot near front of plate at  $t=6.001$ .

(a) Vector plot at  $t=2.701$ 

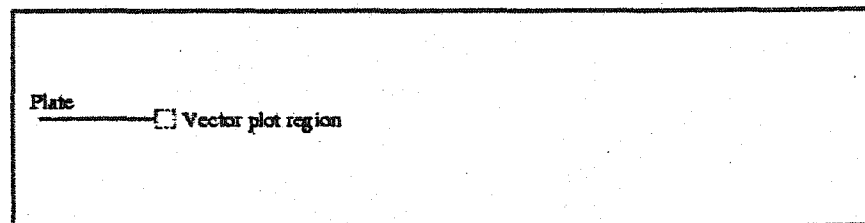
(b) Schematic of entire chamber showing vector plot region

Figure 6-31 Vector plot behind plate at  $t=2.701$ .





(a) Vector plot at  $t=3.001$



(b) Schematic of entire chamber showing vector plot region

Figure 6-32 Vector plot behind plate at  $t=3.001$ .

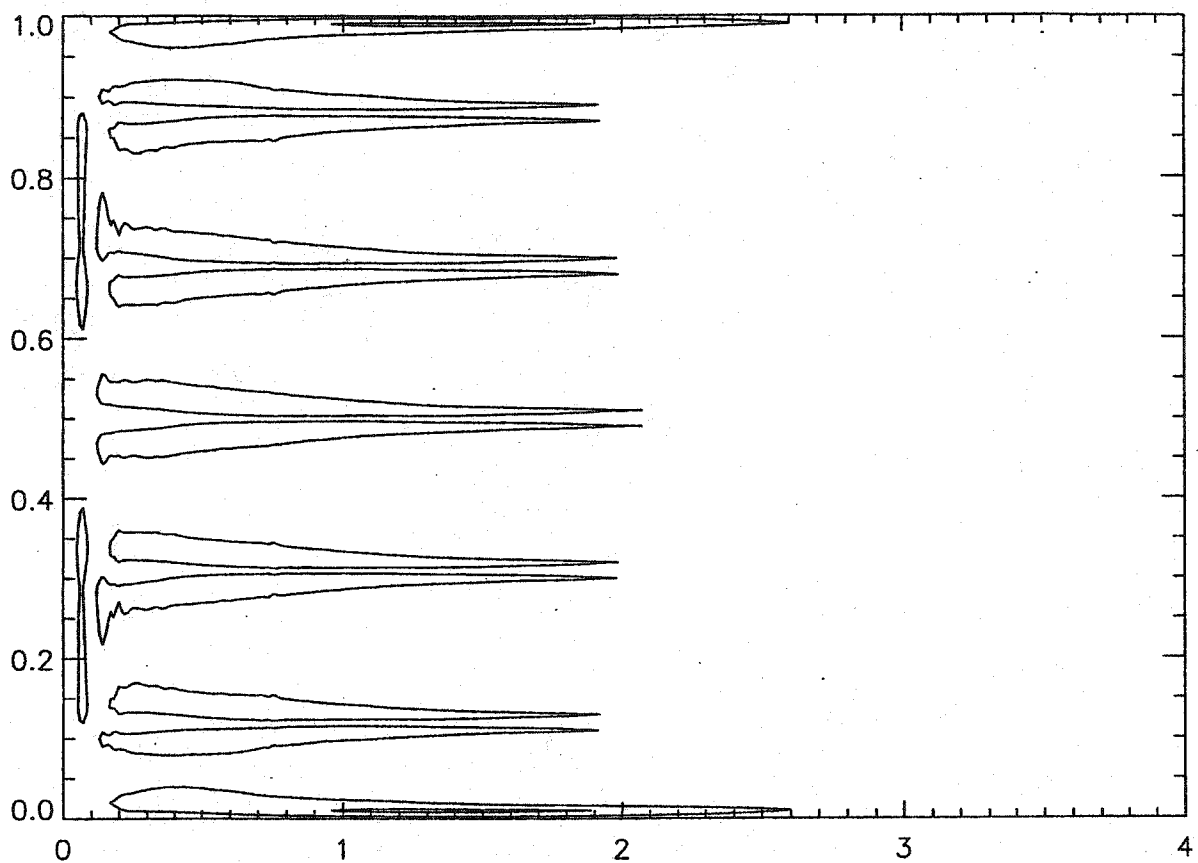


Figure 6-33 Vorticity contour in chamber with 5 plates.

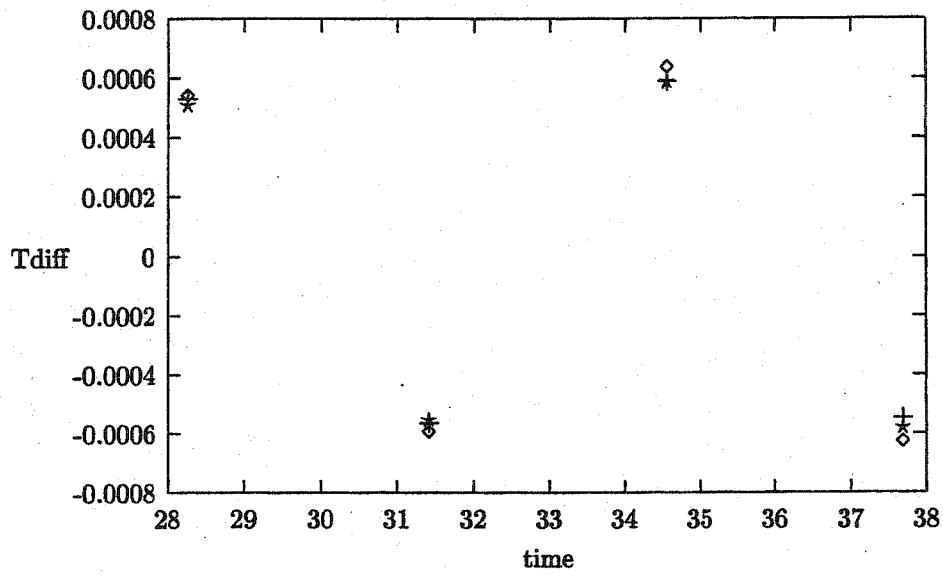


Figure 6-34 Temperature difference between plate ends, plate length=0.2.

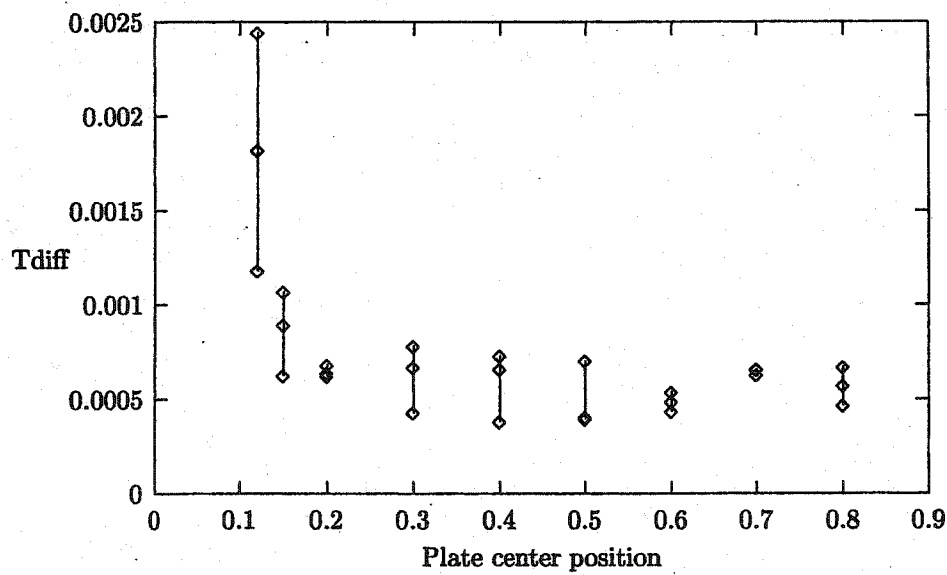


Figure 6-35 Temperature difference between plate ends versus plate position.

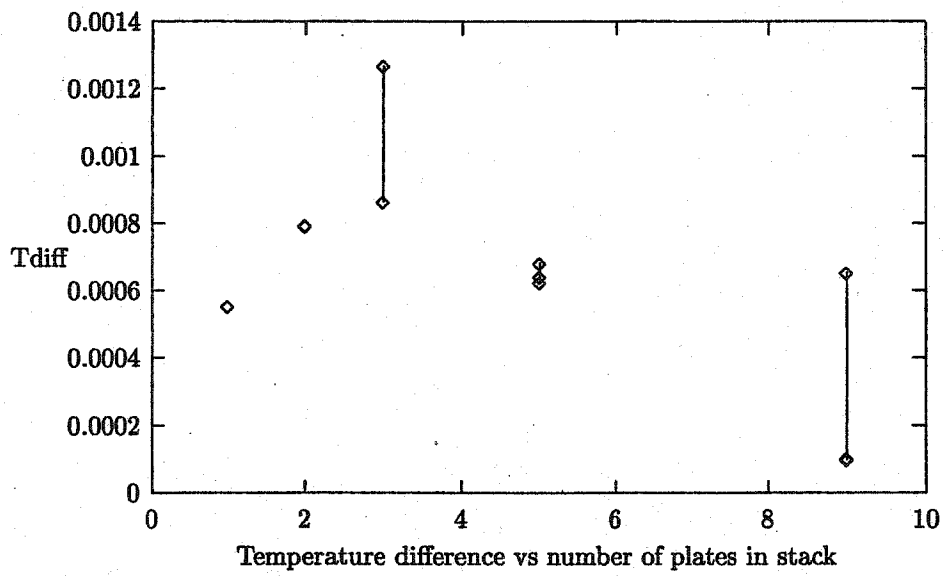


Figure 6-36 Temperature difference vs number of plates.

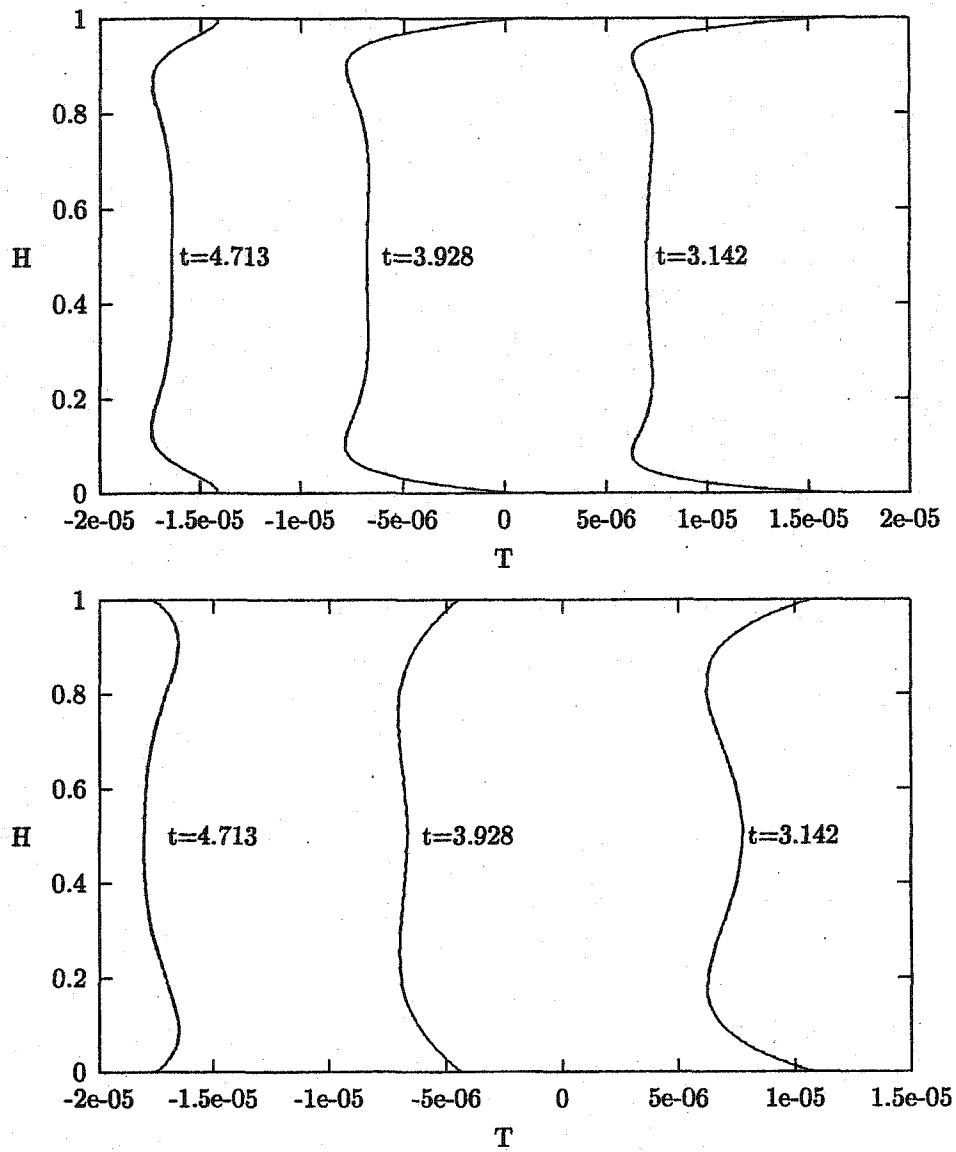


Figure 6-37 Temperature pattern between plates with 2-plate (top) and 9-plate (bottom).

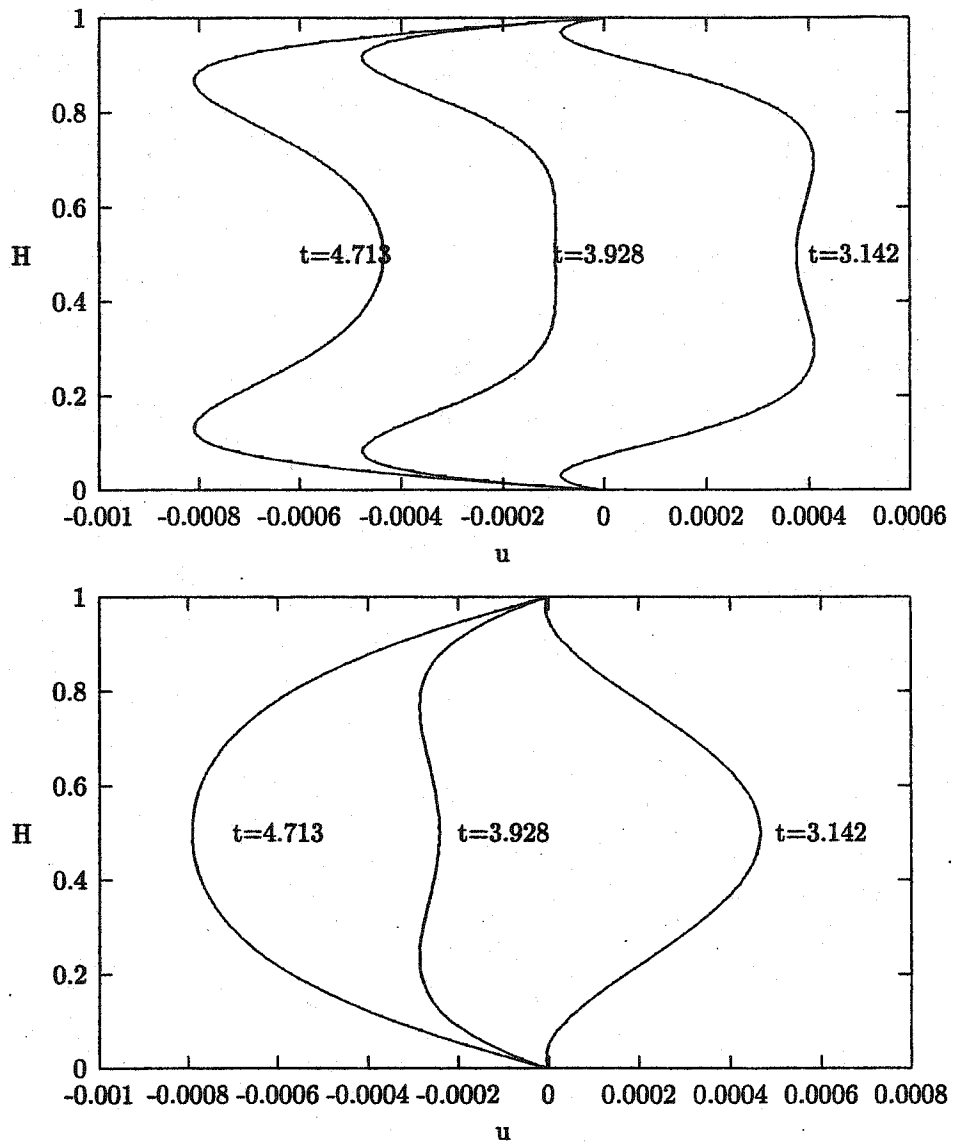


Figure 6-38 Flow pattern between plates with 2-plate (top) and 9-plate (bottom).

# Chapter 7

## Conclusions

The following general conclusions may be stated:

- The semi-implicit method is an accurate and efficient method for sub-sonic compressible viscous flow.
- Eliminating pressure from the governing equations eliminates the most severe numerical instabilities.
- Many types of secondary flows appear when an acoustic wave is forced in a closed chamber.
- Shed vorticity plays a key role in flow around a finite thickness heat exchanging plate.

## Bibliography

- [1] Strutt, J.W. (Lord Rayleigh), 1945, *The Theory of Sound*, ii, secs. 322f-i, Academic Press.
- [2] Hofter, T.J., 1986, "Thermoacoustic Refrigerator Design and Performance" *Ph.D. dissertation*, Physics Department, University of California at San Diego.
- [3] *Montreal Protocol on Substances That Deplete the Ozone Layer*, [www.ciesin.org/TG/PI/POLICY/montpro.html](http://www.ciesin.org/TG/PI/POLICY/montpro.html)
- [4] Swift, G.W., 1988, "Thermoacoustics Engines" *J. Acoust. Soc. Am.*, Vol. 94(2), pp. 941-943.
- [5] Bejan, A., 1995, *Convection Heat Transfer*, chap. 1. John Wiley and Sons, Inc.
- [6] Worlikar, A.S., Knio, O.M., 1996, "Numerical Simulation of a Thermoacoustic Refrigerator" *J. Computational Physics*, Vol. 127, pp. 424-451.
- [7] Cao, N., Olson, J.R., Swift, G.W., and Chen, S., 1996, "Energy Flux Density in a Thermoacoustic Couple" *J. Acoust. Soc. Am.*, Vol. 99(6), pp 3456-3464.
- [8] Gopinath, A., Tait, N.L., and Garrett, S.L., 1998, "Thermoacoustic Streaming in a Resonant Channel: The Time-averaged Temperature Distribution" *J. Acoust. Soc. Am.*, Vol. 103(3), pp 1388-1405.
- [9] Garrett, C.J.R., 1970, "On Cross-waves" *J. Fluid Mech.*, Vol. 41, pp 837-849.
- [10] Sherman, F.S., 1990, *Viscous Flow*, pp 137-140, McGraw-Hill.
- [11] Strutt, J.W. (Lord Rayleigh), 1945, *The Theory of Sound*, i Academic Press.
- [12] Riley, N., 2001, "Steady Streaming" *Annu. Rev. Fluid Mech.*, Vol. 33, pp 43-65.



# Appendices

The discrete equations to the linear Navier-Stoke system to be solved numerically are

$$\begin{aligned}
& \left(1 + 2a + \frac{8}{3}b + 2d\right) U_{i,j}^{n+1} \\
& - \left(a + \frac{4}{3}b\right) (U_{i+1,j} + U_{i-1,j})^{n+1} \\
& - d(U_{i,j+1} + U_{i,j-1})^{n+1} \\
& - \left(\frac{1}{3}e + f\right) (V_{i+1,j+1} - V_{i+1,j-1} - V_{i-1,j+1} + V_{i-1,j-1})^{n+1} \\
& = 2U_{i,j}^n - \left(1 + 2a - \frac{8}{3}b - 2d\right) U_{i,j}^{n-1} \\
& + \left(a - \frac{4}{3}b\right) (U_{i+1,j} + U_{i-1,j})^{n-1} \\
& - d(U_{i,j+1} + U_{i,j-1})^{n-1} \\
& - \left(\frac{1}{3}d - e\right) (V_{i+1,j+1} - V_{i+1,j-1} - V_{i-1,j+1} + V_{i-1,j-1})^{n-1}, \tag{78}
\end{aligned}$$

$$\begin{aligned}
& \left(1 + 2c + \frac{8}{3}d + 2b\right) V_{i,j}^{n+1} \\
& - \left(c + \frac{4}{3}d\right) (V_{i,j+1} + V_{i,j-1})^{n+1} \\
& - b(V_{i+1,j} + V_{i-1,j})^{n+1} \\
& - \left(\frac{1}{3}e + f\right) (U_{i+1,j+1} - U_{i+1,j-1} - U_{i-1,j+1} + U_{i-1,j-1})^{n+1} \\
& = 2V_{i,j}^n - \left(1 + 2c - \frac{8}{3}d - 2b\right) V_{i,j}^{n-1} \\
& + \left(c - \frac{4}{3}d\right) (V_{i,j+1} + V_{i,j-1})^{n-1} \\
& - b(V_{i+1,j} + V_{i-1,j})^{n-1} \\
& - \left(\frac{1}{3}e - f\right) (U_{i+1,j+1} - U_{i+1,j-1} - U_{i-1,j+1} + U_{i-1,j-1})^{n-1}, \tag{79}
\end{aligned}$$

$$\begin{aligned}
& T_{i,j}^{n+1} + ac(U_{i+1,j} - U_{i-1,j})^{n+1} + ad(V_{i,j+1} - V_{i,j-1})^{n+1} \\
& = T_{i,j}^{n-1} - ac(U_{i+1,j} - U_{i-1,j})^{n-1} - ad(V_{i,j+1} - V_{i,j-1})^{n-1}, \tag{80}
\end{aligned}$$

$$p_{i,j}^{n+1} - \left(\frac{\gamma}{\gamma-1}\right) T_{i,j}^{n+1} = p_{i,j}^{n-1} + \left(\frac{\gamma}{\gamma-1}\right) T_{i,j}^{n-1}, \tag{81}$$

where,

$$a = \frac{\Delta t^2}{2M^2 \Delta x^2} \qquad c = \frac{\Delta t^2}{2M^2 \Delta y^2}$$

$$\begin{aligned} b &= \frac{\Delta t}{2Re\Delta x^2} & d &= \frac{\Delta t}{2Re\Delta y^2} \\ e &= \frac{\Delta t}{8Re\Delta x\Delta y} & f &= \frac{\bar{p}\Delta t^2}{8M^2\gamma\Delta x\Delta y} \\ ac &= (\gamma - 1) \frac{\Delta t}{2\Delta x} & ad &= (\gamma - 1) \frac{\Delta t}{2\Delta y} \end{aligned}$$